12-2021

SiGeSn Light-Emitting Devices: from Optical to Electrical Injection

Yiyin Zhou
University of Arkansas, Fayetteville

SiGeSn Light-Emitting Devices: from Optical to Electrical Injection

A dissertation submitted in partial fulfillment
of the requirements for the degree of
Doctor of Philosophy in Microelectronics-Photonics

by

Yiyin Zhou
Tianjin University of Technology
Bachelor of Science in Applied Physics, 2011
University of Arkansas – Fort Smith
Bachelor of Science in Organizational Leadership, 2012
University of Arkansas
Master of Science in Microelectronics-Photonics, 2014

December 2021
University of Arkansas

This dissertation is approved for recommendation to the Graduate Council.

Shui-Qing Yu, Ph.D.
Dissertation Director

Hameed Naseem, Ph.D.
Committee Member

Gregory Salamo, Ph.D.
Dissertation Co-Director

Zhong Chen, Ph.D.
Committee Member

Matthew Leftwich, Ph.D.
Ex-Officio Member

The following signatories attest that all software used in this dissertation was legally licensed for use by Yiyin Zhou for research purposes and publication.

Yiyin Zhou
Student

Shui-Qing Yu, Ph.D.
Dissertation Director

Gregory Salamo, Ph.D.
Dissertation Co-Director

This dissertation was submitted to http://www.turnitin.com for plagiarism review by the TurnItIn company's software. The signatories have examined the report on this dissertation that was returned by TurnItIn and attest that, in their opinion, the items highlighted by the software are incidental to common usage and are not plagiarized material.

Matthew Leftwich, Ph.D.
Program Director

Shui-Qing Yu, Ph.D.
Dissertation Director

Gregory Salamo, Ph.D.
Dissertation Co-Director

Abstract

Si photonics is a fast-developing technology that impacts many applications such as data centers, 5G, Lidar, and biological/chemical sensing. One of the merits of Si photonics is to integrate electronic and photonic components on a single chip to form a complex functional system that features compact, low-cost, high-performance, and reliability. Among all building blocks, the monolithic integration of lasers on Si encountered substantial challenges. Si and Ge, conventional epitaxial material on Si, are incompetent for light emission due to the indirect bandgap. The current solution compromises the hybrid integration of III-V lasers, which requires growing on separate smaller size substrates and bonded on Si wafers. The monolithic growth of III-V lasers suffers from high-density defects and the growth temperature incompatible with the complementary-metal-on-semiconductor (CMOS) process. Therefore, alternative solutions are of high interest to overcome such difficulties. SiGeSn is a Group-IV semiconductor that could achieve direct bandgap, monolithically grown on Si substrate, and CMOS process compatible. These advantages make SiGeSn rather promising towards the monolithic laser for Si photonics.

This dissertation presents the multiple efforts on developing the GeSn-based lasers towards the electrical injection. The development process starts with the bulk lasers by optically pumping. By incorporating Sn in the active region and leaving the threading dislocation away from the active region, the maximum operating temperature (T_{max}) of the broad ridge laser reached 270 K with 20% Sn in the GeSn active region. The lasers with the multiple-quantum-well (MQW) as the gain region were studied for reducing the threshold. The results implied a sufficient gain volume was required to overcome the existing loss within the device. The laser structure with four wells exhibited lasing at temperatures up to 90 K. The introduction of the

SiGeSn cap layer balance more optical field overlapping the MQW active region, leading to an increase of T_{max}. By adding the quantum well number, the lasers showed improvement in the modal gain, eventually reducing the threshold and elevating the T_{max}. The study of light-emitting diodes provides the insight of GeSn heterostructures before achieving the electrically injected GeSn lasers. The three developing structures including Ge/GeSn/Ge, GeSn homojunction, and GeSn/GeSn/SiGeSn heterostructures were designed for: (1) achieving direct bandgap in GeSn active region, (2) incorporating high Sn composition and maintaining strain relaxation in the active region, and (3) eliminating carrier leakage through the hole barriers. With the advances in the GeSn heterostructures, the layer structures were applied to the electrically injected lasers. The electrically injected lasing from GeSn was demonstrated at temperatures up to 100 K. The laser diode structures were further investigated by comparing the layer material and thickness, providing further suggestions on optimizing the laser design.

Acknowledgements

I want to express thanks to my research advisor, Dr. Shui-Qing (Fisher) Yu, who provided guidance and support throughout my entire graduate school period. He brought me to the research field of optoelectronics, and he was always willing to pass all the knowledge to me. His passion and vision of the research have profoundly affected me, eventually resulted in this dissertation. I could not imagine achieving such progress without his guidance. My appreciation goes to Dr. Baohua Li, who is the president of Arktonics, LLC. She provided me the opportunity to conduct research that meets the company's requirements. Her spirit of paying attention to details made tremendously help on my projects. My sincere gratitude extends to my dissertation committee members: Dr. Gregory J. Salamo, Dr. Hameed Naseem, Dr. Chen Zhong, and Dr. Matthew Leftwich. Their genuine advice always helped my improvement. The mentorship covered me through graduate research and study. I would like to appreciate Mr. Ken Vickers and Dr. Rick Wise for providing wonderful opportunity in Microelectronics-Photonics Program.

I would like to thank Dr. John Tolle and Dr. Joe Margetis for the effort of providing the epitaxial growth of all the structures. I would like to thank Mr. Errol V. Porter and HiDEC staffs for providing supports on the fabrication process. I would like to thank Dr. Seyed Amir Ghetmiri and Sattar Al-Kabi for initiating the optical characterization setups. I want to further express my thank to Dr. Yong-Hang Zhang, Dr. Jifeng Liu, Dr. Greg Sun, Dr. Richard Soref for their insightful discussion on the research result.

Finally, I would like to express my thank to Dr. Wei Du for his discussion in research discussions and technical writing. I would like to thank Dr. Aboozar Mosleh, Dr. Thach Pham, Dr. Wei Dou, Dr. Huong Tran, Mr. Joshua Grant for the delightful discussions on the technical

and scientific questions. I want to thank all the lab mates. I am grateful and honored to work with you as a team, which I'm deeply proud of.

The work in this dissertation was partially supported by Air Force SBIR Phase I and Phase II Projects "Epitaxial Technologies for SiGeSn High Performance Optoelectronics Devices" under contract numbers FA9550-14-C-0044 and FA9550-16-C-0016 (PI: Dr. Baohua Li from Arktonics LLC and Program manager: Dr. Gernot S. Pomrenke from Air Force Office of Scientific Research). Any opinions, findings, and conclusions or recommendations expressed in this material are those of the author and do not necessarily reflect the views of the Air Force. The work is also supported by the National Science Foundation (NSF) under contract number DMR-1149605. Any opinions, findings, and conclusions or recommendations expressed in this material are those of the author and do not necessarily reflect the views of the NSF. Support is also appreciated from Air Force Office of Scientific Research (AFOSR) under contract number FA9550-14-1-0205, FA9550-17-1-0354, W911NF-16-1-0517, FA9550-18-1-0045, and FA9550-19-1-0341. Any opinions, findings, and conclusions or recommendations expressed in this material are those of the author and do not necessarily reflect the views of the AFOSR. The work is partially funded by National Aeronautics and Space Administration Established Program to Stimulate Competitive Research (NASA EPSCoR) under contract number NNX15AN18A. Any opinions, findings, and conclusions or recommendations expressed in this material are those of the author and do not necessarily reflect the views of NASA. I am thankful for Dr. M. Benamara's assistance in TEM imaging and Dr. A. Kuchuk's assistance in the XRD measurement from Institute for Nanoscience & Engineering, University of Arkansas.

Dedication

To my father, Jiquan Zhou, who offer endless support throughout my life. To my mother, Hong Liu, for being an excellent example who diligently pursues her dream. To my grandfather, Runpu Liu, who buried the seeds deep in my mind to study abroad and pursue the doctoral degree and he always believed in my success. To all my friends and family, who paint my overall journey full of happiness and love.

Table of Contents

List of Figures

List of Tables

List of Published Papers Used in This Dissertation

Part of Chapter 2 was originally published as:

> Reprinted with permission from "Si-based GeSn lasers with ridge and planar waveguide structures and operating temperatures up to 270 K" Yiyin Zhou, Wei Dou, Wei Du, Solomon Ojo, Huong Tran, Seyed A. Ghetmiri, Jifeng Liu, Greg Sun, Richard Soref, Joe Margetis, John Tolle, Baohua Li, Zhong Chen, Mansour Mortazavi, Shui-Qing Yu, ACS Photonics, 6, 1434 (2019). Copyright (2019) American Chemical Society.

Part of Chapter 3 was originally published as:

> Reproduced from "All group-IV SiGeSn/GeSn/SiGeSn QW laser on Si operating up to 90 K", Joe Margetis, Yiyin Zhou, Wei Dou, Perry C. Grant, Wei Du, Bader Alharthi, Huong Tran, Solomon Ojo, Grey Abernathy, Seyed A. Ghetmiri, Jifeng Liu, Greg Sun, Richard Soref, John Tolle, Baohua Li, Mansour Mortazavi, Shui-Qing Yu, Applied Physics Letters 113 (22), 221104 (2018), with the permission of AIP Publishing.

Part of Chapter 4 was originally published as:

> Reproduced from ["Systematic study of Si-based GeSn light-emitting diodes towards mid-infrared applications", Yiyin Zhou, Wei Dou, Wei Du, Thach Pham, Seyed Amir Ghetmiri, Sattar Al-Kabi, Aboozar Mosleh, Joe Margetis, John Tolle, Greg Sun, Richard Soref, Baohua Li, Mansour Mortazavi, Hameed Naseem, and Shui-Qing Yu, Journal of Applied Physics 120, 023102 (2016)], with the permission of AIP Publishing.

Part of Chapter 5 was originally published as:

> Reprinted with permission from "Electrically injected GeSn lasers on Si operating up to 100 K" Yiyin Zhou, Yuanhao Miao, Solomon Ojo, Grey Abernathy, Sylvester Amoah, Wei Du, Jifeng Liu, Yong-Hang Zhang, Greg Sun, Richard A. Soref, Baohua Li, Shui-Qing Yu, Optica, 9, pp.924-928 (2020). © The Optical Society

Part of Chapter 5 was originally submitted as:

> "Electrically injected GeSn lasers with peak wavelength up to 2.7 μm" Yiyin Zhou, Solomon Ojo, Chen-Wei Wu, Yuanhao Miao, Huong Tran, Joshua M. Grant, Grey Abernathy, Sylvester Amoah, Jake Bass, Gregory Salamo, Wei Du, Guo-En Chang, Jifeng Liu, Joe Margetis, John Tolle, Yong-Hang Zhang, Greg Sun, Richard A. Soref, Baohua Li, Shui-Qing Yu.

Chapter 1: Introduction

1.1 Background

Si photonics made expanding impacts in optical applications such as data communications, 3D sensing, spectral sensing, and so on [1]. The technology integrates the photonic components onto a silicon chip to reduce the optical system's size, cost, and power consumption, with potentially increased performance and reliability. The major driving force is the transceiver markets for data centers, long haul, and 5G, thanks to the expanding demand of network traffic for cloud service, media streaming, and the Internet of Things. As the system is more compact with lower costs, the photonic chip on silicon could enable the next-generation communication system and data interconnects [2], powered by boosted data transfer speed and reliability. 3D sensing using LiDAR is another fast-growing market where Si photonics may shine [3]. The high level of autopilot function requires accurate sensing capability, which is often enabled by adopting the optical coherent emission and detection. Furthermore, the spectral sensors using Si photonics can be widely applied to industrial gas monitoring and medical diagnose [4]. The sensor integrated on a chip is expected to deliver a higher sensitivity at a lower cost.

The integration of photonic devices on the Si platform offers many advantages over other platforms. The fabrication process on Si has been well developed for decades. The achievable features size for the Si platform (~nanometers) is few orders of magnitude smaller than the photonic devices (~micrometers). The commercial foundries for Si Photonics are emerging with research and development capabilities, which pushes Si photonics to become mature for large volume production [5]. Furthermore, the optical waveguide bending radius is small compared to

other PIC platforms. This smaller bending radius allows a higher density of photonic circuits to be integrated on the wafer, leading to further reduction of the size and the cost. The unique merit for Si photonics is to integrate the complementary-metal-oxide-semiconductor (CMOS) electronics and photonic circuits on the same chip. The co-integration promises lower cost and size, higher performance of the system.

In Si Photonics, great successes were made for most building block devices such as waveguides, modulators, and photodetectors. However, the monolithic integration of light sources remains constrained [6]. The conventional epitaxial materials, namely Si, Ge, and SiGe alloys, have been excluded from being an efficient light source due to their indirect bandgap nature. Although the optically pumped rare-earth-doped lasers on Si [7,8]and the Si Raman laser [9] have been reported, they do not rely on bandgap emission and cannot be operated under direct electrical pumping. Recently developed Ge lasers [10] employed strain-engineering and heavily n-type doping to compensate for its indirect bandgap, yet the high threshold and fabrication difficulties remain unresolved thus far. Currently, the light source on Si compromises the heterogeneous integration of direct bandgap III-V lasers [11]. Improving the yields of heterogeneous integration involves extra efforts and costs. The monolithic III-V quantum dot lasers on Si were recently demonstrated the decent performance that is not limited to the buffer threading dislocations [12]. In order grow quantum dot, the molecular beam epitaxy (MBE) is required for the epitaxial growth, which is still a laboratorial technique rather than a large volume industrial method. Furthermore, the growth temperatures of III-V epitaxial layers are typically too high to be compatible with CMOS process.

The light emitters made by the direct bandgap group-IV material could offer unique advantages, particularly the material integration compatibility with the CMOS process. In the

recent decade, the studies of SiGeSn alloy showed the bright future towards group-IV-based monolithic lasers on the Si platform.

1.2 SiGeSn alloy

The SiGeSn is a group-IV-based semiconductor alloy that promises the laser solution for CMOS compatible optoelectronics on the Si platform. It has several advantages to build the light-emitters son Si [13]: i) it can be tuned as a direct bandgap for light emission; ii) the epitaxial growth is monolithic on Si using the commercially available chemical vapor deposition (CVD) reactor; iii) the growth temperature is below the thermal limit for the CMOS process, iv) the lattice constant covers broad range to fit many substrates; v) the bandgap energy can be tuned to cover a broad wavelength, from near- to mid-infrared.

The direct bandgap SiGeSn is the key to the lasers on Si. The typical light emission process from a semiconductor relies on the carrier population in conduction and valence band. Specifically, the light emission process (radiative recombination and stimulated emission) is much more efficient in the direct bandgap semiconductors than the indirect bandgap ones. In a direct bandgap semiconductor, the electrons populate in the conduction band minimum the Γ point, having the same momentum with the holes populating in the valence band maximum. However, in the indirect bandgap, the electrons populate in the condition band with the momentum different from the holes. Consequently, the carrier recombination through indirect bandgap semiconductor needs assistance from extra factors to follow the conservation of momentum, such as the interaction with phonons (lattice vibration). Therefore, the probability of radiative recombination and stimulated emission in an indirect bandgap semiconductor is much lower than in the direct bandgap. The direct bandgap is preferred for the light emission from the

semiconductor compared to the indirect bandgap.

The direct bandgap SiGeSn was achieved by incorporating more Sn content into the alloy. By incorporating more Sn composition into Ge, the GeSn bandgap transits from indirect to direct bandgap at ~ 8% Sn content. The direct bandgap GeSn became the high interest for light-emission on the Si platform. Back in 1991, Soref and Perry calculated the bandgaps for the direct bandgap GeSn [14]. In the calculation, the alloy exhibited direct and indirect bandgaps with the change of element compositions. The Sn incorporation will induce a reduction of conduction band energy. Moreover, the Γ valleys in the conduction band drop at a different rate as more Sn is incorporated. With a certain Sn incorporation, the GeSn becomes a direct bandgap semiconductor. The bandgap energy vs. lattice constant of common semiconductors for optoelectronics is plotted in Fig. 1. For SiGeSn, the bandgap energy ranges from around 1.2 eV, which is Si-rich, all the way to zero, which is Sn-rich and becomes a conductor. This theoretical calculation predicts a broad coverage from infrared applications.

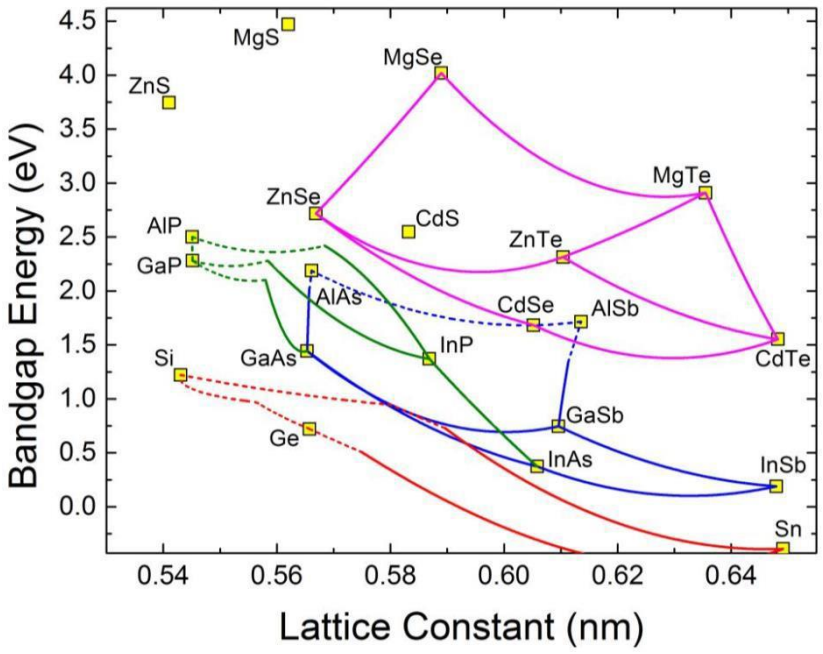

Figure 1. SiGeSn ternary alloy bandgap energy vs. lattice constant compared to common semiconductors for optoelectronics [15].

The first demonstration of the single crystalline growth of metastable GeSn was achieved by using sputtering technique, with Sn content exceeds 1% [16]. The success of GeSn crystalline growth using MBE [17] further attracted more attentions to the GeSn research. J. Taraci demonstrated the GeSn crystalline growth using CVD reactor [18]. The availability of multiple synthesis instruments paved the paths of SiGeSn study since then. The MBE and CVD become two major instruments for the SiGeSn research.

The MBE is one of the most conventional growth tools for optoelectronic device research. It has many strengths, such as the atomic level growth ensures the high-quality crystalline while providing excellent control of layer thickness and alloy composition. For SiGeSn, MBE is quite a powerful tool driving the GeSn research with high quality epitaxial films. However, as the Sn incorporation progress towards high content, the MBE seems limited due to large a lattice mismatch between the GeSn and Ge. The thick GeSn buffer appears to be a solution to ease such mismatch in the CVD growth, which is ineffective for MBE growth due to the low growth rate.

The CVD reactor demonstrated several advantages for SiGeSn growth compared to other methods. First, as the standard group-IV material epitaxial instrument for the industry, the reactor could maintain a decent growth rate while producing thick films with decent crystalline quality. The high-quality epitaxial layer can be grown directly on the 200-mm Si substrate, which has a great potential for large volume production. Furthermore, the growth temperature of SiGeSn is below 450 ˚C, which is CMOS compatible. This feature promises the co-integration of photonic and electronic circuits on a single chip, making the SiGeSn stand out from all other candidates for integrated lasers on Si.

The alloy could be tuned to the different lattice constants. The tunability could enable the

lattice-matched heterostructures with the type-I alignment. The type-I heterostructures are commonly used in III-V semiconductors for carrier confinement. With a small bandgap layer sandwiched with large bandgap barriers, the carriers can be trapped within the small bandgap layer, featuring a higher population of carries in the designated energy levels that contribute to the light emission. A lattice-matched heterostructure owns this feature while eliminates the non-radiative recombination centers caused by the defects induced by the large difference in the lattice constant among the layers. The defect serves as the extra leakage channels that "steal" carriers from the radiative recombination. In the SiGeSn alloy, the bandgap and the lattice constant can be independently tuned by varying the Si and Sn composition. As a result, strain engineering is a major topic on the SiGeSn. Similar to other compound semiconductors, such as AlGaAs and InGaP, SiGeSn allows the independently tune the bandgap and the lattice constant. The lattice-matched heterostructures would further reduce the compressive strain and dislocations caused by the lattice mismatch.

1.3 History of GeSn light emitters

The light emission from direct bandgap GeSn is of great interest for the SiGeSn study. The electrical injection light emitters are mainly focused on light-emitting diodes (LEDs). The GeSn LEDs with low Sn compositions showed room temperature emissions from indirect bandgap transitions [19,20]. As the Sn composition reached to 8% and beyond, direct bandgap emission was recorded [21-23]. The carrier confinement started with the Ge barriers in the DHS [20,21]. The MQW structures were presented, showing enhanced emission [24,25]. Due to the large mismatch between Ge and high Sn composition GeSn, it is hard to achieve high Sn composition using the Ge barriers. Furthermore, the mismatch led to the compressive strain in

the GeSn layer, which makes the GeSn transfer from direct towards indirect bandgap. GeSn DHS with stepped-bandgap GeSn and SiGeSn barriers were presented, showing a relative performance improvement with the 16% Sn in the active region [26].

GeSn laser structures with double-heterostructure (DHS) [27], strain-balanced multiple quantum well (MQW) [28], and lattice-matched MQW structures [29] were proposed promising the lasing transitions at room temperature. The microdisk resonator was demonstrated the whispering-gallery-mode from the Ge/GeSn/Ge quantum well (QW) structure [30]. As predicted by the theoretical calculation, the experiment showed that GeSn becomes a direct bandgap semiconductor incorporating Sn composition beyond ~8% [31]. In 2015, S. Wirth et al. presented the first optically pumped lasers with Sn composition at 12.6% [32]. Since then, GeSn started the age of developing optically pumped lasers. Great efforts were made to reduce the threshold [33] and maximum operating temperatures (Tmax) [34,35]. The lasers with gain region using bulk [34-37], heterostructure [38], and MQW [39] are reported, showing the laser performance can be improved by proper carrier confinement. The increase of Sn composition in the GeSn active region was found to improve the Tmax. The ridge waveguide lasers and microdisk lasers are compared using the same gain material [40], showing the characteristics of the respective structure. Research showed that the management of defect in the buffer layer played an important role in reducing the laser threshold [41]. By introducing the tensile strain, GeSn microdisk lasers operated under continuous-wave pumping conduction at cryogenic temperatures [42]. All these innovative studies were carried under the optical pumping scheme. There electrically injected GeSn lasers remain unexplored. The highlights of GeSn laser are summarized in Fig. 2.

1.4 Theory of semiconductor lasers

1.4.1 Band structure calculation of SiGeSn heterostructures

For laser diode design, bandgap engineering is one of the powerful tools to achieve the desired functions such as wavelength tuning, carrier confinement, optical mode guiding, loss reduction, etc. The bandgap engineering adopts multiple layers with specifically chosen composition,

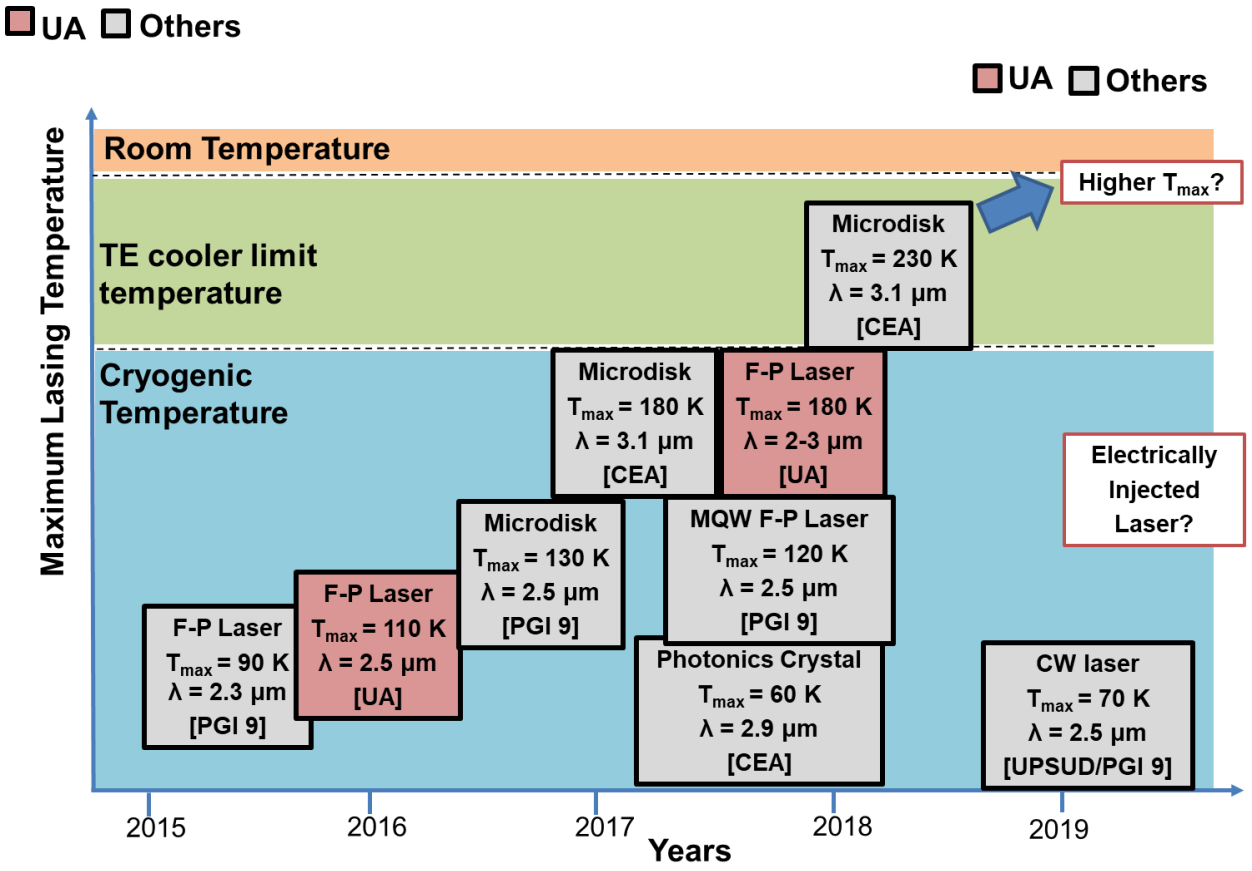

Figure 2. Typical progress of GeSn laser prior to this work.

strain, and thickness. The process of such design requires the calculation of the band structure. In this section, the band energy calculation is described as three parts: band offset determination, bandgap calculation, band edge affected by strain.

The valence band energy for $Si_yGe_{1-x-y}Sn_x$ is determined as:

$$E_v = E_{v,av} + \Delta/3 \quad \text{(Equation 1.1)}$$

where E_v is the valence band energy where heavy hole (HH) and light hole (LH) degenerates at wavevector k = 0. The $E_{v,av}$ is the average valence band energy, the Δ is the spin-orbit splitting energy. The $E_{v,av}$ for $Si_yGe_{1-x-y}Sn_x$ is determined as:

$$E_{v,av} = (1 - x - y)E_{v,av,Ge} + xE_{v,av,Sn} + yE_{v,av,Si} \quad \text{(Equation 1.2)}$$

where $E_{v,av,Si}$, $E_{v,av,Ge}$, $E_{v,av,Sn}$, are the average band energy for Si, Ge, and Sn, respectively. The spin-orbit splitting energy for $Si_yGe_{1-x-y}Sn_x$ is linearly interpolated as:

$$\Delta = (1\text{-}x\text{-}y)\Delta_{Ge} + x\Delta_{Sn} + y\Delta_{Si} \quad \text{(Equation 1.3)}$$

where Δ_{Si}, Δ_{Ge}, Δ_{Sn}, are the spin-orbit splitting energy for Si, Ge, and Sn, respectively.

The bandgap calculation determines the energy difference between conduction band edge E_c and valence band E_v. In the conduction band, two valley minima are considered here: Γ and L. In SiGeSn material system, the direct bandgap is the difference between the Γ valley minimum $E_{c\Gamma}$ and E_v. The indirect bandgap is the difference between L valley minimum is E_{cL} and E_v:

$$E_{g,\Gamma} = E_{c,\Gamma} - E_v \quad \text{(Equation 1.4)}$$

$$E_{g,L} = E_{c,L} - E_v \quad \text{(Equation 1.5)}$$

The bandgap energy is interpolated following Vegard's law with the bowing parameters:

$$E_g = (1 - x - y)E_{g,Ge} + xE_{g,Sn} + yE_{g,Si} - x(1 - x - y)b_{GeSn} - y(1 - x - y)b_{SiGe} + xyb_{SiSn} \quad \text{(Equation 1.6)}$$

where b_{GeSn}, b_{SiGe}, and b_{SiSn} are the bowing parameters for GeSn, SiGe, and SiSn, respectively.

The in-plane strain ε is defined as:

$$\varepsilon = \varepsilon_{xx} = \varepsilon_{yy} = \frac{a_0 - a}{a_0} \quad \text{(Equation 1.7)}$$

where a_0 is the lattice constant of the substrate, and a is the lattice constant of the epitaxial layer. The perpendicular strain, or out-of-plane strain, $\varepsilon_{\perp}$ in semiconductor is defined as:

$$\varepsilon_{\perp} = \varepsilon_{zz} = -2\frac{C_{12}}{C_{11}}\varepsilon \quad \text{(Equation 1.8)}$$

where C_{11} and C_{12} are the elastic stiffness constants.

The strain in semiconductor will cause the band edge shift on both conduction band and valence band. The conduction band shift ΔE_c from original E_c:

$$\Delta E_c = a_c(\varepsilon_{xx} + \varepsilon_{xx} + \varepsilon_{xx}) \quad \text{(Equation 1.9)}$$

where a_c is the conduction band deformation potential energy. For valence band, the LH and HH band edge shift as:

$$\Delta E_{v,HH} = -P_{\varepsilon} - Q_{\varepsilon} \quad \text{(Equation 1.10)}$$

$$\Delta E_{v,LH} = -P_{\varepsilon} - \frac{\Delta}{2} + \frac{Q_{\varepsilon}}{2} - \frac{1}{2}[\Delta^2 + 2\Delta Q_{\varepsilon} + 9Q_{\varepsilon}^2]^{1/2} \quad \text{(Equation 1.11)}$$

$$P_{\varepsilon} = -a_v(\varepsilon_{xx} + \varepsilon_{yy} + \varepsilon_{zz}) \quad \text{(Equation 1.12)}$$

$$\mathrm{Q}_{\varepsilon} = -\frac{\mathrm{b}}{2}(\varepsilon_{\mathrm{xx}} + \varepsilon_{\mathrm{yy}} - 2\varepsilon_{\mathrm{zz}}) \quad \text{(Equation 1.13)}$$

where a_v is the valence band deformation potential energy, b is the shear deformation potential energy.

Finally, the band edge energy with the effect of strain is expressed as:

$$E_{c,\Gamma} = E_v + E_{g,\Gamma} + \Delta E_c \quad \text{(Equation 1.14)}$$

$$E_{c,\mathrm{L}} = E_v + E_{g,\mathrm{L}} + \Delta E_c \quad \text{(Equation 1.15)}$$

$$E_{v,HH} = E_v + \Delta E_{v,HH} \quad \text{(Equation 1.16)}$$

$$E_{v,LH} = E_v + \Delta E_{v,LH} \quad \text{(Equation 1.17)}$$

1.4.2 Theory of carrier transitions in laser for the device development

The semiconductor lasers rely on the carrier transitions, which aim at convert carriers to coherent light emission. The device typically involves five transitions simultaneously during the lasing process: (1) absorption, (2) Shockley-Reed-Hall recombination (SRH), (3) radiative recombination, (4) Auger recombination, and (5) stimulated emission. Figure 3 depicts the five transitions in a semiconductor. One primary goal to develop the GeSn laser design is to analyze the carrier transition mechanism and improve the efficiency of the stimulated emission process. Base on the knowledge described in this section, the laser designs in this dissertation are closely focused on these transitions.

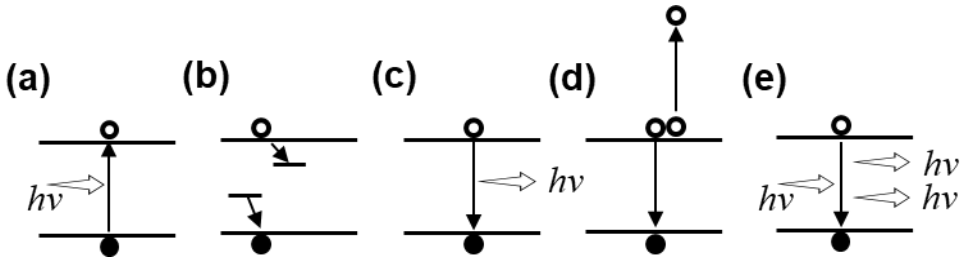

Figure 3. Carrier transitions in laser devices: (a) absorption, (b) SRH recombination, (c) radiative recombination, (d) Auger recombination, (e) stimulated emission.

Absorption: Optical absorption is one of the critical characteristics of a semiconductor. The absorption of a photon creates a pair of electron and hole with the incident light energy hν. For an intrinsic semiconductor, the absorption energy is equal to or larger than the bandgap. This transition is one of the typical methods to inject carriers into the semiconductor by exciting external pumping light source on the semiconductor surface. Optically pumped laser is one type of laser which an external laser injects carriers. Chapter 2 and 3 discuss the study of GeSn laser using optical pumping.

SRH recombination: The SRH recombination describes the carrier recombination through the trap levels within the bandgap. The trap levels are introduced by the impurities source, such as extrinsic dopants, vacancies, dislocations, surface, interface, etc. A single trap level absorbs

and emits one carrier, contributing to the total carrier recombination process. Temperature is one key factor for SRH recombination. The trap levels are mostly frozen at low temperatures (typically less than 100 K). With elevated temperatures, the trap levels are thermally activated and contributing to the recombination process. Therefore, low-temperature characterization of semiconductors often reflects more intrinsic knowledge from the material without the interference of the SRH recombination. Similarly, in a laser device, the carriers would have less carrier recombining with the trap levels, promising a higher efficiency.

Radiative recombination: Radiative recombination is the carrier recombination process with photon emission spontaneously. The photon energy equals the energy difference between the electron and hole before the recombination. Most of the carriers accumulate at the conduction band minimum and the valence band maximum in the semiconductor, so this recombination process is also called band to band recombination. In Fig. 4(a), the carriers occupy the lowest energy of the energy states at the band edge. The higher energy tail is the result of the carrier thermal distribution. The emission spectrum follows the probability of the carriers' energy distribution, which results from the density of state and the Fermi-Dirac distribution, shown in Fig. 4(b).

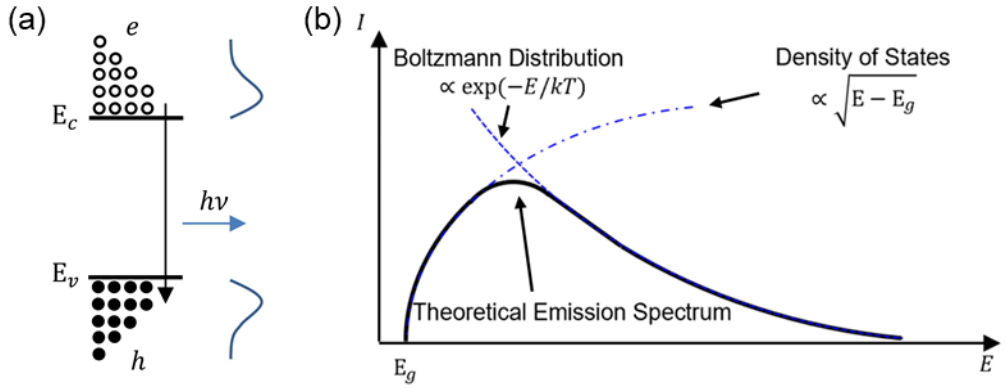

Figure 4. (a) The electron and hole distribution and radiative recombination process, (b) the photon emission intensity of the radiative recombination.

Auger recombination: The Auger recombination is a three-carrier non-radiative recombination process. Typically involves an electron-hole pair and the third particle at three energy levels. The energy exchanged among the three particles carrier interaction. Auger recombination is non-radiative recombination that consumes the carrier density, especially at a high carrier density level.

Stimulated emission: For the laser operation, the stimulated emission is the dominating transition. The stimulated emission started with the condition of population inversion. In the condition of population inversion, the electron population in upper states is more than in lower states. In a semiconductor, the two quasi-Fermi levels reached population inversion when the carrier density is sufficiently high. Under such condition, a photon with the same energy of the quasi-Fermi levels will interact with the carriers at two state levels, producing a copy photon with the same energy. This process involves the exchange of energy between the carriers and the emitted photon. With a photon exciting a generation of a copied photon, this photon amplification process is called stimulated emission.

Rate equation: The carrier density change per unit time for a semiconductor laser is described using the carrier rate equation:

$$\frac{dn}{dt} = \frac{\eta_i I}{qV} - \left(R_{SRH} + R_{Auger} + R_{rad}\right) - R_{stim} \qquad \text{(Equation 1.18)}$$

where n is the carrier density, t is the time, η_i is the carrier injection efficiency, I is the total current, q is the electron charge, V is the volume of the active region, R_{SRH}, R_{rad}, R_{Auger} and R_{stim} are the SRH recombination, radiative recombination, auger recombination, and stimulated emission rate. On the right-hand side of the equation, the first term describes the carrier injection rate into the active region. The second and third terms in the apprentice account for the SRH, radiative, and Auger recombination, where SRH and Auger recombination account for the non-

radiative recombination. The three transitions are spontaneously in the active region. The rate follows: $R_{SRH} + R_{Auger} + R_{rad} = An + Bn^2 + Cn^3 = n/\tau$, where A, B, and C are the coefficient for the SRH, radiative, and Auger recombination, respectively, τ is the carrier lifetime. The last term of the rate equation describes the carrier consumption rate due to the stimulated emission. This consumption rate follows:

$$R_{stim} = v_g g S \qquad \text{(Equation 1.18)}$$

where v_g is the group velocity, g is the material gain, S is the photon density.

Typically for a laser diode, the total current I contributes to the active region current and leaking current. The active region current is partial (factor of η_i) of the total current. It accounts for the carrier dynamic process within the active region. The leaking current is the excess current flow that is wasted in the device. There are two major channels for the leaking current: non-radiative recombination outside the active region and carrier overflow when the carriers escape from the active region.

In the steady state, the carrier change rate becomes zero. The carrier injected into the active region converted to the recombination and stimulated emission processes. With a given injection current, the recombination and stimulated emission are competing to consume the carriers. Therefore, there are several approaches to save more carriers for stimulated emission: reduce the leakage current and increase the injection efficiency and reduce the defects density in the active region. The radiative and Auger recombinations are intrinsic semiconductor characteristics, which is will not further discuss here.

1.5 Development strategy of GeSn lasers

There is no doubt that the GeSn lasers remain a significant portion to be improved. The

operating temperature is still well below the room temperature (180 K by the start of the dissertation). The laser threshold needs to be further reduced. But more importantly, it is highly interested in developing the electrically injected GeSn lasers. For the basic laser design, three major factors should be considered: i) the carrier injection efficiency into the GeSn active region; ii) the material gain in the active region; iii) the optical loss in the device. The following strategy closely involved in these three factors.

Recent GeSn growth by using CVD, the defects are mainly from the threading dislocations and vacancies in the strained layer. The direct bandgap GeSn epitaxial growth adopts the prerequisite Ge and GeSn buffer. Such buffer layers are designed for strain relaxation and neutralization of the threading dislocations. The resulted GeSn epitaxial layer on top of the buffers can be maintained at a decent quality. However, the buffer layers, especially the GeSn buffer, remain highly defective, which needs to be kept away from the active region in the laser device. Research on defect removal using microdisk lasers showed promising results by under etched the bottom defective buffer layer. Growing thick GeSn buffer would be an alternative way to keep a large volume of GeSn having high quality.

The SiGeSn material system has Γ and L valley in the conduction band. The two valleys minima share similar energy levels and accumulate the electrons as band edge. However, only electrons in the Γ valley have a high radiative recombination rate. This is because the electrons in the Γ valley share the same momentum with holes. On the other hand, the electrons in L valley have a large momentum difference to the holes in the valence band. This difference makes electrons extremely rare to recombine with holes radiatively since the transition requires interactions with phonons to conserve the momentum. The direct bandgap material has Γ valley minimum being the lowest energy level in the conduction band. The direct bandgap material has

a high probability of radiative recombination. In the direct bandgap SiGeSn material system, the electrons populate in both L and Γ valley if the carrier injection is high, or the L and Γ valley minima are close. This electron population in L valley dilutes the carrier density within the Γ valley, causing a lower probability of radiative recombination.

Increasing Sn composition is one of the key methods to make the energy difference larger between L and Γ valley minima. As a result, higher electron density could be achieved in Γ valley for efficient light emission through radiative recombination.

As mentioned earlier in this section, strain affects the band edge position. In the SiGeSn material system, the compressively strained material tends to have reduced energy difference between L and Γ valley minima compared to the relaxed film. In this situation, the compressive strain negatively affects the light emission in reducing the electron density in the Γ valley. On the other hand, the tensile strain would further increase the energy difference between L and Γ valley minima. Therefore, the electron density in Γ valley could be increased compared to the relaxed film. Typically, the GeSn epitaxial layer for light emission normally has high Sn composition. The larger lattice constant in GeSn layer yields to a compressive strain when the layer grows on top of the Ge buffer. Therefore, the relaxation of the GeSn active layer would promise an improved performance for the light-emitting device.

In this dissertation, the valence band alignment is discussed to bring attention to the hole leakage. The small or negative barrier height for GeSn DHS yields to the carrier leaking channel. The composition and strain are therefore re-designed so that to prevent the hole leakage through this channel.

With the carrier injection, double heterostructure is used to confine the carriers within the active region. Compared to the GeSn barrier, the SiGeSn barrier would increase the energy

barrier height compared to the GeSn barriers, which effectively maintains a high carrier density in the active region.

1.6 Scope of this dissertation

This dissertation presents the development efforts of GeSn lasers, from optically pumping to electrical injection. The chapters cover several device forms, including optically pumped GeSn lasers using bulk and MQW gain as the gain region. By investigating the performance of the optically pumped lasers and the LEDs, the DHS structure and active region characteristics are studied and optimized. Such experience applies to the design of GeSn laser diodes, leading to the successful demonstration of electrically injected lasers. Further development paths are further discussed.

Chapter 2 shows the characteristics of the optically pumped GeSn lasers. The GeSn bulk lasers with high Sn composition were characterized at low temperatures. The elevated T_{max} was achieved from the higher Sn composition devices. The T_{max} was achieved as high as 270 K was recorded from the devices with 20% Sn in the active region. The ridge waveguide and microdisk lasers were compared and analyzed by using the same gain structure.

Chapter 3 describes the lasing from GeSn MQW structure was observed at temperatures up to 90 K. The performance of MQW lasers was evaluated with the tuning of the SiGeSn cap layer and well number.

Chapter 4 introduces the preparation study towards the GeSn electrically injected laser. The preparation adopts the GeSn LED devices, which offer the radiative recombination and the carrier injection mechanism in DHS using the GeSn LEDs. The performance of the optically pumped laser applies here for the electroluminescence (EL) as the prior step towards the laser

diodes. Three generations of LED design yield the reduction of non-radiative recombination and improvement of the carrier injection efficiency.

Chapter 5 demonstrates electrically injected GeSn diode lasers. After the improvement of the carrier injection in the LEDs, the laser diode is designed correspondingly into the waveguide laser structure. The high-quality GeSn gain region was achieved in the DHS with high Sn composition while maintaining a low compressive strain level. The developed DHSs were adopted into ridge waveguide diode laser. Lasing under electrical injection was demonstrated at temperatures up to 100 K with a minimum threshold of 0.6 kA/cm^2 at 10 K. The characteristics of the laser diodes were further evaluated by changing the DHS cap layer and active region material and thickness.

Chapter 6 summarizes the results and proposes the future improvement direction of GeSn lasers towards the room-temperature continuous-wave operation.

Chapter 2: Optically pumped bulk GeSn lasers

In this chapter, lasing characteristics from GeSn bulk laser are discussed by using the optically pumping method. This chapter aims to explore the device approaches to improve GeSn laser performance, specifically in increasing the maximum operating temperature.

The optically pumping method directly introduces the light into the GeSn devices from the top surface. Consequently, the light is absorbed leading to the generation of the carriers. In this chapter, the bulk GeSn epitaxial was fabricated into laser devices using ridge waveguide, planar waveguide, index guide waveguide, and microdisk structure. The broad ridge waveguide structure shows a higher laser operating temperature up to 270 K, by using a GeSn gain region with Sn composition of 20%.

2.1 Broad ridge waveguide lasers with a high Sn composition

In this work, GeSn lasers based on the ridge and planar waveguide structures are investigated via optical pumping. The 20% Sn composition yields direct bandgap GeSn alloy with its Γ valley sitting more than 100 meV below its L valley in the conduction band. The maximum lasing operation temperature was achieved at 270 K, evidenced by the laser-output versus pumping-laser-input (L-L) curves and the emission spectra. The lowest lasing threshold was obtained from the 100-μm-width ridge waveguide structure. Further analysis revealed that the improved local heating dissipation and reduced surface recombination of the 100-μm-width ridge device led to the high lasing operation temperature and lower threshold. With the current lasing temperature being close to the room temperature, it is essential in the future to switch from the bulk to more advanced device structures such as MQWs for electrical injection operation, as suggested in Ref. 29 that with a possible active region design of 20 SiGeSn/GeSn QWs.

The GeSn sample was grown on a relaxed Ge buffer (nominal 700-nm-thick) on a Si substrate using an industry-standard ASM (ASM international, Almere, NL) Epsilon® 2000 PLUS reduced pressure chemical vapor deposition (RPCVD) reactor with commercially available precursors of GeH_4 and $SnCl_4$. A multiple-step Sn-enhanced growth recipe was used to achieve a 20% final Sn composition, which was developed and reported in the previous study regarding the spontaneous-relaxation-enhanced (SRE) Sn incorporation process [37]. Note that by using the compensated Sn incorporation approach, i.e., adjusting the $SnCl_4$ flow to compensate the increased Sn incorporation, the constant Sn incorporation can be achieved [43]. After growth, Sn composition was determined by secondary ion mass spectrometry (SIMS); the strain was extracted by reciprocal space mapping (RSM) of X-ray diffraction (XRD) measurement; the GeSn thickness and material quality were studied by transmission electron microscopy (TEM) image. The SIMS and XRD 2θ-ω scan were also used to cross-check the layer thicknesses and the Sn compositions.

GeSn sample growth: A 750-nm-thick Ge buffer layer was first grown on Si followed by an in-situ annealing to reduce the defects. A nominal 11% Sn based recipe was used to initiate the GeSn growth. The Sn incorporation starts from 11%. As the GeSn grows thicker, the gradually relaxed material leads to the Sn incorporation in subsequent GeSn layer increases until 15% with a grading rate of 17.4%/μm. This is the 1st GeSn layer, in which the formation of threading dislocation loops prevents the defects from being propagated to the subsequent 2nd GeSn layer. As the material almost fully relaxes, the Sn incorporation increases with a grading rate of 5.2%/μm, until the final Sn composition of 20% was achieved. This is the 2nd GeSn layer featuring low defect density.

Photoluminescence (PL) measurements: The PL measurements were performed using a

standard off-axis configuration with a lock-in technique (optically chopped at 377 Hz). A 532 nm continuous wave (CW) laser was used as an excitation source. The laser beam was focused down to a 100-μm-diam spot with the measured power of 100 mW. The PL emission was collected by a spectrometer and then was sent to an InSb detector with response cut-off at 5.0 μm.

Optical pumping measurements: The optical pumping characterization was performed using two pulsed laser excitation sources: i) a 1064 nm laser with 10 kHz repetition rate and 2 ns pulse width; and ii) a 1950 nm laser with 10 kHz repetition rate and 20 ns pulse width. The laser beam was collimated to a narrow stripe (~20 μm width and 0.3 cm length) via a cylindrical lens to pump the GeSn waveguide devices. The device was first mounted on a Si chip carrier and then placed into a continuous flow cryostat for low-temperature measurement. The emission from the facet was collected by a spectrometer and then sent to an InSb detector. The integrated emission intensity was measured by setting the grating at zero order.

Figure 5 shows the high-resolution TEM image of the sample. The Ge and GeSn layers are clearly shown. For GeSn alloy, two distinct layers can be observed, as marked as the 1st and 2nd layers with the thicknesses of 450 nm and 970 nm, respectively. The 1st layer over the Ge buffer is defective due to the relatively high threading dislocation density (TDD) because of lattice mismatch between Ge and GeSn. However, the formation of threading dislocation loops in the 1st GeSn layer prevents the defects from propagating into the 2nd GeSn layer, as shown in Fig. 5(a). As a result, the 2nd GeSn layer exhibits relatively low TDD of 106 cm-2 according to the etch pit density measurement. The formation mechanism of threading dislocation loops was discussed in the previous studies [44,45].

The SIMS result is shown in Fig. 5(b). Three regions can be resolved based on Sn

incorporation: i) region I with the constant Sn composition of 11% and thickness of 200 nm; (ii) region II with the Sn-composition grading rate of 17.4%/μm and thickness of 230 nm, leading to increase of Sn composition from 11% to 15%; iii) region III with the Sn-composition grading rate of 5.2%/μm and thickness of 970 nm, resulting in maximum Sn incorporation of 20% at the surface. The graded Sn incorporation can be explained as the following: the GeSn growth starts with a nominal 11% Sn recipe, once the layer thickness reaches its critical thickness, the gradual relaxation of the material facilitates more Sn incorporation, resulting in subsequent Sn incorporation in the GeSn layer increases to 20%. Note that the combination of regions I and II corresponds to 1st layer observed in TEM, while the region III corresponds to 2nd layer.

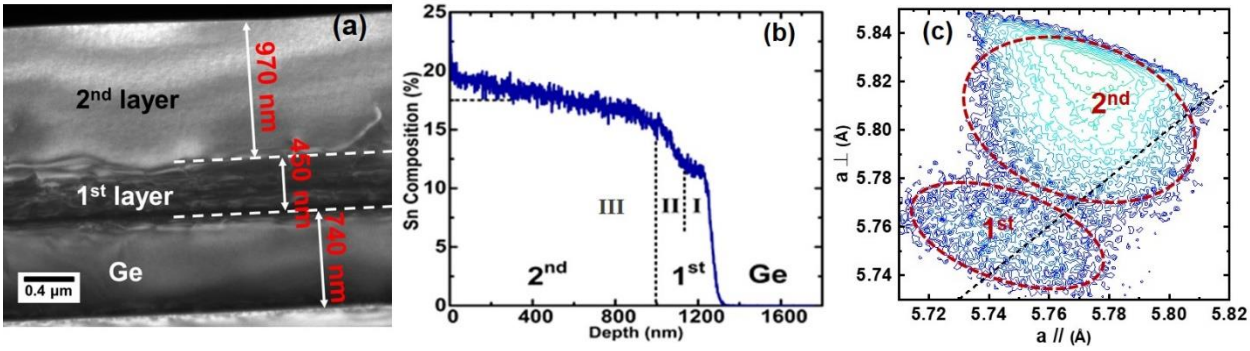

Figure 5. (a)TEM image of sample showing 1st defective relaxing layer and 2nd high quality GeSn top layer, which acts as the gain region. (b) SIMS profile of Sn composition with the three regions indicated: (c) XRD RSM contour map showing the graded Sn composition in 1st and 2nd GeSn layers. Reprinted with permission from [46]. Copyright 2020 American Chemical Society.

Figure 5(c) shows the RSM contour plot of the GeSn. The 1st and 2nd layers can be clearly resolved. The dashed line indicates the strain relaxation line. The broadened contour plot is mainly due to the graded Sn compositions in each layer. Since it is very difficult to pinpoint the strain at a specific point due to the graded Sn composition, the averaged strain at each GeSn layer was extracted, as -0.10% and -0.52% for the 1st and 2nd layer, respectively.

Band structure calculation: Based on the obtained Sn composition, strain, and layer

thickness, the band diagram at 300 K was calculated using the effective mass and matrix propagation method [28,47]. The strain-induced bandgap change was considered for the calculations [48]. Figure 6 shows the schematic band structure. Four subbands were considered including indirect (E_{cL}) and direct ($E_{c\Gamma}$) valleys in the conduction band (CB) and heavy hole band (E_{vHH}) and light hole band (E_{vLH}) in the valence band (VB). The variations (indicated by shadow areas) of E_{cL} and $E_{c\Gamma}$ originate from the different adoptions of bowing parameters [49-52]. Since both GeSn bottom and top layers are compressively strained, the E_{vHH} band is above the E_{vLH} band. The whole GeSn layer exhibits the direct bandgap characteristics because of high-Sn incorporation even with partially compressive strain. Due to that the Sn composition increases towards the surface, the decrease of both Γ (direct) and L (indirect) valleys with the direct one more rapidly than the indirect one was observed. At surface (20% Sn region), the bandgap was calculated ranging from 0.21 to 0.31 eV. While the PL peak at 300 K was measured at 3460 nm (0.358 eV), the discrepancy might be mainly due to the inaccurate bowing parameters, which are currently unavailable for high Sn alloy currently.

The temperature-dependent PL measurements were performed using a 532-nm excitation laser to study the optical property of the GeSn layer. Figure 7(a) shows the temperature-dependent PL spectra. As the temperature decreases from 300 K to 10 K, the PL intensity significantly increases, indicating the unambiguous signature of the direct bandgap material. The "three peaks" feature in PL spectra is due to the H_2O and CH_4 absorptions at 3.0 μm and 3.2 μm, respectively, which result in two valleys in spectra. The PL peak blue-shift following the Varshni empirical model was observed as expected. Note that the optical transitions, i.e., light absorption and emission are mainly limited to the near-surface region, where the Sn composition is ~20%. This is due to: i) the penetration depth of the 532-nm excitation laser is less than 50

nm; and ii) the photogenerated carriers tend to transport from the wider bandgap region (GeSn region away from the surface) to the narrower bandgap region (surface) as the result of the graded Sn composition. Further PL peak analysis was conducted using Lorentzian function fitting. From 300 to 10 K, the integrated PL intensity increases up to 35 times and the PL peak full width half maximum (FWHM) decreases rapidly from 74 to 28 meV, as shown in Fig. 7(b), suggesting that the PL emission originates from the band-to-band radiative recombination in the direct bandgap.

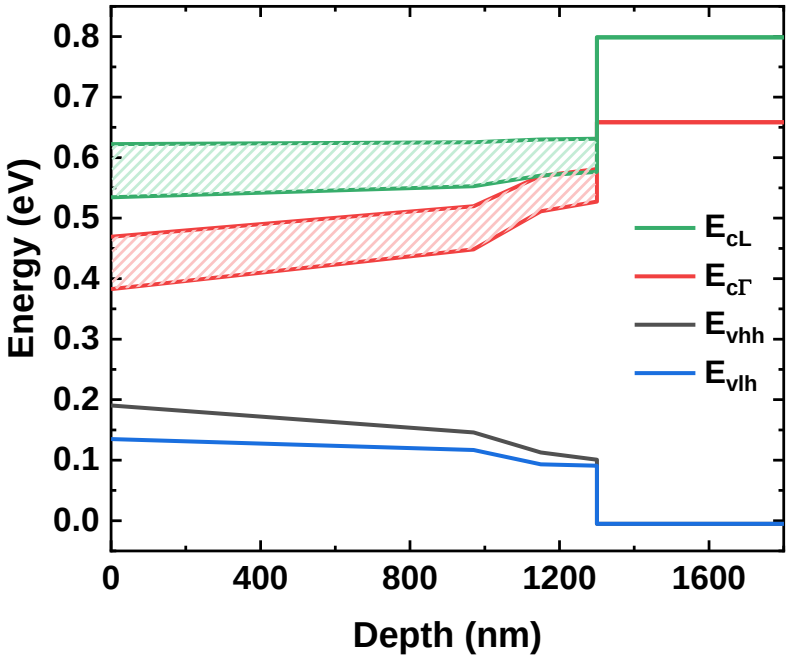

Figure 6. Band structure calculated at 300 K. Reprinted with permission from [46]. Copyright 2020 American Chemical Society.

Laser devices based on the ridge and planar waveguide structures were investigated. The ridge waveguides with ridge widths of 5, 20, and 100 μm (annotated as devices A, B, and C) were fabricated by standard photolithography and wet chemical etching processes that were developed by previous work [35] while the planar structure (annotated as device D) was not

etched at all. The etching depth was selected as 800 nm to provide sufficient mode confinement. All samples including ridge and planar waveguides were lapped down to ~70 μm thickness and then cleaved to form the cavity with the lengths of 2750 (device A, B and C) and 2650 μm (devices D).

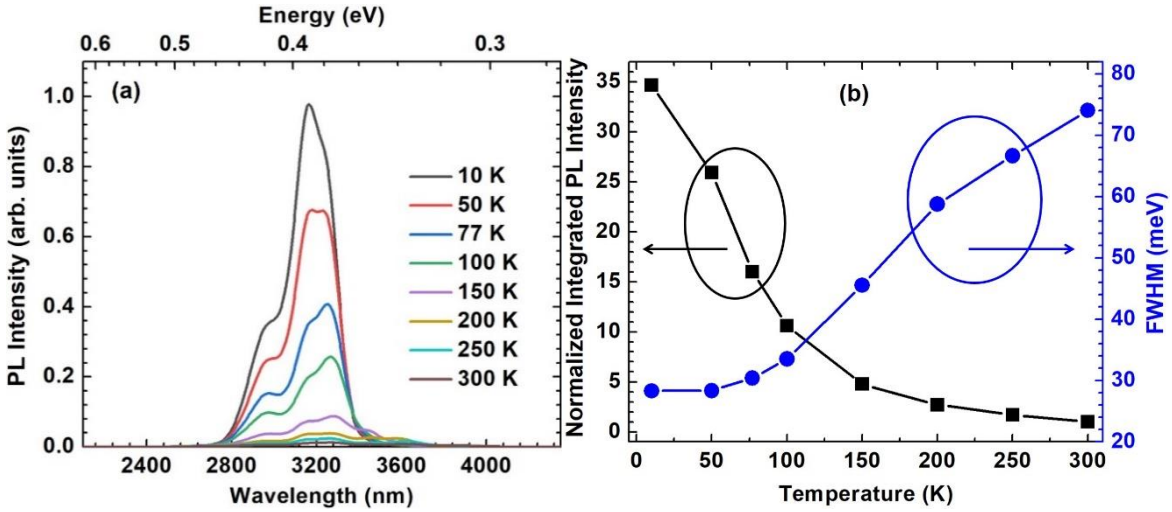

Figure 7. (a) Temperature-dependent PL spectra using 532 nm CW laser pumping. (b) Temperature-dependent FWHM and normalized integrated intensity of PL spectra. Reprinted with permission from [46]. Copyright 2020 American Chemical Society.

The optical pumping characterization was performed using two excitation sources: a pulsed 1064-nm laser and a pulsed 1950-nm laser. To accurately calculate the effective light absorption for each device as they feature different ridge width, the cross-sectional profile of the pumping laser beam was measured, as shown in Fig. 8. The pumping power density was calculated in the following way: cross-sectional profile of each laser beam was measured and then fitted using Lorentzian function. For the device whose ridge width is smaller than the FWHM of the laser beam, the overall pumping power intensity was calculated by the integral of power within the ridge region divided by the product of ridge width and cavity length. For the device whose ridge width is wider than the FWHM including the planar waveguide device, the

pumping power density was calculated according to total excitation power / FWHM. The effective light absorption for each device is summarized in Table 1.

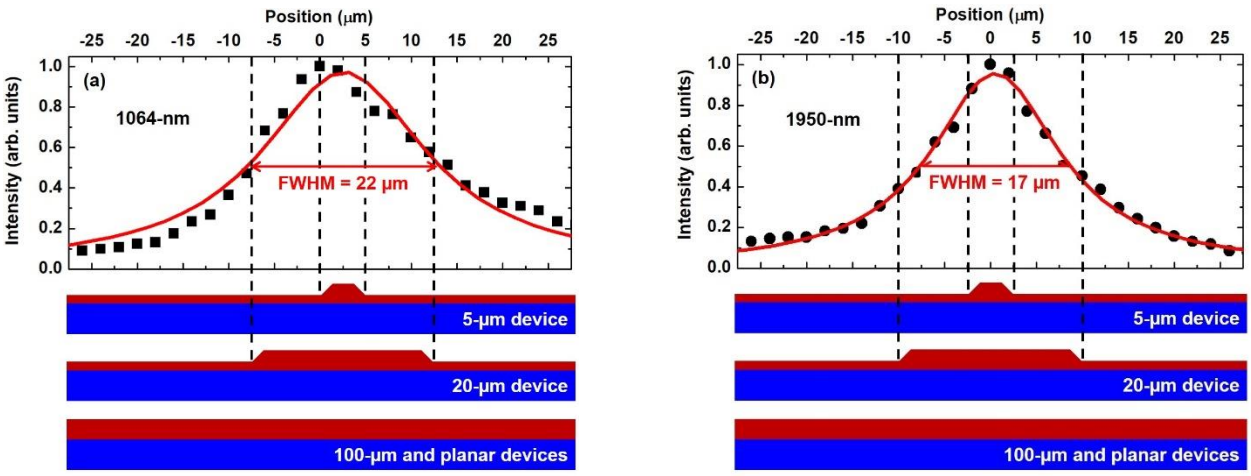

Figure 8. (a) 1064-nm and (b) 1950-nm pumping laser beam profile compared with devices with different ridge widths. Reprinted with permission from [46]. Copyright 2020 American Chemical Society.

Table 1. Spatial overlap percentage between device and pump laser calculated from beam spot profile and device geometry. Reprinted with permission from [46]. Copyright 2020 American Chemical Society.

	Device A	Device B	Device C	Device D
Ridge width	5 μm	20 μm	100 μm	Planar
1064 nm laser	14.2%	47.0%	86.2%	100%
1950 nm laser	18.2%	55.2%	89.3%	100%

Lasing mode pattern calculation: The mode calculation was performed using a 2D mode solver. Figure 9 shows the typical pattern of the fundamental transverse electric (TE_0) modes for devices A, B, and C. Since the refractive index exhibits only a slight increase as Sn compositions increase from 10% to 20%, an identical refractive index of 4.25 was used for the entire GeSn layer. The modal overlap with the high-quality GeSn top layer is calculated as

64.9%, 65.4%, 65.4% and 65.6% for devices A, B, C, and D (D was not shown) respectively. Note that the 90° sidewall rather than sloped sidewall was used for simulation. Based on the previous study, less than 1% difference between the two cases, and therefore can be ignored.

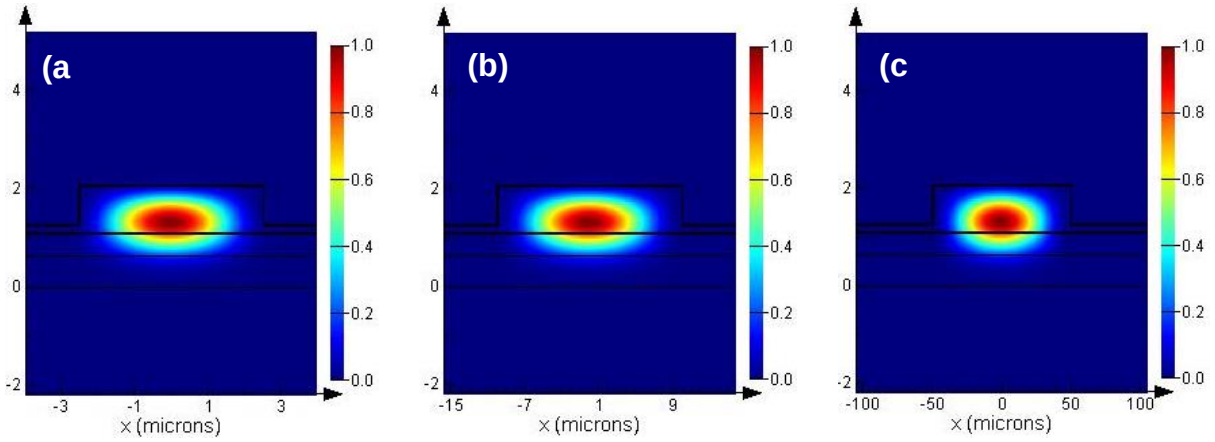

Figure 9. Optical Mode of TE00 mode calculated for devices (a) A (5 μm); (b) B (20 μm); and (c) C (100 μm). The modal overlap with the high-quality GeSn top layer is calculated as 64.9%, 65.4%, and 65.4% for devices A, B, and C, respectively. Reprinted with permission from [46]. Copyright 2020 American Chemical Society.

SEM image of the device: SEM images are shown in Fig. 10. The sloped sidewall was observed, as shown in Fig. 10(a). The cleaved facet is shown in Fig. 10(b). By reducing the sidewall roughness which could reduce the scattering loss, the improved lasing performance can be expected.

The optical pumping characterization was firstly performed using a pulsed 1064 nm laser. The L-L curves for each sample were measured from 77 K to its maximum operating temperature. The typical L-L curves at different temperatures are shown in Fig. 11(a) for device C. At 77 K, the lasing thresholds were extracted as 516, 384, 356, and 330 kW/cm2 for devices A, B, C, and D, respectively (Fig. 11(b)), exhibiting lower thresholds of wider ridge devices B, C and D than that of device A. Note that the spatial distribution of the light

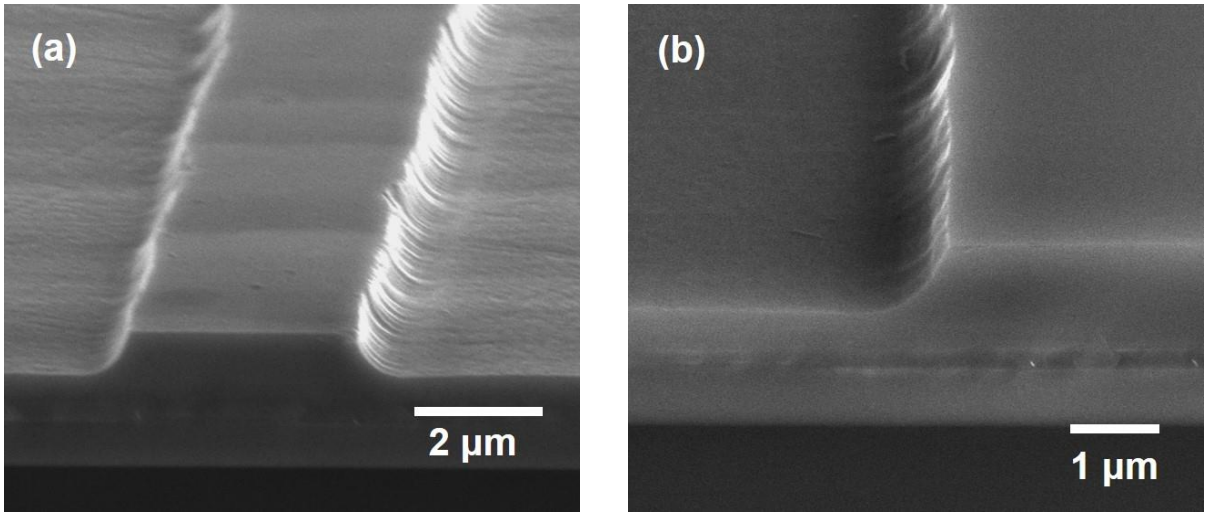

Figure 10. SEM image of waveguide laser device A. (a) waveguide ridge; (b) cleaved facet. Reprinted with permission from [46]. Copyright 2020 American Chemical Society.

shown in Table I was considered for the threshold calculations. Moreover, since the excitation is not uniform, the net positive gain may be achieved in the middle of the waveguide but not at the edges, resulting in the enhanced spontaneous emission and consequently the gradual transition of threshold behavior. The reduced threshold with wider ridge devices could be attributed to the reduced surface recombination: the increase of ridge width leads to less effect from the sidewall surface recombination. For device A, the maximum operating temperature was measured at 120 K; while for devices B, C, and D, 260 K lasing temperature was obtained (Fig. 11(c)), which is higher than previously reported highest ridge waveguide lasers (180 K) [35] and microdisk lasers (230 K) [38]. The higher operating temperature obtained is mainly due to the high material quality that was achieved using the unique growth recipe30 as well as the 65.4% modal overlap (for B and C. For A: 64.9%; D: 65.6%) with the low TDD GeSn gain region. Moreover, the increased operating temperature of devices B, C, and D featuring wider ridges and/or planar structure is made possible thanks to the improved heat dissipation compared to device A that with a narrower ridge, suffering from the enhanced free carrier absorption (FCA). At 260 K, the

lasing thresholds were extracted as 2990, 6055, and 9587 kW/cm2 for devices B, C, and D, respectively, showing the trend of threshold increase as ridge width increases. This can be interpreted by that: i) the dramatically increased FCA and non-radiative recombination at higher temperature dominate the loss over the sidewall surface recombination; ii) the inhomogeneous excitation for a wider cavity device could result in achieving gain in the middle of the waveguide but not at the edges, where light absorption could occur; and iii) the less optical confinement of sample D also leads to its higher threshold.

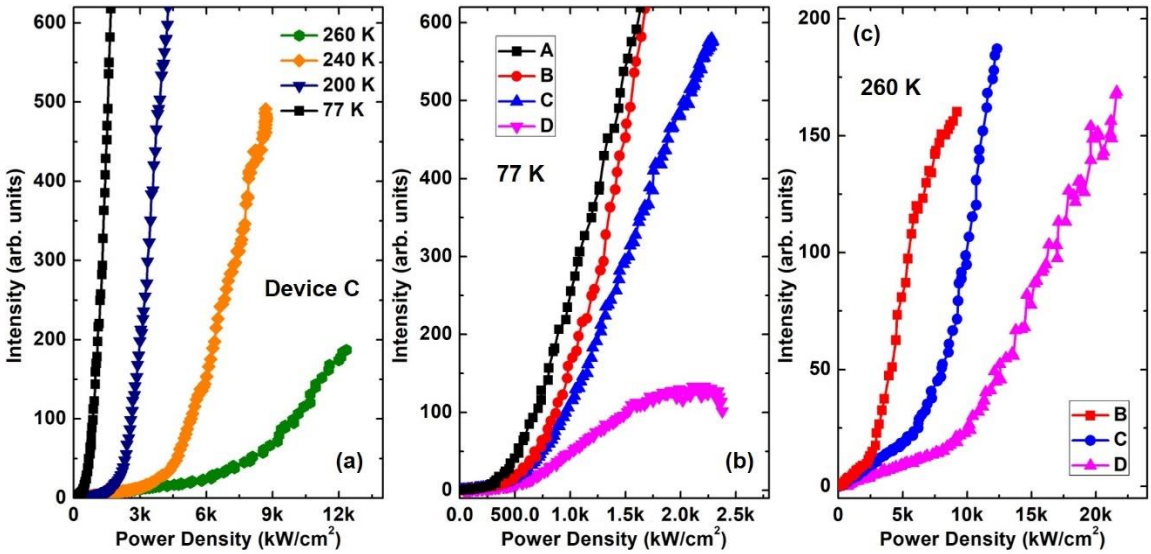

Figure 11. L-L curves under 1064 nm laser excitation. (a) from 77 to 260 K for device C; (b) all devices at 77 K; and (c) devices B, C, and D at 260 K. Reprinted with permission from [46]. Copyright 2020 American Chemical Society.

Lasing spectra were measured at 2-times lasing threshold pumping power density of each sample. Due to the relatively large area of the cavity facet, the typical multimode lasing characteristic was observed for each device. In Fig. 12, each resolved peak consists of multiple peaks that are mostly overlapped, which cannot be further identified from the spectrum owing to the resolution limit of the spectrometer of ~0.1 nm considering the transverse and longitudinal mode spacings of 0.01 and 1.3 nm, respectively. Despite the mode overlapping, the FWHM of

each resolved peak was estimated as ~2 to 3 meV. Compared with the FWHM of PL spectra at 10 K of 23 meV shown in Fig. 7, the significantly decreased FWHM indicates the unambiguous signature of lasing.

At 77 K, the lasing wavelengths were obtained from 2641 to 2961 nm for devices A-D. Compared with the PL peak at 3250 nm at 77 K, the clear peak blue-shift was observed, which might be interpreted as the typical band-filling effect dominant under intense injection. Device A exhibits more blue-shift than the other three samples due to the higher pumping power density that results in higher energy levels being populated by carriers in both conduction and valence bands. As temperature increases from 77 to 260 K, the lasing peak all shifts towards longer wavelength for devices B, C, and D as expected. It is worth noting that as the temperature increases from 77 K, the separation between lasing and PL peak gradually reduces, and eventually the lasing peak occurs at a longer wavelength than PL peak beyond 160 K. At 260 K, the lasing peaks for devices B, C, and D locate at ~3330 nm, which is longer than PL peak. This might be explained as follows: the main factors affecting the lasing peak shift include: i) the higher pumping intensity compared to that in PL measurement results in the high density of carriers that contributes to the band-filling effect which in turn results in the blue-shift of the lasing peaks; ii) the increased temperature leads to the red-shift of lasing peak; and iii) the shift of gain spectrum due to bandgap altering with temperature results in the lasing peak shift. Note that other factors such as refractive index altering with temperature could also affect the lasing position. Therefore, the lasing peak shift is an overall effect of competition among the factors above-mentioned. At lower temperatures, the band-filling effect could dominate the peak shift, results in the overall blue-shift; while at higher temperatures, the increased temperature might become the dominant factor, as a result, the overall red-shift was observed. For device C, the 77

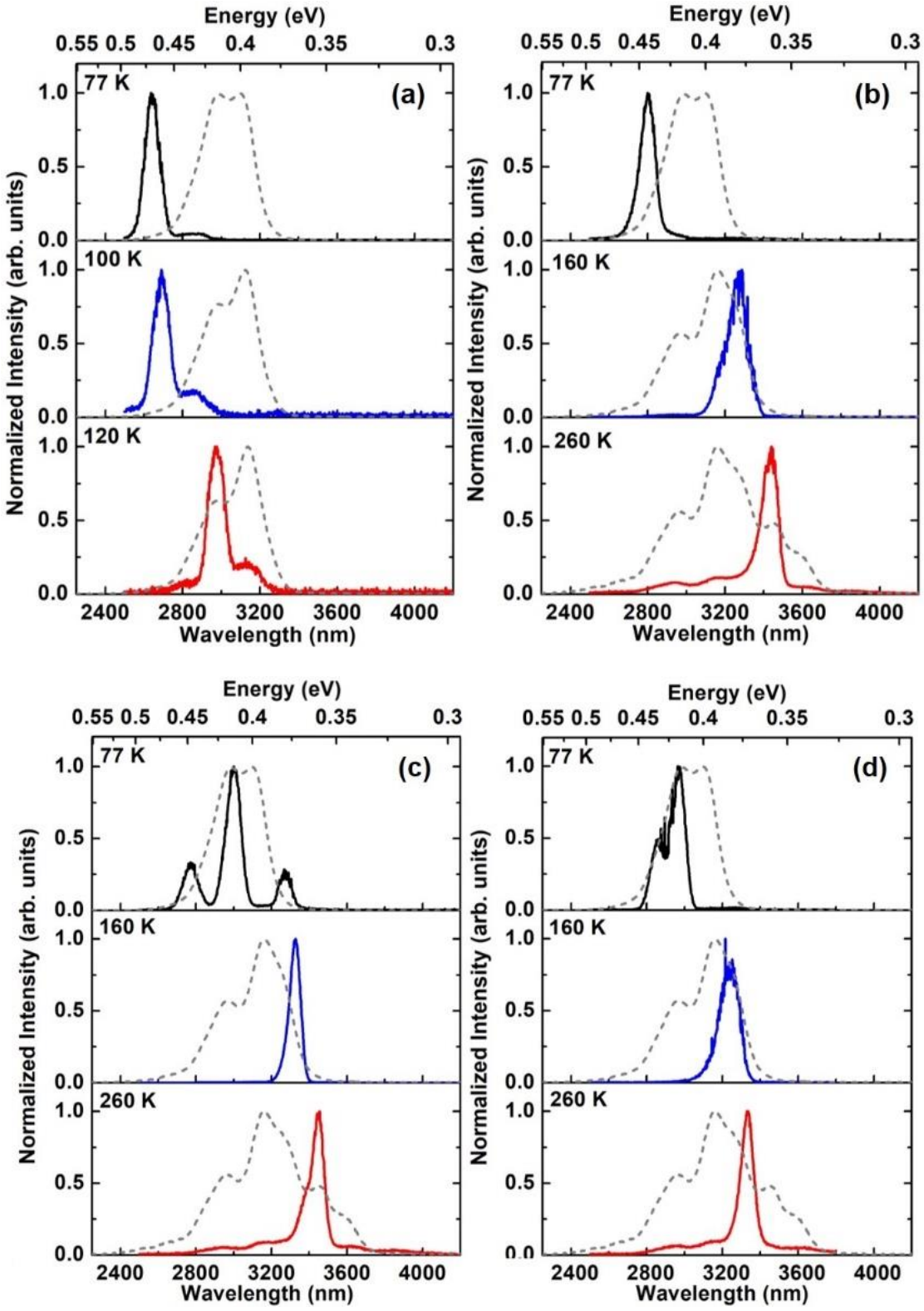

Figure 12. Lasing spectra at 2 × threshold under the excitation of 1064 nm laser for devices (a) A; (b) B; (c) C; and (d) D. The PL spectra (dashed curves) are also plotted for comparison. Reprinted with permission from [46]. Copyright 2020 American Chemical Society.

K spectrum shows two more peaks at ~2750 and ~3300 nm in addition to the main lasing peak, which might be due to the non-uniform distribution of the modal gain at 77 K, leading to extra enhanced modes in the lasing output. The similar peak feature can also be observed from device D at 77 K and around ~2800 nm, as shown in Fig. 11(d).

The peak linewidth was extracted using data fitting method: The analysis of the lasing spectrum of device D at 200 K was shown here as an example. Figure 13(a) shows the enlarged spectrum, where the multi-peak feature can be observed. The clearly resolved peaks (numbered as 1, 2, 3 and 4) were fitted using Gaussian function. The peak linewidth was then extracted from the fitted Gaussian peak. Note that based on the theoretical calculation, the longitudinal mode spacing is ~1.3 nm, while the transverse mode spacing is in the order of ~0.01 nm. Each observed peak consists of multiple peaks that are mostly overlapped. Due to the resolution limit of 0.1 nm of the spectrometer, these modes cannot be further identified from the spectrum.

The lasing threshold was extracted as following, as shown in Fig. 13(b) as example (device D at 200 K): selecting the data points with the power density above "knee" point, fitting the data with linear curve. The threshold can be obtained by the y-axis-intercept with the fitting curve. In Fig. 13(b), the threshold of 340 kW/cm^2 was obtained. In this work, all lasing

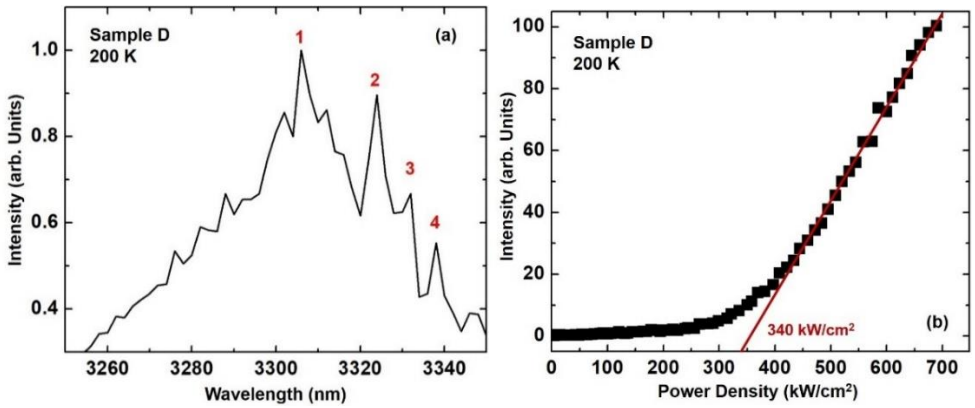

Figure 13. (a) Lasing spectrum of device D at 200 K. (b) Lasing threshold extraction method. Reprinted with permission from [46]. Copyright 2020 American Chemical Society.

thresholds were extracted using the same method.

Laser characterization using 1950 nm excitation source. Since the pumping photon energy of 1064 nm laser (1.165 eV) is much higher than the emission photon energy (less than 0.469 eV), the large quantum defect, i.e., the energy difference between absorbed and emitted photons could lead to deterioration of lasing performance by local heating. To reduce the impact of the quantum defect on lasing characteristics, a 1950-nm laser was used as the excitation source.

Figure 14(a) shows the typical L-L curves at different temperatures for device C. For device A, the maximum operating temperature increases from 120 to 140 K; while for devices B, C, and D, their maximum operating temperatures are increased to near room temperature at 270 K. At 77 K, the lasing thresholds were extracted as 132, 88, 47, 74 kW/cm2 for devices A, B, C, and D, respectively, much smaller than those under 1064-nm laser excitation even with a lower absorption coefficient of 1950 nm. We attribute the increased operating temperature and dramatically reduced thresholds to the following: the quantum defect of ~170 meV is 45%

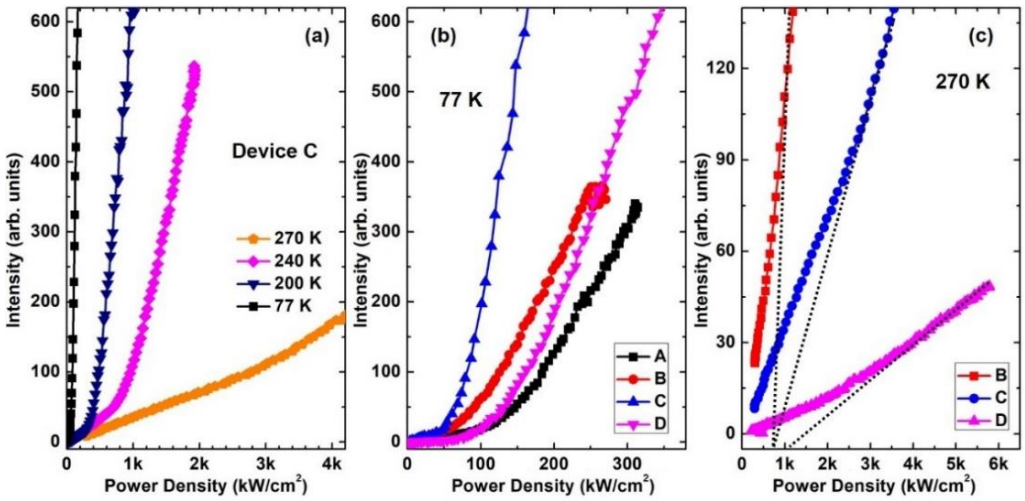

Figure 14. L-L curves under 1950 nm laser excitation. (a) from 77 to 270 K for device C; (b) all devices at 77 K; and (c) devices B, C, and D at 270 K. The dotted lines indicate the method of threshold extraction. Reprinted with permission from [46]. Copyright 2020 American Chemical Society.

smaller for the 1950-nm laser compared to the 1064-nm laser of ~700 meV, and results in less excess phonon energy being converted into thermal energy under the 1950-nm pumping. For devices B, C, and D, the thresholds at their maximum operating temperatures are measured as 886, 796, and 1105 kW/cm2, respectively.

Figure 15 shows the lasing spectra measured at 2-times lasing threshold pumping power density for each device. The multimode lasing characteristic was observed at each temperature. At 77 K, the lasing wavelengths were obtained from 2700 to 3270 nm for four devices. In Figs. 15(b) and 15(c), the peak at ~3005 nm is possibly due to the non-uniform distribution of modal gain that was observed under 1064-nm laser pumping as well. Note that the peak at ~3900 nm is the artifact due to the second order diffraction of the 1950-nm pumping laser. For devices B, C, and D, the similar blue-shift of the lasing peak at a lower temperature and red-shift at a higher temperature relative to PL peak were observed, as the result of the band-filling effect and local heating effect being dominant at low and high temperatures, respectively. The lasing peaks at 3350~3450 nm were obtained for devices B, C, and D at their maximum operating temperature of 270 K, respectively. The lasing characterization results are summarized in Table 2.

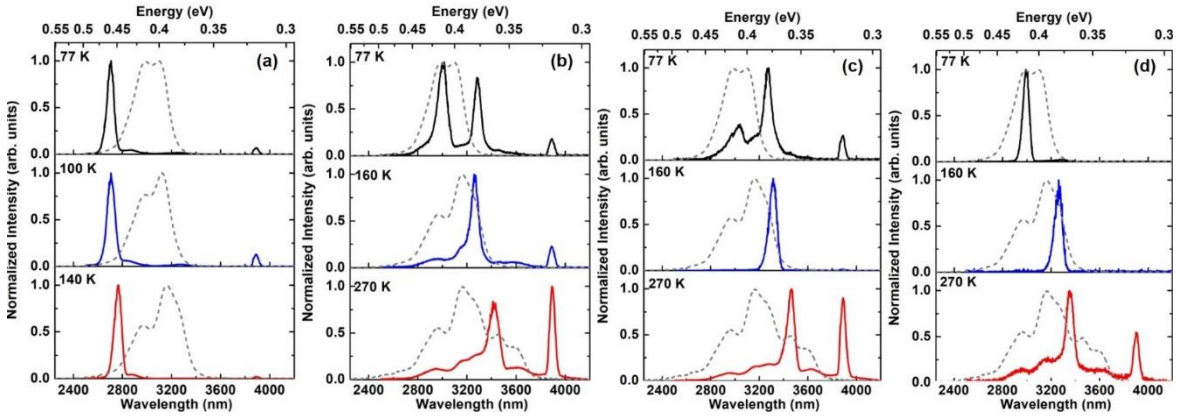

Figure 15. Lasing spectra at 2 × threshold under the excitation of 1950 nm laser for devices (a) A; (b) B; (c) C; and (d) D. The PL spectra (dashed curves) are also plotted for comparison. Reprinted with permission from [46]. Copyright 2020 American Chemical Society.

Emission spectra below and above threshold: Emission spectra at 0.8 × threshold and 2 × threshold for each device at maximum operating temperature are shown in Fig. 16. Below the threshold, only background PL emission can be seen; while above the threshold, the unambiguous lasing peak can be observed.

Table 2. Summary of lasing characterization Reprinted with permission from [46]. Copyright 2020 American Chemical Society.

1064-nm pumping	A (5 μm)	B (20 μm)	C (100 μm)	D (Planar)
Threshold @77K (kW/cm^2)	516	384	356	330
Peak position @77K (nm)	2641	2802	2965	2961
Maximum Operating Temperature (K)	120	260	260	260
Threshold @ Maximum Operating Temperature (kW/cm^2)	903	2990	6055	9587
Peak position @ Maximum Operating Temperature (nm)	2970	3432	3444	3334
1950-nm pumping	A (5 μm)	B (20 μm)	C (100 μm)	D (Planar)
Threshold @77K (kW/cm^2)	132	88	47	74
Peak position @77K (nm)	2703	3022	3272	2997
Maximum Operating Temperature (K)	140	270	270	270
Threshold @ Maximum Operating Temperature (kW/cm^2)	364	886	796	1105
Peak position @ Maximum Operating Temperature (nm)	2780	3414	3462	3354

L-L curves plotted in log-scale: Figure 17 shows the typical L-L curves on a log-log scale. The typical S-shape can be observed at 77 K, confirming the lasing characteristic. As temperature increases, the L-L curve shows weak S-shape. At 260 K under 1064 nm laser pumping, the S-

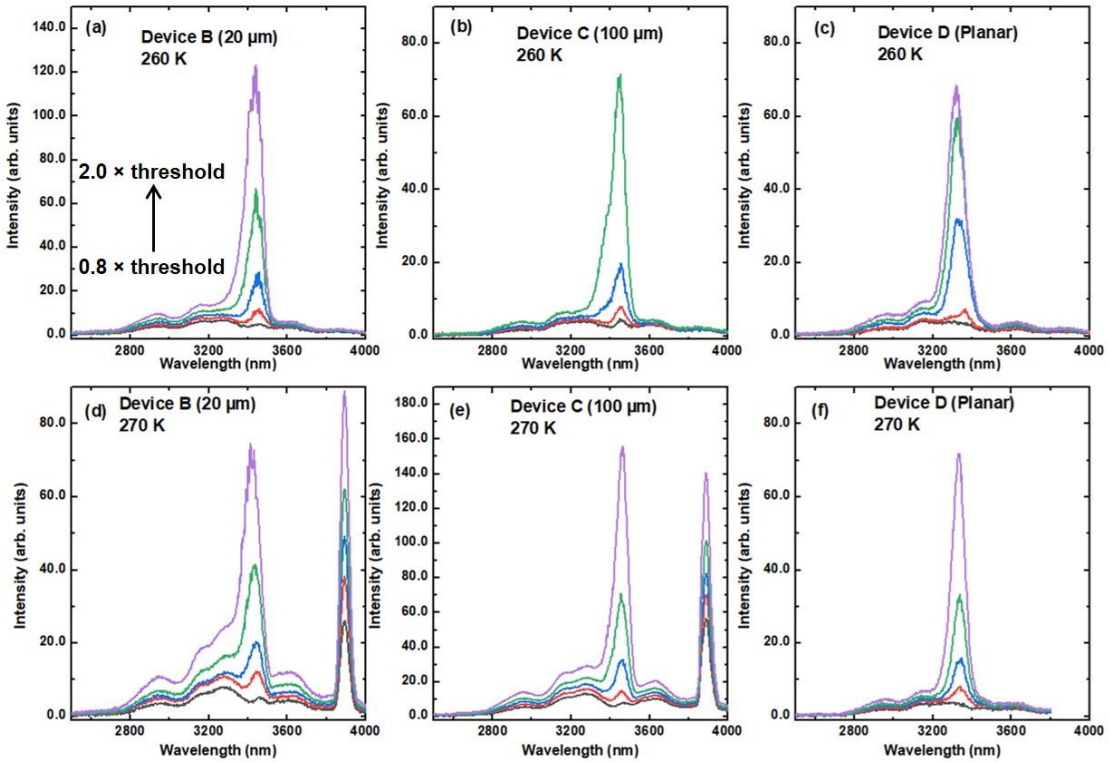

Figure 16. Lasing spectra at maximum operating temperatures for Devices B, C, and D under excitation from 0.8 × to 2.0 × threshold. The peak at 3900 nm is an artifact due to the second order diffraction of the grating-based spectrometer for the1950-nm. Reprinted with permission from [46]. Copyright 2020 American Chemical Society.

shape feature can still be observed. At 270 K under 1950 nm laser pumping, it is hard to see the S-shape. The lasing at 270 K is confirmed by the threshold feature and the emission spectra.

Stimulated emission study at 280 K: Device C was selected for further optical pumping characterization at 280 K. Under pumping power density of 3.1 MW/cm2, the spontaneous emission dominates the spectrum (the 3900-nm peak is the artifact mentioned above). As the pumping power density increases, a peak at ~3450 nm emerges, and its intensity increases dramatically with the pumping power density, as shown in Fig. 18. At 7.6 MW/cm2, this peak exhibits strong intensity and narrowed line-width of ~7 meV, showing the clear stimulated emission characteristics. While the pumping power density cannot be increased further due to the severe heat generation, the lasing at 280 K could not be further confirmed.

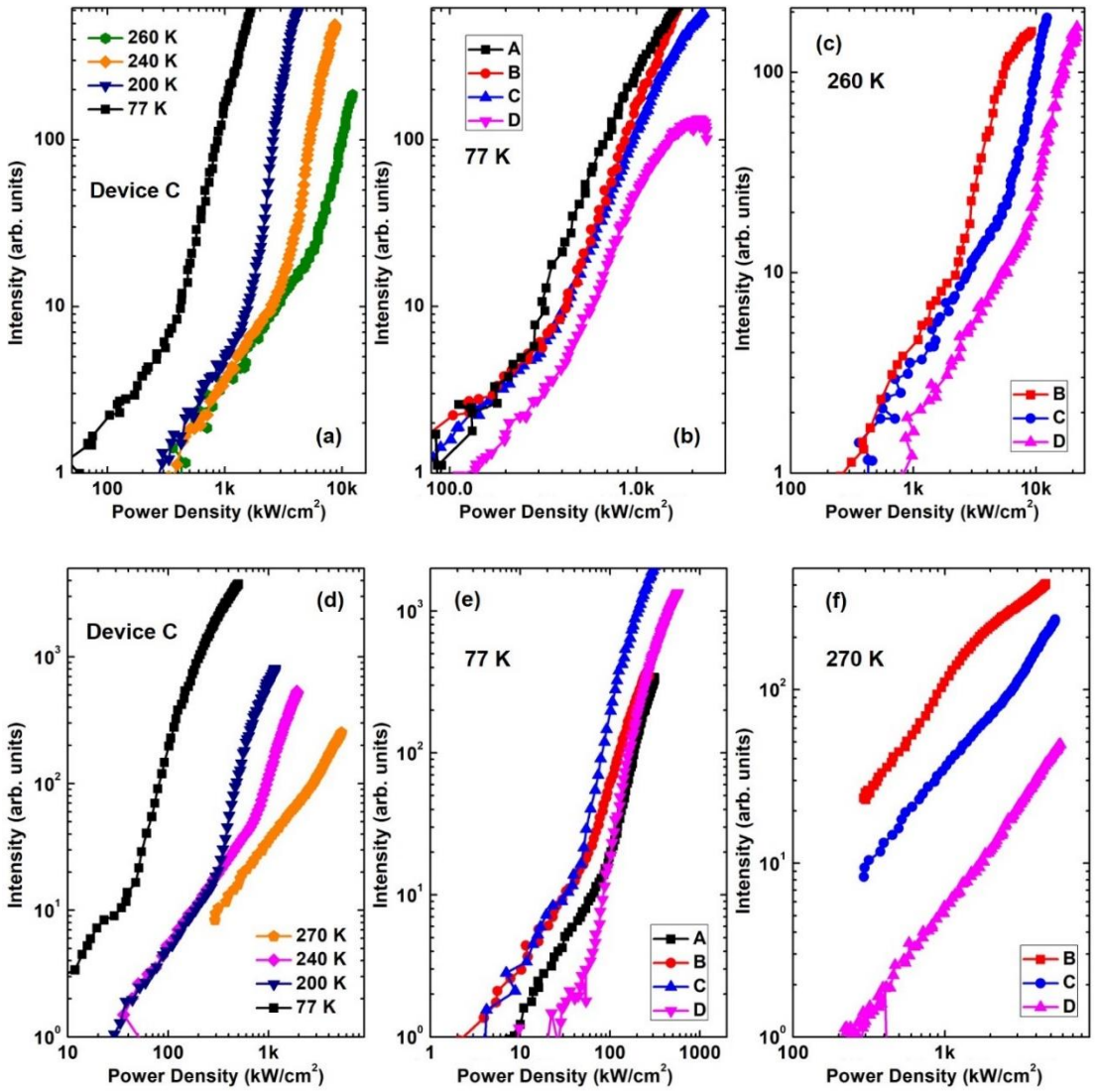

Figure 17. Top: L-L curves in log-log scale under 1064 nm laser excitation. (a) from 77 to 260 K for device C; (b) all devices at 77 K; and (c) devices B, C, and D at 260 K. Bottom: L-L curves in log-log scale under 1950 nm laser excitation. (d) from 77 to 270 K for device C; (e) all devices at 77 K; and (f) devices B, C, and D at 270 K. Reprinted with permission from [46]. Copyright 2020 American Chemical Society.

In conclusion, optically pumped GeSn lasers with ridge and planar waveguide structures were investigated. The GeSn sample was grown using a multiple-step Sn-enhanced growth recipe via industry standard CVD reactor with low-cost $SnCl_4$ and GeH_4 precursors. The maximum Sn composition of 20% was obtained. The maximum operating temperature of 270 K was achieved.

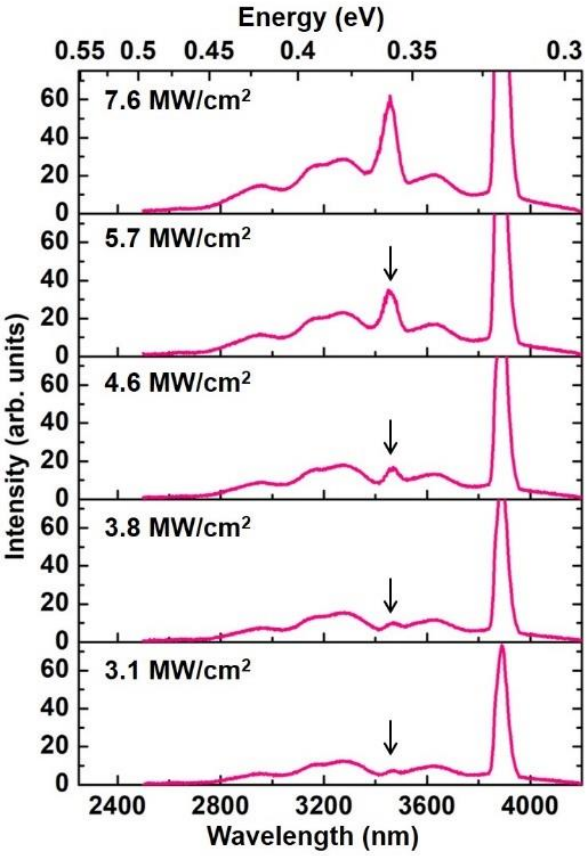

Figure 18. Power-dependent emission spectra of sample C at 280 K under 1950 nm laser. Reprinted with permission from [46]. Copyright 2020 American Chemical Society.

At 280 K, stimulated emission spectrum was observed with intensive pumping power density. Our systemic study of the four optically pumped laser devices with various ridge width reveals that the reduced side-wall surface recombination and better heat dissipation are key factors to achieve near room temperature operation. We predict that room temperature GeSn lasers can be demonstrated by: i) surface passivation (adding Ge cap layer) to further reduce the surface recombination; and ii) optimization of the ridge width to strike a balance between the heat dissipation and optical confinement. Moreover, the demonstration of planar waveguide laser structure in this study points at the great potential of GeSn lasers being advanced towards high-performance Si-based monolithically integrated mid-infrared laser sources.

2.2 GeSn gain-guided laser respected to ridge waveguide laser

The ridge waveguide laser reported in Ref. 53 and section 2.1 were fabricated using wet chemical etching. The etching forms a non-vertical sidewall. For a 5-μm-wide device, the top surface for the laser remains only ~3 μm wide. The etched sidewall has a broad area where a considerable number of carriers recombine through the surface recombination process. In such case, large carrier loss from the surface recombination deteriorates the performance of the lasers. A method that eliminates the surface recombination is desired to improve the laser performance. In this section, a GeSn ridge waveguide (index-guided) laser was compared to a gain-guided laser. The gain-guided laser avoids sidewall structure so that the surface recombination from the sidewall can be greatly eliminated.

The GeSn bulk structure was grown by using reduced pressure CVD. A 700-nm Ge was grown directly on Si substrate. A 970-nm GeSn layer was then grown. The GeSn layer resulted in two regions: a 210-nm lower region with 9% Sn composition and a 760-nm higher region with 11% Sn composition. The lower region is defective due to the relaxation of compressive strain, while the upper region has a high quality, providing the modal gain for the laser.

The ridge waveguide laser was fabricated by using a wet etch process. The etching was stopped at the lower region GeSn. The index guided laser was fabricated by using a simple gold deposition by e-beam evaporator followed by a metal liftoff process. The 5 μm wide window is exposed as the entrance window for the pumping laser. The substrate of both samples was partially removed by using the lapping. The Fabry-Perot cavity was formed by cleaving. The cavity length of ~1.2 μm prepared.

The fundamental optical TE mode profile in both lasers are calculated, shown in Fig. 19. The optical mode resides in the upper GeSn layer for both lasers. The optical confinement

factors are calculated as 70 and 72%, respectively.

The sample was set in the cryostat and pumped by a pulsed 1064 nm laser. The repetition rate and the pulse width are 45 kHz and 6 ns, respectively. The emission spectra were collected at low temperatures by using a PbS (1-3 μm) detector through a monochromator.

The temperature dependent L-L (light output vs. light input) curves are plotted in Fig. 20. At 90 K, the thresholds were measured as 817 and 600 kW/cm^2 for ridge waveguide laser and gain-guided laser, respectively. The slope efficiency values were calculated as 290 and 1400 at arbitrary units, respectively. Both lasers operated at temperatures up to 130 K. The characteristic temperature T_0 was extracted as 36 and 45 K, respectively. Figure 21 plots the

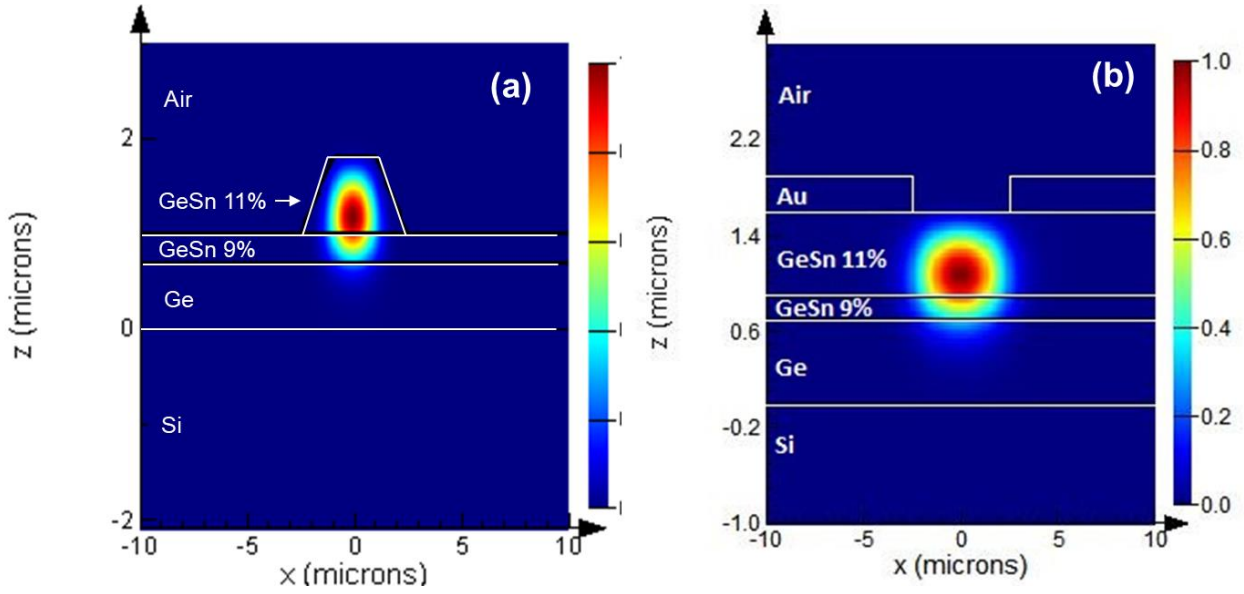

Figure 19. Fundamental TE mode profile in (a) ridge waveguide laser and (b) gain guided laser. injection power dependent emission spectra at 90 K. The peak wavelengths were measured at 2528 and 2537 nm, respectively.

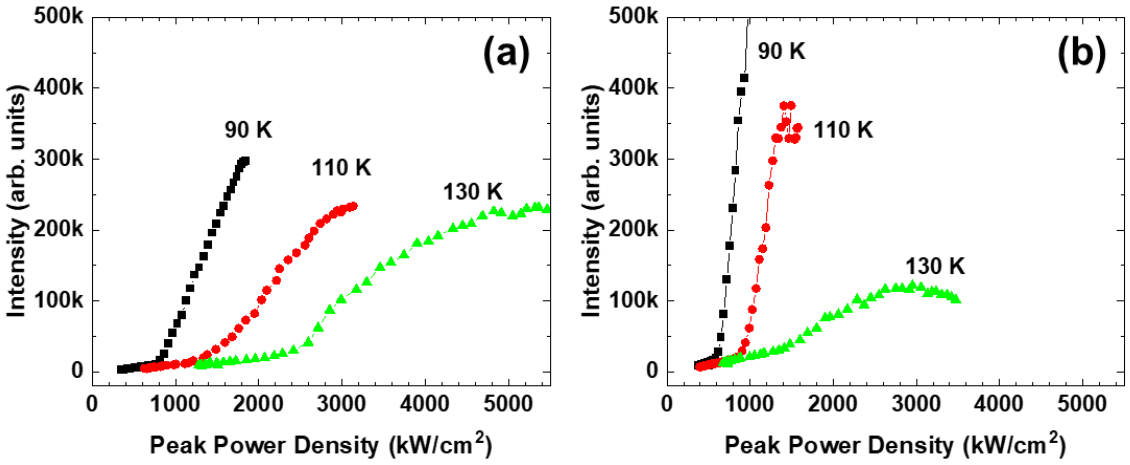

Figure 20. The L-L curve from the (a) ridge waveguide laser and (b) gain-guided laser.

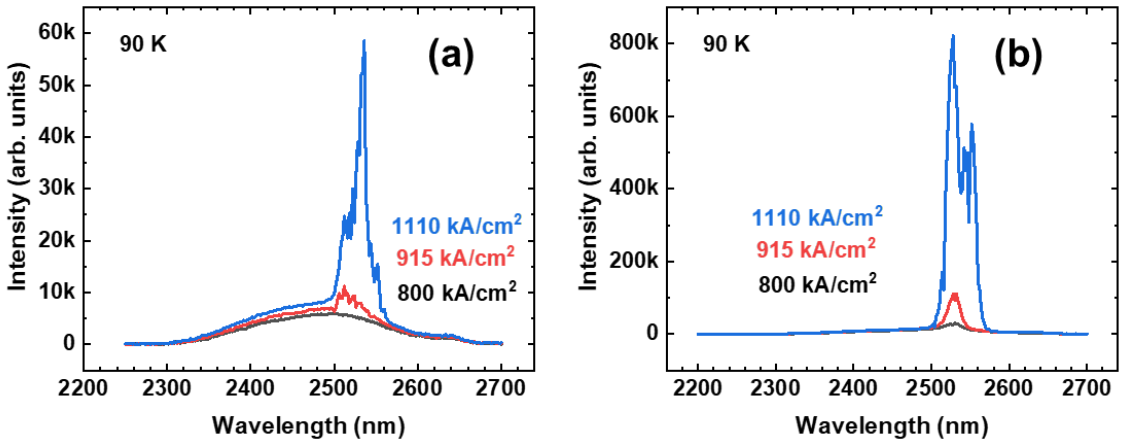

Figure 21. Injection power dependent emission spectra for (a) ridge waveguide laser and (b) gain-guided laser at 90 K.

The L-L curve shows a distinct improvement with reduced threshold and higher slope efficiency. These improvements are expected as no surface recombination in the gain-guided laser structure. Furthermore, the sidewall of the ridge waveguide structure has a lower transmittance as the incident angle is not through the normal. The absorption under the sidewall would also reduce since the GeSn layer is thinner. The laser spot side is ~20 μm, which is much larger than the device, less than 1/4 of the light energy contributes to the carriers, and the rest of the energy will transfer to thermal energy that heats the device. In the gain-guided layer, the Au-

coated layer can reflect the light away from the sample and only pass the light through where the window opened. This feature helps to eliminate the unnecessary absorption at the non-gain area and adds a thermal dissipation channel via the top surface to reduce the local temperature.

In sum, the GeSn optically pumped lasers were characterized using a ridge waveguide structure and a gain-guided structure. The gain-guided structure offered a lower threshold thanks to the elimination of the surface recombination as well as the reflection of the unnecessary light.

2.3 Microdisk laser compared to ridge waveguide lasers

The high material structure was fabricated into micro-disk lasers and tested at Univ. Grenoble Alpes, CEA [40]. The microdisk has a thickness of 1 μm and diameter of 10 μm. The microdisk laser was pumped by using a 1064 nm laser and showed a threshold of 108 kW/cm^2 at 15 K. The T_{max} of the microdisk was measured as 250 K. The microdisk laser showed a lower threshold compared to the ridge waveguide F-P laser. This was benefited from the higher Q value in the micro-cavity compared to the F-P cavity. However, the microdisk has a 10 K lower T_{max} than the F-P cavity. This is likely due to the limited thermal dissipation as only small pillar remaining as the dissipation channel. The F-P lasers, especially for broad ridge, dissipate more heat than the microdisk lasers since the active region directly contacts to the substrate. A review of laser performance of optically pumped lasers is summarized in Table 3.

Figure 22 summarizes the Sn composition, material thickness, and maximum lasing temperature for the F-P lasers fabricated at University of Arkansas. All sample growth recipe adopts the SRE technique. The larger GeSn thickness by using the same growth recipe leading to the relaxation of the epi layer, which further enables a higher Sn incorporation. The higher Sn composition GeSn has a direct bandgap and a lower Γ valley minimum energy than L valley.

The relaxation of the compressive in-plane strain could keep the sufficient energy difference between the L and Γ valley. These resulted in a higher carrier injection efficiency and a higher material gain for the laser device, leading to lasing at elevated temperatures.

Table 3. A brief review of GeSn laser development. Reprinted with permission from [40].

Layer Structure	Optical Cavity	Maximum Sn Composition	Typical Threshold	Operation Wavelength	Operation Temperature
HS	F-P	12.6%	325 kW/cm^2 @ 20 K	2.3 μm	90 K [32]
HS	F-P	10.9%	68 kW/cm^2 @ 10 K	2.5 μm	110 K [53]
HS	Micro-disk	12.5%	220 kW/cm^2 @ 50 K	2.5 μm	130 K [36]
HS	Micro-disk	16.1%	377 kW/cm^2 @ 25 K	3.1 μm	180 K [34]
HS	F-P	7.3% - 17.5%	117-300 kW/cm^2 @ 77 K	2.0 - 3.0 μm	180 K [35]
HS	Micro-disk	14.5%	300 kW/cm^2 @ 20 K 421 kW/cm^2 @ 20 K*	2.6 μm	100 K [39] 120 K* [39]
MQW	Micro-disk	13.3%	35 kW/cm^2 @ 20 K 45 kW/cm^2 @ 20 K*	2.5 μm	100 K [39] 120 K* [39]
MQW	F-P	13.8% - 14.4%	25 kW/cm^2 @ 10 K**	2.6 μm	90 K** [62]
HS	F-P	22.3%	203 kW/cm^2 @ 77 K 137 kW/cm^2 @ 77 K**	3.0 μm	150 K [24] 180 K** [37]
HS	Micro-disk	16.0%	134 kW/cm^2 @ 15 K	2.9 - 3.2 μm	230 K [40]
HS	F-P	20.0%	330 kW/cm^2 @ 77 K 47 kW/cm^2 @ 77 K**	2.9 - 3.4 μm 2.8 - 3.5 μm**	260 K [46] 270 K** [46]

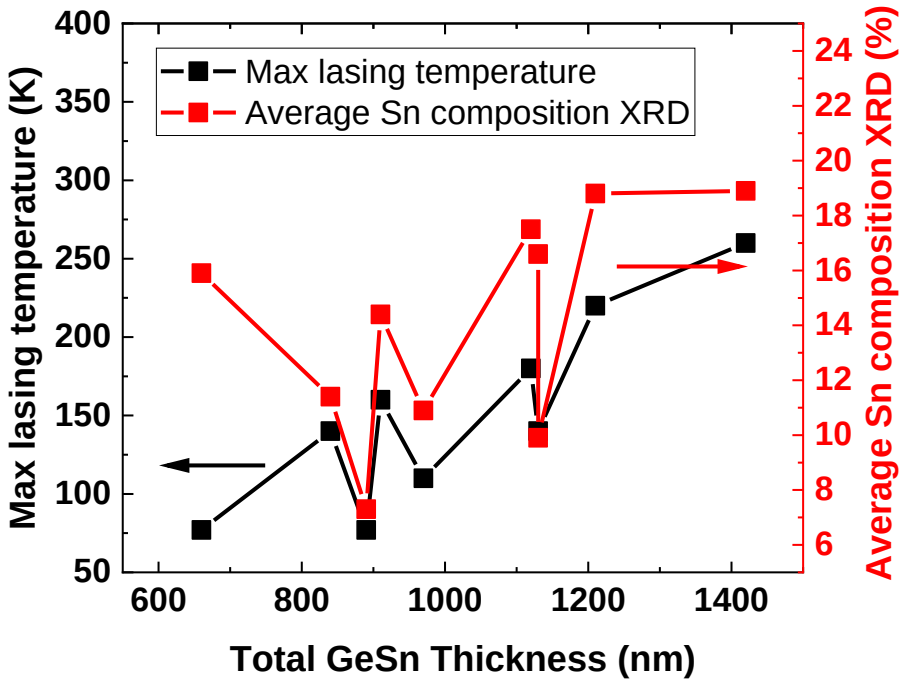

Figure 22. Relation between Sn composition, total thickness of GeSn, and T_{max} for ridge waveguide lasers.

Chapter 3: SiGeSn/GeSn MQW lasers

Historically, QW structure significantly reduced the semiconductor laser threshold, which ultimately enable the room temperature continuous wave operation [24,29]. The reduction of threshold is the advantage of the quantum confinement provided by the QW structure. In the QW structure, the elections and holes reside at the quantized energy levels and can reach to threshold condition with less carriers comparing to the double heterostructure. For laser using direct bandgap GeSn as active region, it is highly desired to investigate the optical property of the GeSn QW structures to achieve the reduction of threshold. In this section, the investigation starts with the design considerations of the QW structure, following by the demonstration of 4QW lasers, the device structures for the optically pumped GeSn MQW lasers are also discussed for future improvement.

In QW structure, the energy levels are quantized at discrete energy levels. In Fig. 23 the density of state is a stair profile in comparison with the bulk material. The major benefit for this

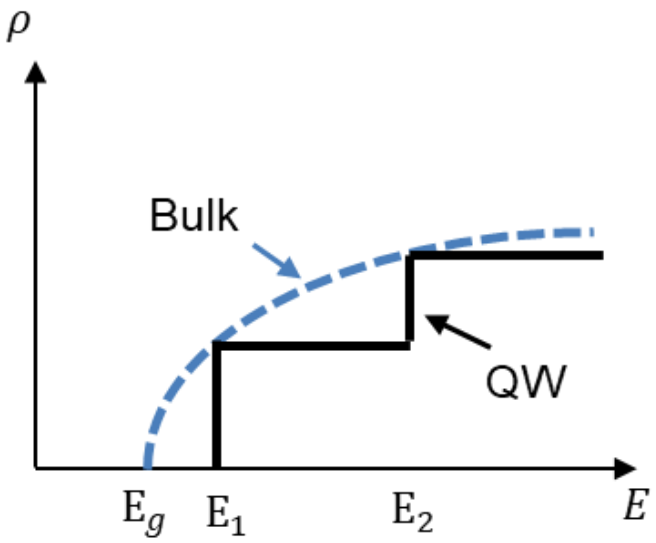

Figure 23. Density of state for the bulk and QW structure.

step profile is that the carriers populate directly at the discretized energy levels without the need of filling other energy states as in the bulk material. Therefore, less carriers are required to achieve the carrier population level in the designed energy state. The light emission through the designed transition states is more effective at designed energy transitions.

In MQW structure for light emission, the individual wells independently contribute to the total emission. Compared to the single QW, whose density of state is limited for small current injection level, the MQW structure multiplies the density of states with the number of wells. Consequently, MQW increase the saturation limit of the carrier density within the active region, maintaining the transition rate under large carrier injection. In a laser design, the material gain is one of the most important parameters. The material gain for MQW is directly proportional to the number of wells. Therefore, increasing number of wells is a powerful method to achieve the desired material gain.

3.1 Quantum well design and optical property

3.1.1 GeSn QW structure: barrier selections

So far, there are three phases of study on the GeSn QW in terms of barrier material using Ge, GeSn, and SiGeSn. The pros and cons for these QW structures for light emission are discussed here.

The GeSn QW using Ge barrier was the first structure that experimentally realized in a microdisk resonator on Si [30]. The Ge is the most accessible barrier material while offer a large potential barrier in the conduction band. As stated in the reference, the L valley in conduction band becomes lower than the Γ valley due to the high level of compressive strain. This band condition makes the well an indirect bandgap material, which is limited for light emission. The

lattice mismatch between Ge and GeSn further limit the potential increase of Sn incorporation, which is necessary to achieve the direct bandgap. Therefore, a method to reduce the huge compressive strain in the GeSn well layer is a key direction for light emission using GeSn QW structure.

Studies using GeSn barriers showed a promising in making the bandgap of GeSn well to be direct [43,54]. The bulk GeSn buffer layer could not only reduce the lattice mismatch between well and barrier layers, but also serve as a barrier layer to form the quantum structure. As the consequence, GeSn with higher Sn composition in well region is likely to be achieved during the non-equilibrium growth process using CVD. With less compressive strain and higher Sn composition, the direct bandgap GeSn well can be achieved. The direct bandgap emission from GeSn QW was demonstrated at cryogenic temperatures [43]. It is also noted that the barrier height is rather limited (<50 meV) with the combination of GeSn layers using low and high Sn composition. Such barrier height is rather limited to hold sufficient carriers within the QW region, especially at elevated temperatures. In addition, if the GeSn barriers are selected, the direct method to increase the barrier height is to reduce the Sn composition, which would deteriorate the efforts to reduce the lattice mismatch and increase the well Sn composition incorporation. This would limit the QW light emission at cryogenic temperatures. For elevated temperatures towards 300 K, the carriers could easily gain the thermal energy to escape from the quantum confinement. A higher barrier height would thusly preferred.

Barrier material using SiGeSn provides the advantages both from Ge and GeSn barriers: (1) the tunable composition makes it possible to reduce the lattice mismatch between well and barriers; (2) the larger bandgap providing high barrier height in conduction band; and (3) potentially growing high Sn composition for direct bandgap emission. Thanks to the

intermediate Ge and GeSn buffer, the compressive strain in the well region is greatly eased so that high Sn composition could be achieved. In this dissertation, Sn composition as high as 15% was achieved in GeSn using SiGeSn barrier. The high Sn composition leaves separation between L and Γ valley so that the negative impact from the compressive strain can be balanced. Therefore, a direct bandgap GeSn QW with sufficiently high barrier (~200 meV) could be realized. In this dissertation, the SiGeSn composition is fixed at nominal recipe with 3% and 8% for the Si and Sn composition, respectively. Further exploration of Si and Sn composition growth recipe remain highly interested in future development.

3.1.2 Design and characterization of strain-balanced MQW

In this section, the design and characterization of MQW structures are presented. Figure 24 describes the structure used in this section. The epitaxial structure consists of two major sections: the Ge and GeSn buffer and the SiGeSn/GeSn MQW region. The epitaxial structures were grown on the Si wafer. The Ge buffer is grown with a thickness of 700 nm. A spontaneous relaxed GeSn buffer is grown with a starting Sn composition at 8%, the ending Sn composition is designed at 11%. The thickness of the GeSn buffer is designed at 800 nm. The bottom SiGeSn barrier has a thickness of 50 nm, the GeSn wells and SiGeSn barriers are repeatedly grown with thickness of 20 and 15 nm, respectively. Three samples were grown with the number of wells as four, six, and ten.

The thickness of the sample is designed to be strain-balanced, following the relation: $t_{barrier} \times \varepsilon_{barrier} + t_{well} \times \varepsilon_{well} = 0$, where t and ε are the thickness and strain for the layer. This condition makes the growth condition repeating at the end of each period. As a result, the multiple periods can be grown with the same starting strain condition, which promises the same

growth result (thickness and composition) for each period.

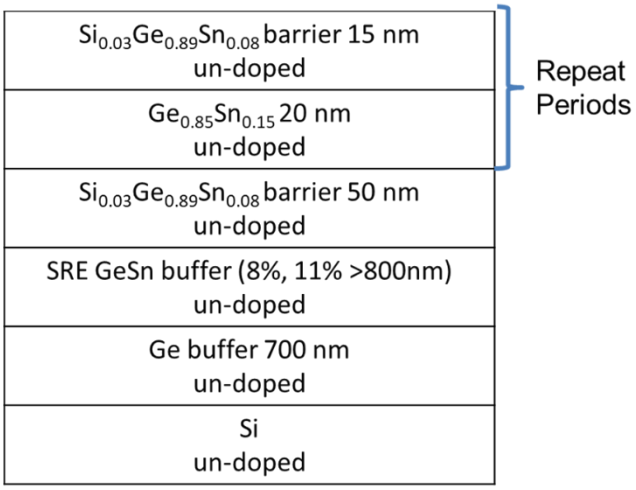

Figure 24. The MQW layer structure.

The temperature dependent PL spectra were characterized. The 100 mW 532 nm CW laser was used as the pumping source to inject carriers. Figure 25(a) showed the PL spectra from 4QW sample at temperatures from 10 to 300 K. The spectra present the typical emission spectra from MQW structure. The emission peak intensity at temperatures below 100 K are significantly higher than intensity at higher temperatures. The emission peak shifts towards longer wavelength at high temperatures, showing reduction of bandgap energy.

The 4QW sample has emission peak intensity ~40, compared to 10QW has emission intensity at ~160. The significant increase of the peak intensity implies the improved emission efficiency from the MQW structure. In 4QW sample, there is a peak at 2200 nm indicating the carrier escaped from the MQW recombines at GeSn buffer layer, which has a wider bandgap transition. By increasing well number, more carriers allowed to populate within the MQW region, contributing to the radiative recombination through QW. Therefore, the peak intensity is higher in 6QW sample.

For 10QW sample, the emission peak intensity is further increased, indicating more carriers are involved in the radiative recombination. The emission efficiency is further improved. On the other hand, the emission peak wavelength at 10 K has a red shift compared to 50 K. This shift implies an internal heating process within the 10QW, where heat cannot be dissipated well causing bandgap shrinkage. With more repeating layers in MQW, the thermal conductivity becomes limited due to the interfaces. The heat generated could not be dissipated property, causing the red shift, especially at 10 K, where the temperature change is quite sensitive.

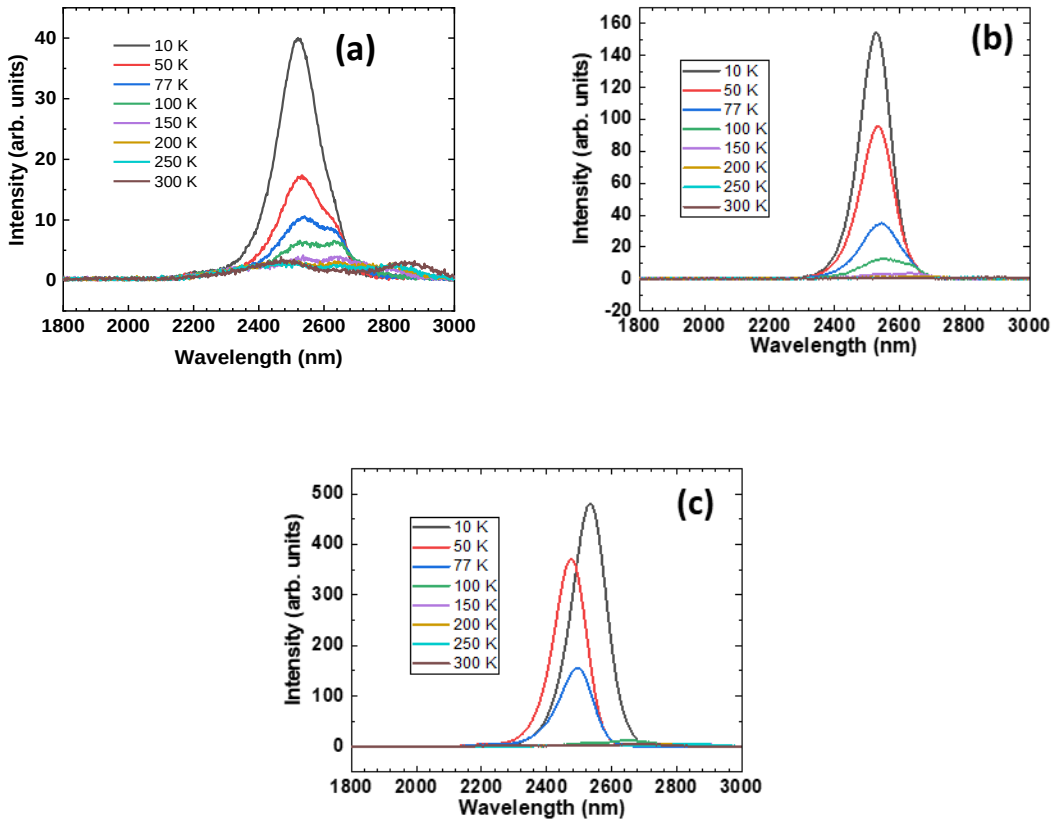

Figure 25. The PL for (a)4QW, (b)6QW, and (c)10QW.

3.1.3 Design and characterization of separate confinement heterostructure QW structure

The separate confinement heterostructure adopts the QW structure with additional carrier blocking layer to confine the carriers from escaping the QW region. This altertatively solves the low barrier issue for GeSn barrier QW. The carriers escaped from the QW will be held within the QW region by the outer barrier. The carrier confinement in this design effectively increased the carrier density contributing to the light emission, which yield to a higher emission efficiency.

Figure 26(a) shows the desgined SCH SQW structure using GeSn and SiGeSn barriers. The well remains the Sn composition at 15%. The SQW barrier adopts GeSn with Sn composition at 11%. And the SCH barrier takes SiGeSn with Si and Sn composition at 3 and 8% respectively. The structure was grown on a Ge buffer followed by a thick and relaxed GeSn buffer. The GeSn buffer is grown using the SRE technique so the Sn compsition reaches 11% with the upper surface mostly relaxed.

The relaxation of the GeSn buffer ensures the SQW to be direct bandgap, as shown in Fig. 26(b), where the Γ band in the QW is much lower than the indirect L band. In the conduction band, the QW barrier height is small ~33 meV between the barrier and the well. The SiGeSn barriers add the barrier height wih extra 200 meV. This extra energy barrier provides sufficient confinement to electrons.

The temperature dependent PL was measured and shown in Fig. 26. The 10 K spectrum shows a single emission peak at 2400 nm, showing the emission from the SQW region. No emission peak was identified at ~2160 nm, indicating the sufficient carrier confinement within the SCH SQW structure. In addition, the peak intensity is much about five times stronger than the SQW sample (SiGeSn/GeSn/SiGeSn), showing the improvement on the quantum efficiency with the SCH structure. More carriers paticipat in the radiative recombination in the QW region.

The design is aimed at developing into SCH MQW laser structure, eventually for the next generation GeSn MQW electrically injected laser. The MQW structure could be used to increase the material gain at high injection. The SCH design ensures the electrons can be sufficiently confined within the MQW active region. Furthermore, the combination of GeSn and SiGeSn barriers could also serve the purpose of adjusting the optical mode in the waveguide, which add another degree of freedom for the laser device design.

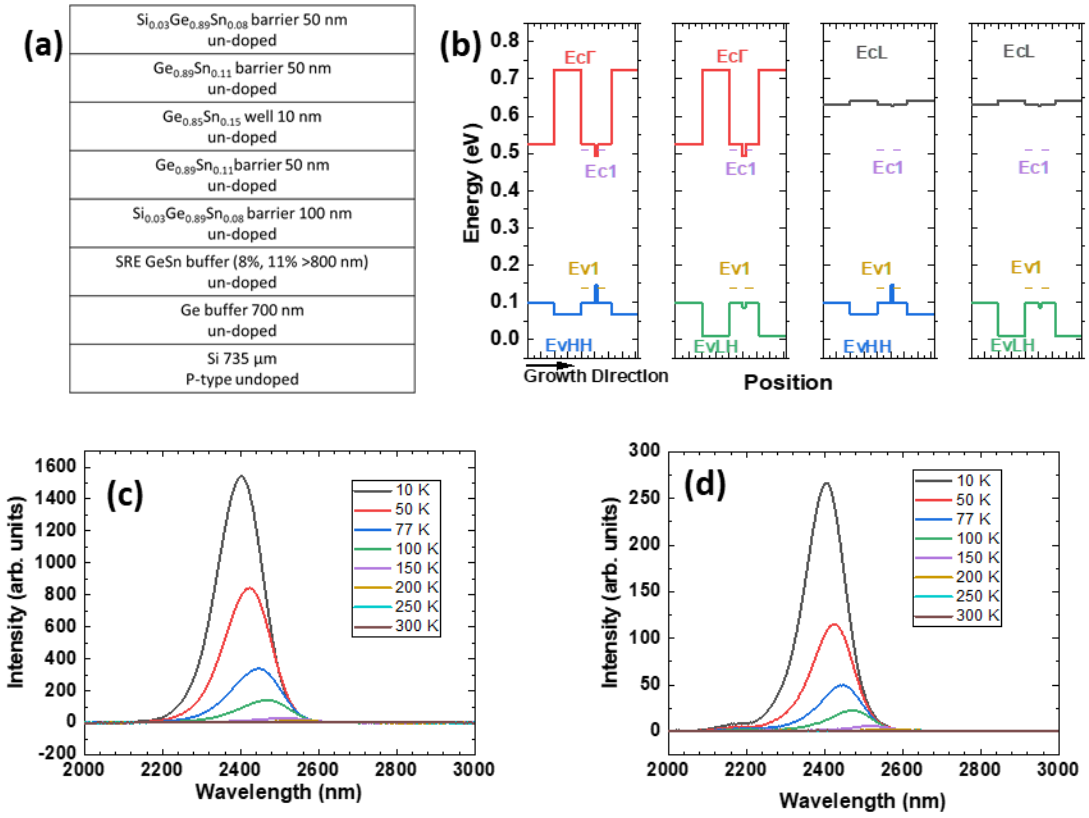

Figure 26. (a) structure of the SCH SQW structure, (b) calculated four band edges and the first quantized energy in Γ (Ec1) and HH (Ev1), and temperature dependent PL spectra for (c) SCH SQW and (d) SiGeSn/GeSn/SiGeSn SQW.

3.2 MQW laser

It is generally acknowledged that the QW structures could be applied to the laser

structures to improve their device performance which eventually may lead to room temperature operation [24,29]. GeSn based MQW configurations have been grown and characterized, including Ge/GeSn, GeSn/GeSn, SiGeSn/GeSn, etc. [33,43,54-57]. Our previous study indicated that by appropriately selecting the Si and Sn compositions, using GeSn as buffer (with Sn composition lower than that in GeSn well) on Ge virtual substrate (VS) and SiGeSn as barrier could achieve direct bandgap well with type-I band alignment, as well as sufficient carrier confinement [43,54,57]. Applying MQW to GeSn laser has been previously proposed and the structures have been grown and characterized [39,58-60]. However, a detailed experimental study of the MQW GeSn laser has not been reported so far, which is expected to set a baseline for further device design optimization.

In this work, two MQW samples (annotated as A and B) with 4-well structures were investigated. Optically pumped lasing was achieved for both samples. The sample with the higher Sn composition and the total well layer thickness (larger gain volume) exhibited lower lasing threshold and higher maximum operating temperature. The distinct results could provide effective guidance for future QW laser design especially the selection of action region structure.

The MQW samples A and B studied in this work were grown using an industry standard ASM Epsilon® 2000-Plus RPCVD system. Low-cost commercially available SiH_4, GeH_4, and $SnCl_4$ were used as Si, Ge, and Sn precursors, respectively. The Ge buffer layer (600 and 1000 nm-thick for samples A and B) was grown on Si substrate by a two-step growth method [61]. For each sample, a relaxed GeSn buffer was grown prior to QW growth to reduce the strain of the MQW layer-stack. The barrier/well layer-stacks were then grown pseudomorphically to the relaxed GeSn buffer. After the growth, high-resolution X-ray diffraction (HRXRD) 2θ-ω scan and RSM were employed to identify Si and Sn compositions and the degree of strain of each

layer. Cross-sectional TEM images were utilized to determine the layer thickness and examine the material quality. Atom probe tomography (APT) and SIMS were performed to cross-check the Si and Sn compositions and the layer thickness. The detailed information is included in supplementary.

The Sn compositions in well layers were measured as 13.8% and 14.4% for sample A and sample B, respectively. The wells have consistent Sn composition and thickness, confirmed by APT result (see supplementary). The $Ge_{0.912}Sn_{0.088}$ buffer in sample B used with its correspondingly larger starting lattice constant allows for higher levels of Sn incorporation in the GeSn wells. Compared to sample A, sample B has thicker GeSn wells and SiGeSn barriers, as well as higher corresponding Sn compositions in each well. Figure 27 summarizes the layer information for sample A and B.

(a)		(b)	
$Si_{0.050}Ge_{0.887}Sn_{0.063}$	72 nm	$Si_{0.033}Ge_{0.887}Sn_{0.080}$	95 nm
$Ge_{0.862}Sn_{0.138}$ 1st QW	22 nm	$Ge_{0.856}Sn_{0.144}$ 1st QW	30 nm
$Si_{0.050}Ge_{0.887}Sn_{0.063}$	71 nm	$Si_{0.033}Ge_{0.887}Sn_{0.080}$	99 nm
$Ge_{0.862}Sn_{0.138}$ 2nd QW	22 nm	$Ge_{0.856}Sn_{0.144}$ 2nd QW	31 nm
$Si_{0.050}Ge_{0.887}Sn_{0.063}$	70 nm	$Si_{0.033}Ge_{0.887}Sn_{0.080}$	99 nm
$Ge_{0.862}Sn_{0.138}$ 3rd QW	24 nm	$Ge_{0.856}Sn_{0.144}$ 3rd QW	31 nm
$Si_{0.050}Ge_{0.887}Sn_{0.063}$	74 nm	$Si_{0.033}Ge_{0.887}Sn_{0.080}$	99 nm
$Ge_{0.862}Sn_{0.138}$ 4th QW	22 nm	$Ge_{0.856}Sn_{0.144}$ 4th QW	31 nm
$Si_{0.050}Ge_{0.887}Sn_{0.063}$	85 nm	$Si_{0.033}Ge_{0.887}Sn_{0.080}$	105 nm
$Ge_{0.916}Sn_{0.084}$ buffer	600 nm	$Ge_{0.912}Sn_{0.088}$ buffer	700 nm

Figure 27. Schematic diagrams of (a) sample A and (b) sample B showing the extracted Si and Sn compositions and each layer thickness. Reproduced from [62], with the permission of AIP Publishing.

The high-resolution X-ray diffraction (HRXRD) RSM was performed to examine the Sn

compositions and strain for each layer. Figure 28 (a) and (b) show the RSM contour plots for samples A and B, respectively. The well and barrier layers were psuedomorphically grown with respect to GeSn buffer for both samples. The Sn composition for the GeSn well and buffer and in-plane strain for each layer are summarized in Table 4.

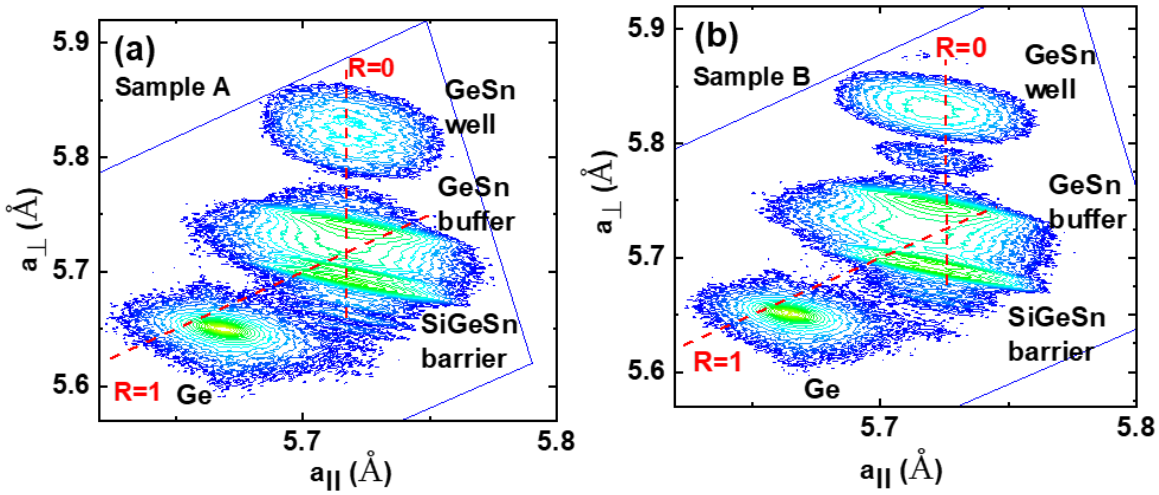

Figure 28. HRXRD RSM contour plot for (a) sample A and (b) sample B. Dash lines are the eye guidance of relaxation for R = 1 and R = 0. Reproduced from [62], with the permission of AIP Publishing.

Table 4. Sn composition and in plane strain extracted from XRD RSM. Reproduced from [62], with the permission of AIP Publishing.

	Sample A			Sample B		
	GeSn well	SiGeSn barrier	GeSn buffer	GeSn well	SiGeSn barrier	GeSn buffer
Sn composition (%)	13.8	-	8.4	14.4	-	8.8
In-plane strain (%)	-1.05	0.18	-0.22	-1.11	0.31	-0.12

* Negative values indicate the compressive strain.

Figure 29 (a) shows the SIMS profile overlaid with TEM image of sample A. Along the growth direction, the Sn compositions of GeSn wells were obtained as 10.0%, 11.0%, 12.3% and 13.0%, respectively. The variation of compositions is mainly due to the depth broadening effect

of SIMS measurement: as the measured depth increases (deeper into the sample), the shape of the SIMS sputter hole tends to taper (become v-shaped). The ion beam increasingly interacts with the sidewalls of the sputter hole which interferes with the actual signal from the bottom of the sputtered hole, results in the different readout values of Si and Sn compositions. Note that since the SIMS provides the average composition value across a monolayer, the measured Si and Sn compositions in barriers were not affected by depth broadening effect due to the relative

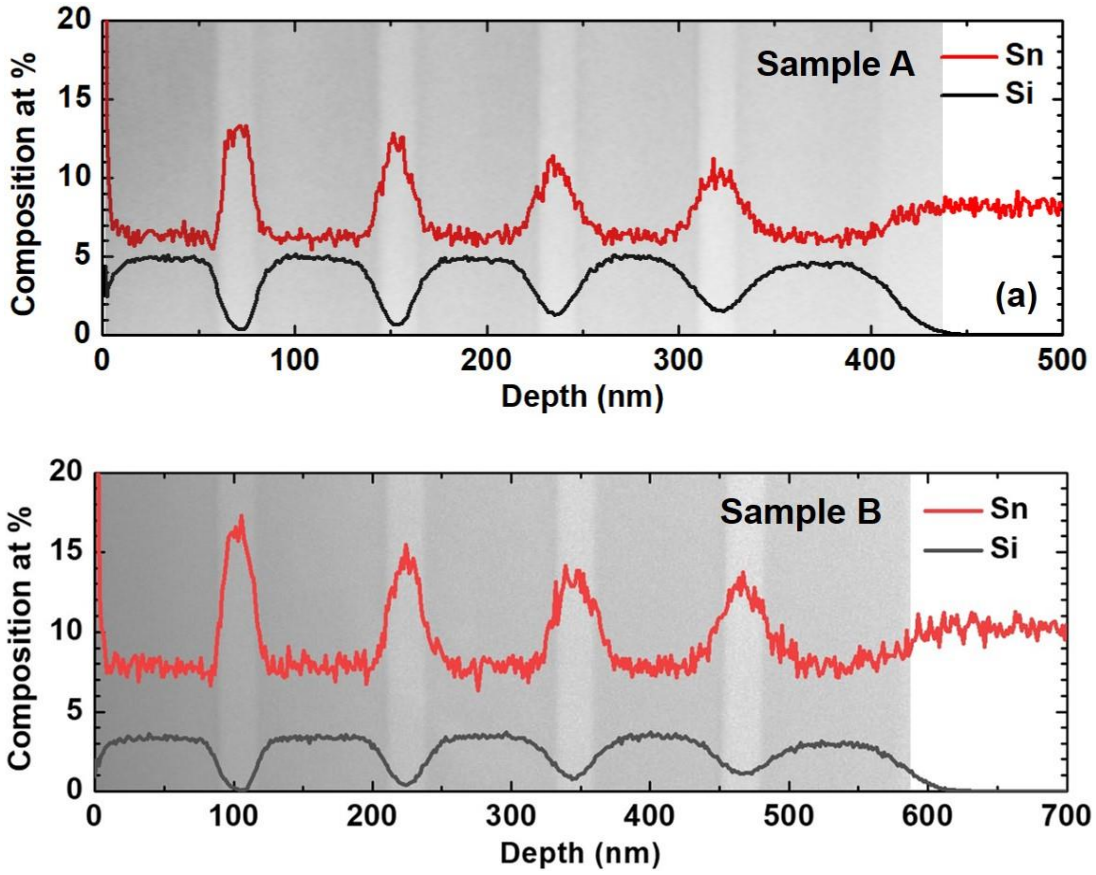

Figure 29. SIMS profiles and TEM images for (a) sample A and (b) sample B showing the measured Si and Sn compositions and each layer thickness. Reproduced from [62], with the permission of AIP Publishing.

thicker layer, i.e., the slight inaccurate SIMS readout only affects the thin layer such as QW. The

Si and Sn compositions in the SiGeSn barrier layer were determined as 5% and 6.3% respectively. Based on the TEM image, each well/barrier layer can be clearly resolved and features low defect density. There are almost no threading dislocations propagating across the QW, indicating the high material quality. The low defect density is mainly due to the formation of threading dislocation loops in the GeSn buffer layer, which prevents the defects from being propagated to the QW region. The measured thickness of each well from TEM image agrees well with the full width at half maximum (FWHM) of SIMS peak, as shown in Fig. 29(a).

Atomic probe tomography (APT) measurement was performed to cross-check the Si and Sn composition in the well and barrier. Figure 30 shows the APT measurement result of sample

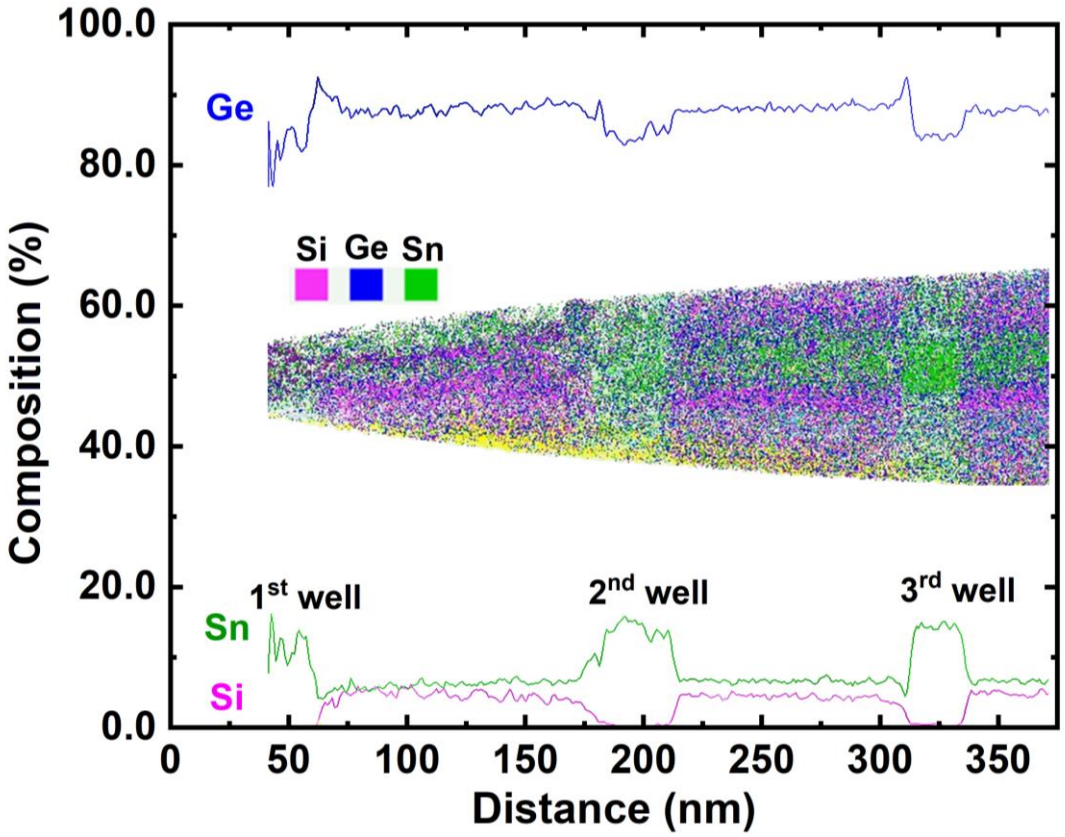

Figure 30. 1D APT composition scan of Si, Ge, Sn compositions. Inset: An atom map of Sample B reconstructed from the 3D APT. Reproduced from [62], with the permission of AIP Publishing.

B. From the sample surface, the Sn composition in 1st, 2nd, and 3rd well was obtained as 14.4%, well. The Si and Sn compositions in SiGeSn barrier were measured as 3.3% and 8.0%, respectively. The abrupt transitions between the barrier and well compositions indicate the high-quality material structure. The asymmetric increase in the Ge compositional profile at the well/barrier interface in Figure 30 is a reconstruction artefact from the differences in the field evaporation strengths between the two materials. Although the 4th well was not measured because of the limited ability to sample through the entire tip, it is reasonable to believe that the Sn composition in 4th well should be identical to other three wells since the growth condition was kept the same.

The band structures of samples A and B are calculated at 300 K, as shown in Fig. 31, using the data from material characterizations. For sample A, the wells feature direct bandgap with the energy difference between L and Γ of 42 meV. The optical transition in the well is 0.450 eV (2753 nm). The barrier heights in conduction band (CB) and valence band (VB) are 175 and 113 meV, respectively. For sample B, the direct bandgap wells show the energy

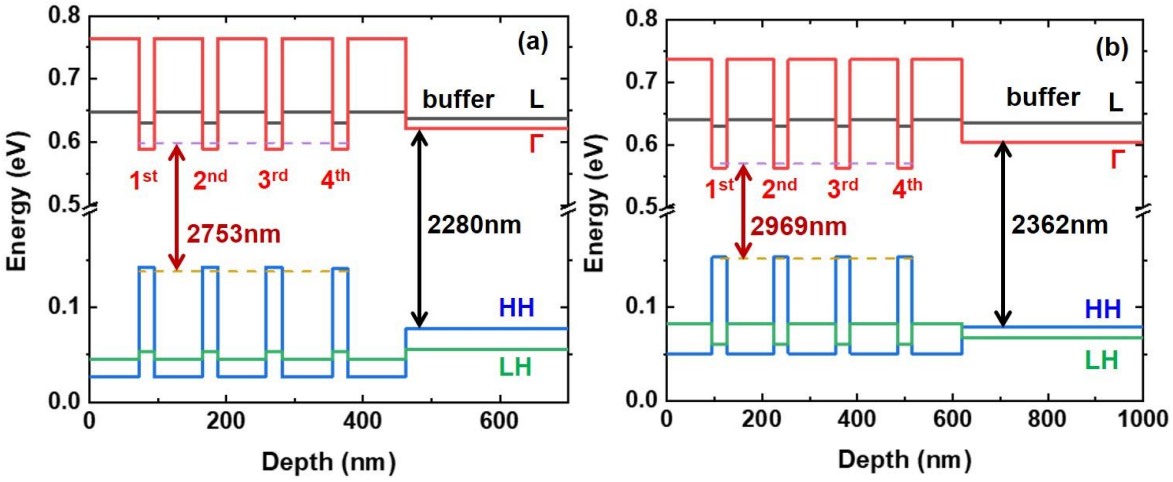

Figure 31. Calculated band structures of (a) sample A, and (b) sample B. Reproduced from [62], with the permission of AIP Publishing.

difference between L and Γ of 67 meV. The optical transition in the well is 0.418 eV (2969 nm). The barrier heights in conduction band (CB) and valence band (VB) are 174 and 102 meV, respectively. The emission wavelengths of GeSn buffer are 2280 nm and 2362 nm for samples A and B, respectively, which are much shorter than optical transitions in the well.

The PL measurements were performed using a standard off-axis configuration with a lock-in technique (optically chopped at 377 Hz). A continuous wave (CW) laser emitting at 532 nm wavelength was used as an excitation source. The laser beam was focused down to a 100-μm-diam spot and the power was measured to be 100 mW. The PL emission was collected by a spectrometer and then sent to an InSb detector with cut-off at 5.0 μm.

The temperature-dependent PL spectra are shown in Fig. 32(a). For each sample, as the temperature decreases from 300 K to 10 K, the PL intensity dramatically increases, showing the clear signature of the direct bandgap material. The observed PL peak features clear blue-shift at lower temperature, which is expected due to the increase of the bandgap. Note that since the penetration depth of the 532-nm excitation laser beam is less than 100 nm in GeSn/SiGeSn, the major light absorption can occur only in the top layers including the top SiGeSn barrier and 1st GeSn well, and therefore the major emissions are from the 1st GeSn wells. Compared with sample A, sample B exhibits higher PL peak intensity and longer emission wavelength. This is attributed to enhanced direct bandgap radiative recombination due to a higher Sn composition in sample B. It worth noting that for each sample, at each temperature only a single peak (emission from GeSn well) was observed and no emission feature from barrier can be found in the PL spectrum. This indicated the sufficient carrier confinement at both CB and VB.

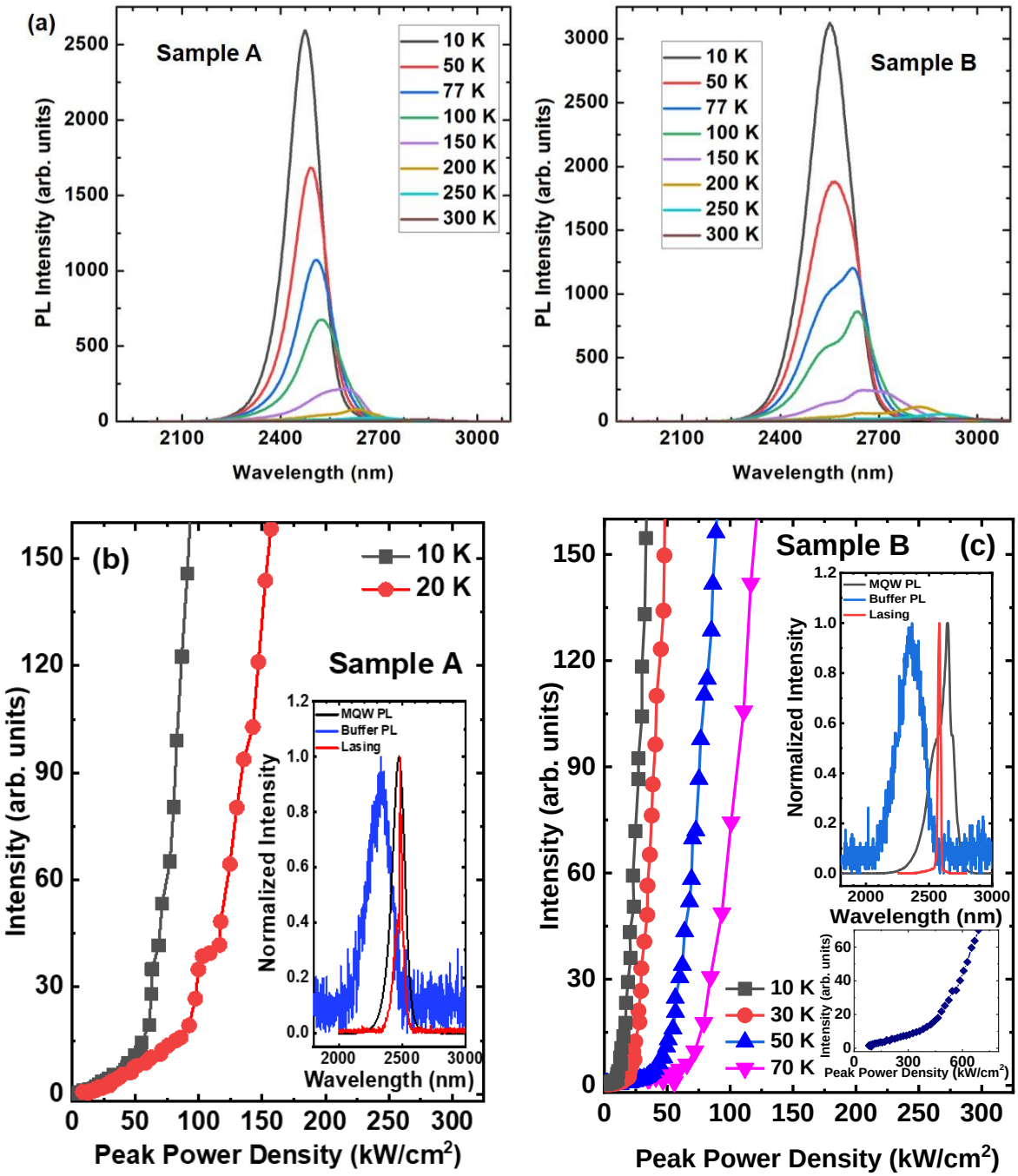

Figure 32. (a) Temperature-dependent PL spectra for samples A and B; (b) L-L curves of sample A. Inset: Lasing, PL spectra of MQW, and GeSn buffer at 10 K; (c) L-L curves of sample B. Inset: top: Lasing, PL spectra of MQW, and GeSn buffer at 77 K; bottom: L-L curve at 90 K. Reproduced from [62], with the permission of AIP Publishing.

Ridge-waveguide-based edge-emitting lasers were fabricated by standard lithography and wet etching processes. The etching depth was selected as 800 nm to provide a sufficient mode

confinement. After etching, the samples were lapped down to ~70 μm thickness and then cleaved to form the cavity. The detailed fabrication procedure was reported in Ref [35].

The optical pumping characterization was performed using a pulsed laser operating at 1950 nm with 10 kHz repetition rate and 20 ns pulse width. The laser beam was collimated to a narrow stripe (~20 μm width and 0.3 cm length) via a cylindrical lens to pump the GeSn waveguide structure. The device was first mounted on a Si chip carrier and then placed into a continuous flow cryostat for low temperature measurement. The emission from the facet was collected by a spectrometer and then sent to an InSb detector. Note that the penetration depth of 1950-nm laser beam is deeper than 1000 nm so that all QWs are involved in the light absorption.

Figure 32(b) shows the laser-output versus pumping-laser-input (L-L) curves for sample A (2300 μm-long and 20 μm-wide device). The 10 to 20 K curves show a clear threshold characteristic, with the corresponding thresholds from 55 to 110 kW/cm2, respectively. Beyond 20 K, the threshold characteristic disappears, and the spontaneous light emission is dominant. The lasing, PL spectra of MQW and GeSn buffer at 10 K are shown in the Fig. 32(b) inset. Compared to the line-width of MQW PL peak, the dramatically reduced line-width of lasing peak further confirms the lasing characteristic. It worth pointing that unlike the MQW PL emission that only the 1st GeSn well is involved in the light emission, under 1950-nm pumping all four GeSn QWs contribute to the lasing emission. The laser operating wavelength was determined as 2490 nm at 10 K. Moreover, the peak of GeSn buffer PL locates at 2200 nm, which is much shorter than MWQ PL peak and lasing peak, confirming that the lasing emission comes from the MQW (see supplementary).

Figure 32(c) shows the laser-output versus pumping-laser-input (L-L) curves for sample B (1350 μm-long and 20 μm-wide device). The threshold characteristic was observed up to 90 K

(see bottom inset). As the temperature increases from 10 to 90 K, the lasing thresholds were extracted from 25 to 480 kW/cm^2. The threshold of 62 kW/cm^2 at 70 K is lower than that of the previously reported GeSn heterostructure laser under the same pumping condition (137 kW/cm^2) [37]. The characteristic temperature was calculated as 53 K (from 10 to 70 K), which is a bit lower than that in Ref. 37 (65 K). The lasing wavelengths (transition between first electron and hole quantized energy levels) match well with the calculation, confirming the laser emissions are from the QW region. Figure 32(c) top inset shows the spectrum comparison among GeSn buffer PL, MQW PL, and lasing at 77 K. The lasing peak shows a blue-shift of 70 nm relative to its PL peak. This blue-shift can be interpreted as the typical band filling effect, which has also been observed in the previously reported GeSn lasers [35,43]. The peak of buffer PL is more than 300 nm away from those of lasing and MQW PL, indicating the lasing originally from MQW.

The temperature-dependent lasing behavior might be explained as following: as temperature increases, the ratio of radiative over non-radiative recombination might decrease, which requires increased injection level for a compensation to maintain lasing operation. For sample A, at temperature above 20 K, the increase of injection cannot compensate the reduced radiative recombination, which might be attributed to small gain volume due to the thin GeSn active layer, and therefore the lasing ceases beyond 20 K. For sample B, the thicker GeSn active layer leads to a higher gain volume, which might offer sufficient compensation via increasing injection until 90 K.

To verify the lasing emission origin, the samples were treated wet chemical etch to remove the well and barrier layers. The GeSn buffer layer was exposed. PL measurement for GeSn buffer was performed to compare with the emission from MQW samples (without etching) using 1064 nm laser. Figure 33(a) shows the PL spectra of sample A. At 10 K, MQW sample

shows two peaks in the PL spectrum, with a higher energy (~2200 nm) and a lower energy peak (~2500 nm) that were assigned to emissions from GeSn buffer and MQW, respectively (according to the band structure calculation shown in section 3). The peak intensity of GeSn buffer is much weaker than that of MQW due to the significantly reduced absorption at GeSn buffer. The PL spectrum of GeSn buffer shows only one peak at ~2200 nm. For the optical pumping measurement, the lasing peak at 10 K is at 2490 nm, very close to the MQW PL and far away from GeSn buffer PL. Therefore, the lasing emission is unambiguously from the MQW. Figure 33(b) shows the PL spectra of sample B. The PL peaks of GeSn buffer and MQW were observed at 2180 nm and 2480 nm, respectively. Since the lasing peak at 10 K was obtained at 2541 nm, considering the lasing peak blue-shift due to band filling, the lasing emission is clearly from MQW.

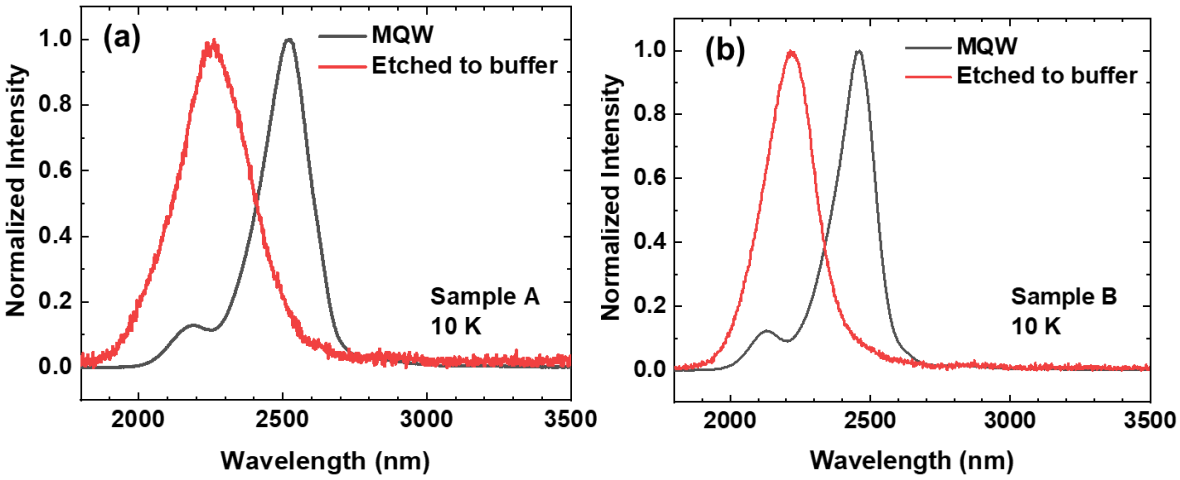

Figure 33. Photoluminescence comparison between GeSn buffer and MQW at 10 K of (a) sample A; (b) sample B. Reproduced from [62], with the permission of AIP Publishing.

The optical confinement factor was investigated to further understand the lasing characteristics. The mode profiles were calculated using a 2D solver. Figure 34 shows the overlap of typical fundamental TE mode with the QW structures for two samples. The numbers

in each figure indicate the GeSn well corresponding to Fig. 27. Since the refractive index of GeSn/SiGeSn shows very low Si- and Sn-compositional dependence, the optical field distribution is similar to that of bulk samples [63]. The optical confinement factor of each layer is listed in Table 5. It can be seen that sample B features the higher overall optical confinement factor of 7.32% compared to sample A of 4.10%.

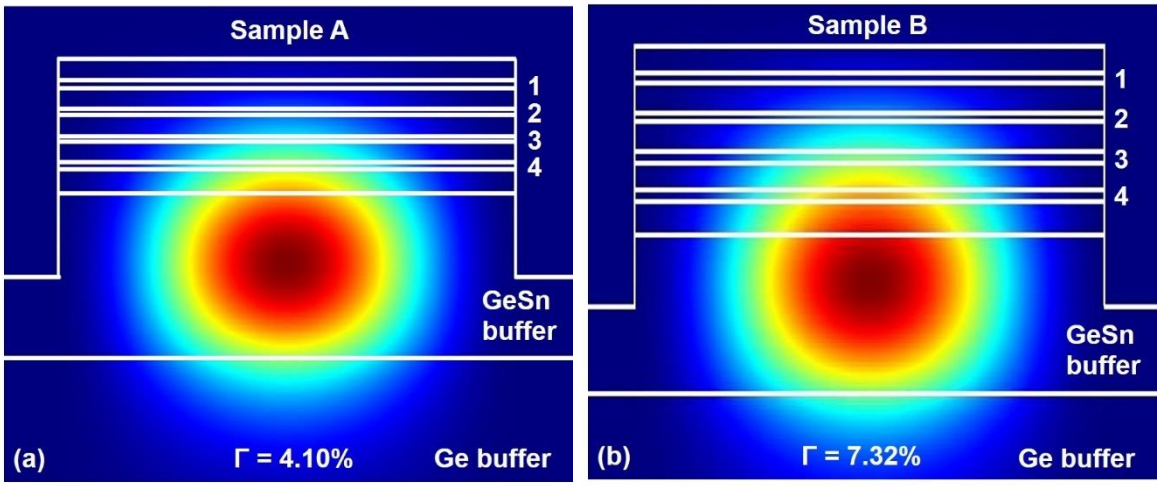

Figure 34. Fundamental TE mode profile for (a) sample A and (b) sample B showing the overlap between optical field and QWs region. The numbers in each figure indicate the GeSn well corresponding to Fig. 27. Reproduced from [62], with the permission of AIP Publishing.

The laser performance in terms of lower threshold and higher maximum operating temperature of sample B is unambiguously superior to that of sample A. The possible relevant factors leading to the better performance of sample B are as follows: i) the overall active layer thickness of sample B (summation thickness of four wells, 118 nm) is 30% thicker than that of sample A (91 nm), resulting in that the gain volume of sample B could be higher than that of sample A; ii) the overlap between optical field and the QWs of sample B is higher, leading to the higher optical confinement factor; iii) the higher Sn composition in GeSn buffer of sample B further relaxes the GeSn well, which could improve the carrier confinement; and iv) the higher

Sn composition in GeSn well of sample B features more bandgap directness, which enhances the radiative recombination.

Table 5. Optical confinement factor of each GeSn well. Reproduced from [62], with the permission of AIP Publishing.

	Sample A	Sample B
1st QW	0.35%	0.35%
2nd QW	0.60%	1.05%
3rd QW	1.06%	2.44%
4th QW	2.09%	3.48%
Total	4.10%	7.32%

The QW lasing characteristics were further analyzed, summarized as follows: i) due to the optical coupling between each two adjacent wells, the Fermi energy could be a constant throughout the QW region. However, the SiGeSn barriers are relative thick for both samples, which might reduce the optical coupling, and therefore the contribution from each well may not be equal; ii) the lasing performance could be improved by adding a Ge cap layer, which increases the overlap between QW region and maximum optical filed region. Our simulation indicated that with a 600-nm-thick Ge cap layer, the improved Γ of 10.25% was obtained for sample B, showing 40% increase; iii) optimizing the SiGeSn barrier and GeSn well thickness, and the numbers of well to achieve sufficient optical coupling and a greater optical confinement factor could further improve the lasing performance. For example, as proposed in Ref. 29, a $Si_{0.1}Ge_{0.75}Sn_{0.15}/Ge_{0.9}Sn_{0.1}$ 20-well structure with 20-nm-thick barrier and 20-nm-thick well would lead to room temperature lasing, which is attainable using the presented CVD growth approach; iv) although it could be argued if the thickness of the QW in this work is sufficiently thin to provide effective 2D density of state, the correlation of the lasing characteristic versus the

gain volume set an effective starting point for future QW laser action region design in terms of selection for the well thickness and number to ensure lasing operation.

In conclusion, two 4-well GeSn QW samples based on SiGeSn/GeSn/SiGeSn structures were grown and characterized. The optically pumped lasing was achieved with both samples. The maximum lasing temperature of 20 K and threshold of 55 kW/cm2 at 10 K were obtained from the thinner well sample; while the thicker well sample shows lower thresholds of 25 and 62 kW/cm^2 at 10 and 77 K, and lasing temperature up to 90 K. Further analysis revealed that the better performance of thicker well sample can be tentatively interpreted as the higher gain volume compared to the thinner well sample. The results reported in this work provide the guidance for the design and optimization of the future higher-performance GeSn QW lasers.

3.3 MQW lasers well number

In the last section, the laser threshold and maximum operating temperature improved with two major factors: higher Sn composition in well, and larger thickness. It is necessary to separate the effect and study separately. Here in this section, experiment was designed to study the well number contribution to the laser characteristics.

The MQW structures were grown via the RPCVD ASM Epsilon® 2000 Plus. Precursor gasses used include commercially available SiH_4, GeH_4, and $SnCl_4$. The growth temperatures were kept below 400 °C, which were compatible to the complementary metal-on-semiconductor process. Figure 35 shows the summarized layer configuration of all samples grown (as well as nominal layer, composition, and thickness information). Three samples with QW numbers of 4, 6, and 10 were grown with no SiGeSn cap layers. Another three samples with 4QW structures were grown with SiGeSn cap layer thickness of 100, 200, and 400 nm. The MQW structures

were wet etched into ridge waveguide structures, having 20 μm of width and 800 nm of height. The Fabry-Perot cavity was formed by cleaving after thinning the Si substrate. The cavity length was kept at 2 mm. The laser was mounted in a cryostat and cooled at low temperatures. A pulsed 1064 nm laser was used as pumping source with a pulse width of 2 ns and repetition rate of 10 kHz. The pumping laser was focused through a cylindrical lens at a stripe with dimension of 20 μm wide by 300 mm long. The emission from the edge of the device was collected and analyzed using the Horiba (Horiba, Kyoto, Japan) iHR 320 spectrometer equipped with an InSb detector, which covers the wavelength range from 1 to 5.5 μm.

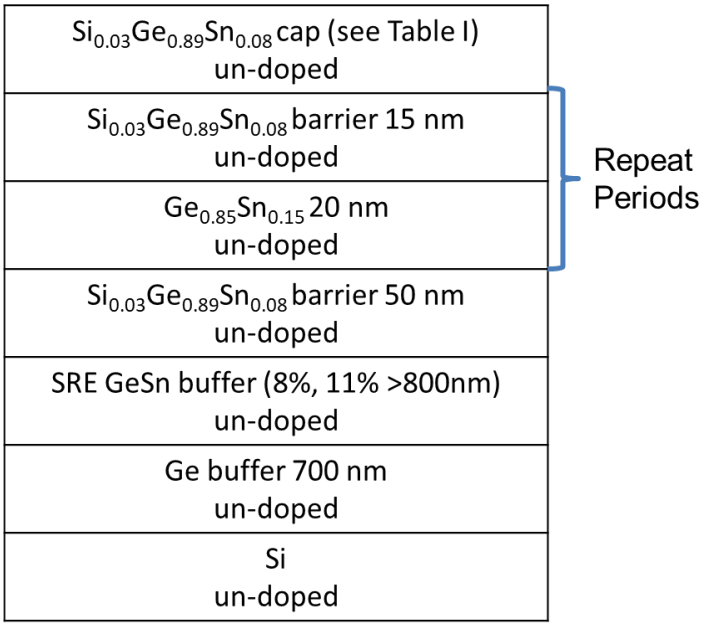

Figure 35. General layer structure for the MQW samples.

The laser characteristics were observed from temperatures starting from 77 K. The maximum operating temperature and threshold pump power density of applicable samples are listed in Table 6. The lasing spectra from the 6QW structure were demonstrated in Fig. 36(a) and light output vs. light input curve in Fig. 36(b). The lasing spectra from the 10QW structure

were demonstrated in Fig. 36(c) and light output vs. light input curve in Fig. 36(d).

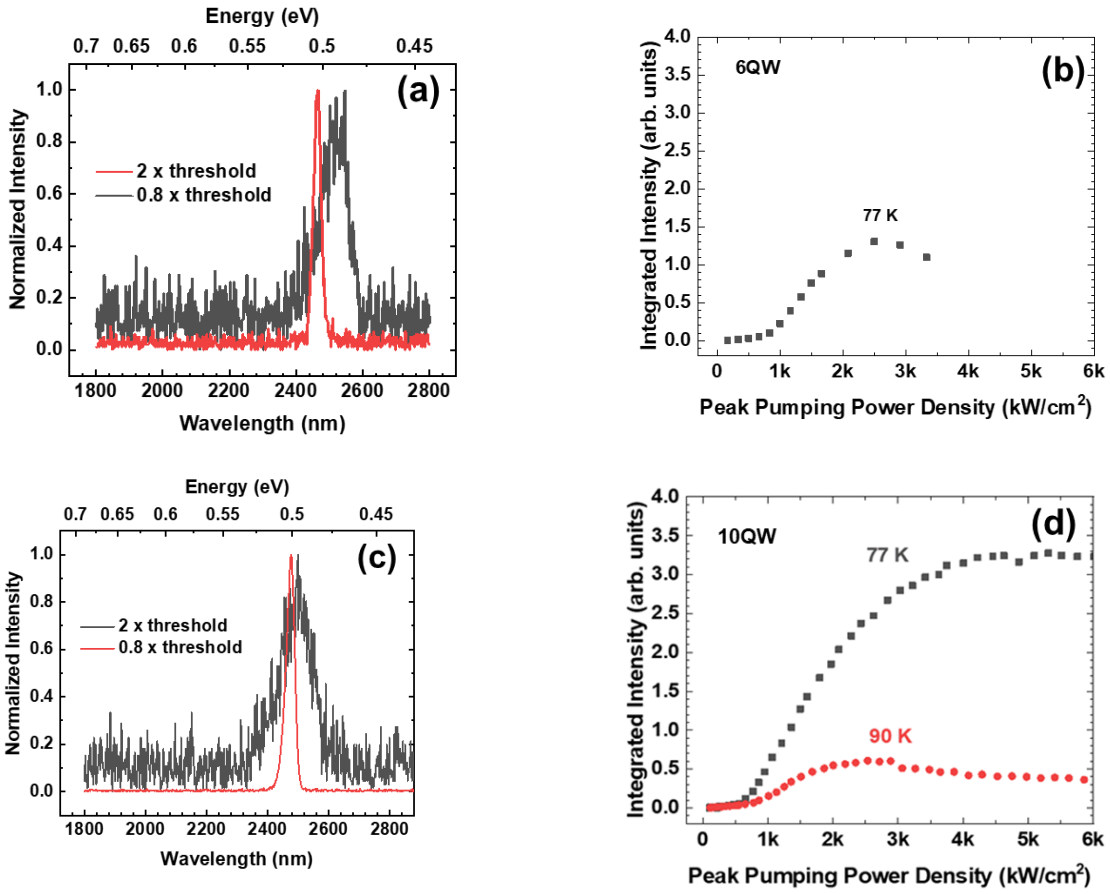

Figure 36. (a) PL emission spectra from 6QW laser; (b) L-L curve from 6QW laser at 77 K; (c) PL spectra from 10QW laser; and (d) L-L curve from 10QW laser at 77 and 90 K.

Table 6. Summary of laser threshold power density at each operation temperatures

4QW	6QW	10QW
NA	77 K, 913 kW/cm^2	77 K, 622 kW/cm^2
		90 K, 694 kW/cm^2

NA: no lasing observed at 77 K.

The set of non-capped MQW samples showed a clear trend on the maximum operating temperatures and threshold power density. For the 4QW sample with no cap layer, lasing was not observed owing to the inadequate modal gain to overcome the loss. In contrast, 6QW sample

demonstrated lasing at 77 K with threshold of 913 kW/cm^2. For 10QW sample, the lasing threshold was reduced to 622 kW/cm^2 at 77 K and the maximum operating temperature increased to 90 K. The emerging of lasing transition with higher QW number is owing to the increasing of total gain (approximately proportional to N times the gain from a single QW) and reduced fermi energy level at a given carrier density [64]. Due to the imperfection of GeSn MQW growth, the laser structure has considerably high loss. For small well number, achieving sufficient gain for lasing requires the increase of carrier density, which will eventually lead the fermi level close to the energy level in QW. In this scenario, the gain will be saturated no longer increase with the carrier density. As a result, large QW number would be desired to provide enough total gain, while reduce the fermi energy level. Furthermore, in larger QW number structure, under optical pumping scheme, the pumping light absorption and higher optical confinement factor (Γ) make further contribution to reduce the threshold as well as to maintain high gain at elevated temperatures.

Optically pumped SiGeSn/GeSn MQW lasers were studied with changing of QW number. To overcome the existing loss in the given structure, six QWs were needed to achieve lasing at 77 K. The 10QW structure exhibits a lower threshold and operating temperature up to 90 K.

3.4 MQW lasers with SiGeSn cap

In last section, the SiGeSn/GeSn MQW laser has a low optical confinement factor. The Ge refractive index is quite high at ~4. The GeSn has higher index, makes the mode resides mostly in the GeSn buffer layer. This mode profile can be adjusted upward to the MQW region by adding a SiGeSn cap. Therefore, the optical confinement will increase as the cap thickness,

leading to higher modal gain to overcome the existing loss in the structure.

A set of 4QW samples was studied to improve Γ by increasing SiGeSn cap layer thickness. The MQW structure suffers from low confinement factor due to poor overlap of the active region and the confined optical field because the maximum of the optical mode is in the GeSn buffer layer, as schematically shown in Fig. 37. Four samples were used with the SiGeSn cap layer thickness of 0, 100, 200, and 400 nm. The etch depth kept at 800 nm. The design of adding SiGeSn cap layer is aimed at coupling more light into the MQW active region by building large refractive index above the MQW region. The fundamental TE mode was calculated in Fig. 38. The optical confinement factor was calculated for each device (1.4%, 2.5%, 3.4% and 4.5%, for device with thickness from 0 to 400 nm, respectively). More than three times improvement can be achieved compared the 0 nm cap to 400 nm cap device.

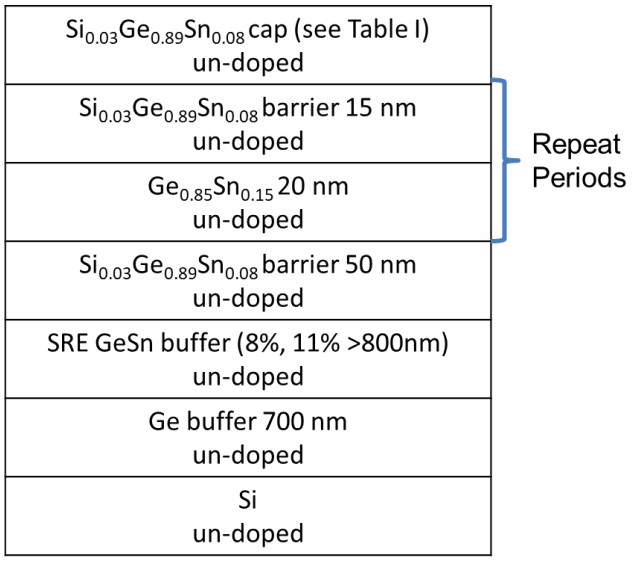

Figure 37. General layer structure for the MQW samples

No lasing was observed from the devices either with no cap device and or a 100-nm cap

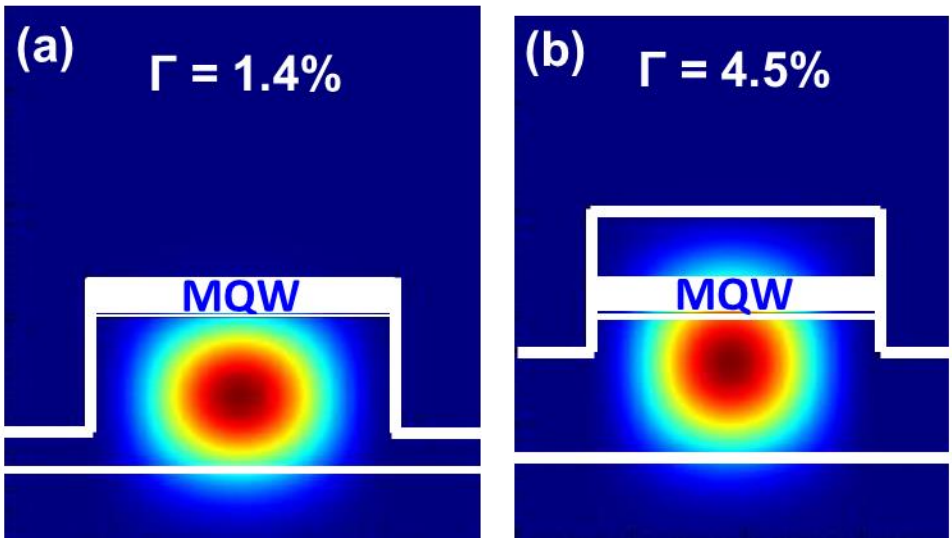

Figure 38. Fundamental mode of the 4QW structure using refractive index calculated at 2.5 μm. (a) 0 nm cap and (b) 400 nm cap.

samples at 77 K. Lasing was achieved for both structures with a cap of 200 and 400 nm at 77 K. In this set of 4QW samples, the 200 nm capped structure resulted in the lowest threshold. The 400 nm capped device has a significantly higher threshold. Further examination on the slope efficiency and maximum output for the two lasing devices, the result implies the material gain remain similar. These effects imply other loss mechanism emerges as the cap thickness further increased. The loss channel is believed mainly from the in-efficient injection of absorbed carriers into the MQW region.

The set of non-capped MQW samples showed a clear trend on the maximum operating temperatures and threshold power density. For the 4QW sample with no cap layer, lasing was not observed owing to the inadequate modal gain to overcome the loss. In contrast, 4QW sample with 200 nm cap demonstrated lasing at 77 K with threshold of 913 kW/cm^2. The spectra of 200-nm capped 4QW sample are shown in Fig. 39(a); the L-L curve at 77 K is shown in Fig. 39(b). For 400-nm capped 4QW sample, the lasing threshold was reduced to 622 kW/cm^2 at 77 K and the maximum operating temperature increased to 90 K. The emission spectra and L-L

curve for 400 nm cap are plotted in Fig. 39(c) and (d), respectively. The threshold and T_{max} of the devices are summarized in Table 7. The emerging of lasing transition with thicker cap from 0 to 200 nm indicates an improvement of the optical confinement factor, which increases the modal gain. As the result, the threshold was reduced. Further increase of the cap thickness resulted in an increase of threshold. This could be a partial relaxation of SiGeSn cap layer, where dislocation becomes considerable to allow carriers recombine non-radiatively before they reach the MQW region.

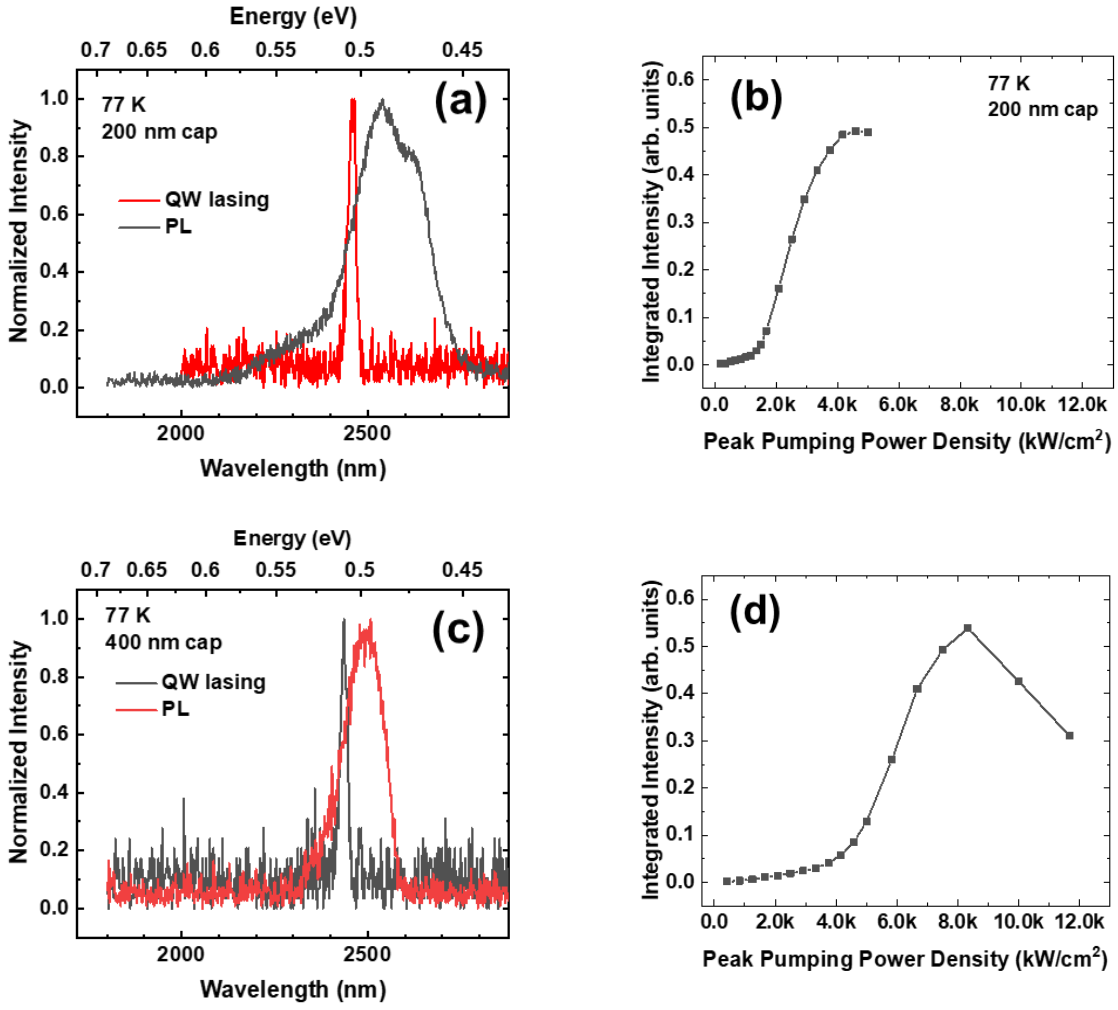

Figure 39. (a) PL emission spectra from 4QW laser with 200 nm cap; (b) L-L curve from 4QW laser with 200 nm cap; (c) PL spectra from 4QW laser with 400 nm cap; and (d) L-L curve from 4QW laser with 200 nm cap. All measurements were taken at 77 K.

Table 7. Summary of laser threshold power density at each operation temperatures and optical confinement factor

SiGeSn cap Thickness	T_{max}, P_{th}	Optical confinement Γ
no cap	NA	1.4%
100 nm	NA	2.5%
200 nm	77 K, 1494 kW/cm^2	3.4%
400 nm	77 K, 4316 kW/cm^2	4.5%

To conclude, optically pumped SiGeSn/GeSn 4QW lasers were studied with changing of SiGeSn cap layer thickness. Adding SiGeSn cap layer thickness improves the optical confinement with a factor of 3.2, leading to lasing achieved at 77 K. Further increase the thickness to 400 nm leads to increase of threshold, which is likely due to the recombination of carriers before they reach to the MQW active region.

Chapter 4: Light-emitting diodes for electrical injection analysis

With abundant efforts developed in optically pumped GeSn lasers, lasing from GeSn through electrical injection remain empty. We must acknowledge the effort making from zero to one is rather difficult. But there are fractions of increment can be understood before getting the lasing transition. One step connection is to achieve a good light-emission by using LEDs. Although one can argue the LED and laser works under fundamentally different principles, they do share a lot in common in terms of carrier injection. The optically pumped lasers demonstrated great potentials for lasing. The major difference between the electrically injected laser and optically pumped laser is the method of carrier injection. The LED is a great choice for analyzing the carrier dynamic for the light emission from the GeSn active region. So, the study of GeSn structure LED become a key to untangle the limit factors that prevent the GeSn from lasing through electrically injection.

4.1 Ge/GeSn/Ge double heterostructures

Recently, studies on group-IV semiconductor GeSn alloys open a new window for the development of Si-based optoelectronics active devices [12,19,21,22,24,29, 65-68]. Since a direct bandgap, GeSn has been experimentally identified [18] and an optically pumped GeSn-based laser has been demonstrated [31], the GeSn-based light emitter as the low-cost Si-based light source is expected to be efficient, with which all necessary components for mid-IR sensing on a Si platform will soon be available. In addition, by varying the Sn composition in the GeSn alloy, the operating wavelength of the GeSn based LED could cover a broad mid-IR range. Preliminary investigation of EL from GeSn active layers has been conducted by several research groups [19,21-24,51,67,69-71]. For the purpose of improving the device performance, some

advanced device structures such as DHS and MQW were studied [23,54,66,69], which offer better carrier confinement so that the light emission efficiency can be significantly improved. Particularly, the band structure of the Ge/GeSn/Ge DHS in this study features a higher density of states compared to the MQW whose energy states are quantized in the growth direction. As a result, the high carrier concentration in an active GeSn layer can be achieved at a high injection level. Therefore, the DHS-based LED holds the possibility of high-power emission.

To fully develop the heterostructure-based GeSn LED technology, a detailed device study including temperature-dependence, injection-dependence, and Sn compositional-dependence is necessary, which currently is still missing. In this work, the comprehensive study of GeSn LEDs was presented based on the Ge/GeSn/Ge p-i-n DHS with the Sn compositions up to 9.2%. Temperature-dependent PL and EL spectra have been characterized from 300 to 77 K for each device. The room temperature integrated EL intensity versus current injection was further investigated, which shows the monotonic-increase feature. Based on the experimental data and theoretical calculation, the band structure of the device is discussed, which reveals that the type-I band alignment was achieved.

The DHS GeSn LED samples were grown using an ASM Epsilon® 2000 Plus RPCVD system. The complete layer sequence includes: (1) a 750-nm-thick p-type doped Ge layer (also serving as the buffer layer); (2) a 200-nm-thick unintentionally doped $Ge_{1-x}Sn_x$ active layer; and (3) a 50-nm-thick n-type doped Ge cap layer. Since the concentration of background doping of the $Ge_{1-x}Sn_x$ layer was measured to be slightly p-type doped, in order to achieve a good PN junction, the doping concentrations of p- and n-type Ge layers were selected as 5×10^{18} and 1×10^{19} cm^{-3}, respectively. The p-type Ge buffer layer was grown on a Si substrate using a two-step growth process (a low-temperature 100 nm undoped seed layer and a higher temperature 650 nm

p-type doped layer) followed by an *in-situ* annealing to reduce the defects. The reactor was then cooled down to 350 ºC in H_2 and after which $SnCl_4$ and GeH_4 were introduced into the chamber to initiate GeSn growth. Finally, a 50-nm-thick n-type Ge cap layer was deposited at the same temperature to avoid Sn-precipitation. The pseudomorphically grown Ge cap layer also served as the passivation layer to reduce the surface recombination. Three samples were grown with the Sn compositions up to 9.2% in this study. A detailed growth mechanism was discussed in the previous report [61].

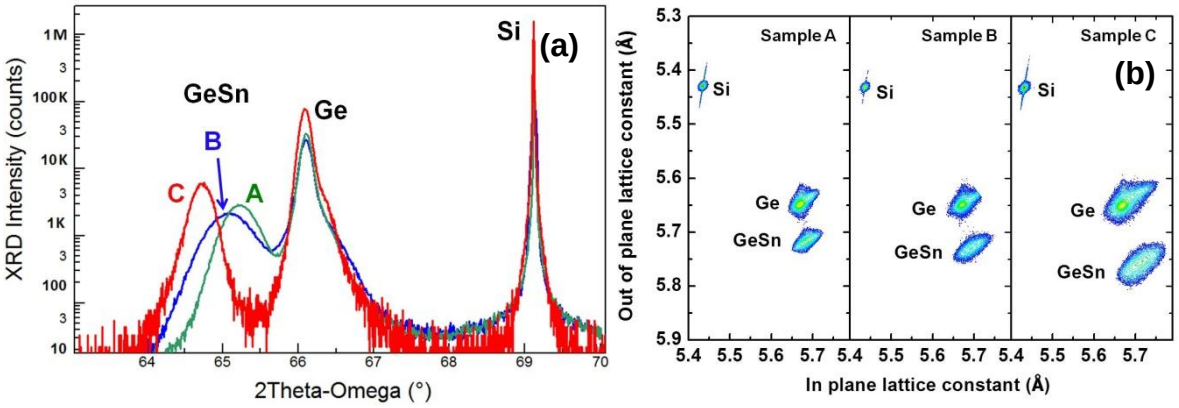

Figure 40. (a) The 2θ-ω scan of GeSn and Ge layers. As the Sn composition increases, the GeSn peak shifts towards to lower angle. The information of samples A, B and C are shown in Table I. (b) RSM from (-2 -2 4) plane of Ge and GeSn layers. The different strain states of the p- and n-type Ge layers results in the asymmetric contour plot of Ge. The GeSn layers are compressively strained. Reproduced from [72], with the permission of AIP Publishing.

After growth, the material quality, the layer thickness, the Sn composition and the strain of the as-grown wafer were carefully analyzed by using TEM and high-resolution XRD techniques. The 2θ-ω scan is shown in Fig. 40(a). The Si, Ge, and GeSn peaks are clearly resolved. As the Sn composition increases, the GeSn peak shifts towards a lower angle. The RSM is plotted in Fig.40(b), which reveals that all GeSn layers were compressively strained (in-plane). The asymmetric contour plot of Ge was observed. This is due to the different strain states of the p-type Ge buffer layer (relaxed) and n-type Ge cap layers (in-plane tensile strain).

The TEM results showed that the majority of the defect was localized at the Ge/Si interface because of the optimized growth of the Ge buffer layer, leading to the low-defect GeSn layers. The density of threading dislocations was extracted from RSM [73]. The measured thickness of each layer agreed well with the initial device design. The material characterization results are summarized in Table 8. The negative value of strain indicates the compressive strain.

Table 8. Summary of material characterization. plane of Ge and GeSn layers. The different strain states of the p- and n-type Ge layers results in the asymmetric contour plot of Ge. The GeSn layers are compressively strained. Reproduced from [72], with the permission of AIP Publishing.

Sample #	Measured Sn (%) by XRD	p-type Ge strain (in-plane)	GeSn layer strain (in-plane)	n-type Ge strain (in-plane)	Density of threading dislocations (cm^{-2})
A	6.06%		-0.51%	0.57%	2.14×10^{7}
B	6.44%	Relaxed	-0.43%	0.58%	3.91×10^{7}
C	9.24%		-0.48%	0.93%	7.15×10^{7}

The temperature-dependent PL characterization was conducted to further examine the material optical quality. The PL measurements were performed using a standard off-axis configuration with a lock-in technique (optically chopped at 377 Hz). A continuous wave (CW) laser with 532 nm wavelength was used as an excitation source. The laser beam was focused down to a 100 μm spot and the power was measured to be 560 mW. The PL emission was collected by a spectrometer and then sent to a thermoelectric-cooled lead sulfide (PbS) detector with a cutoff at 3.0 μm.

Figure 41(a) shows the PL spectra of samples A, B and C at the temperatures from 300 to 77 K. Based on the bandgap energy calculation, all GeSn layers in this study are indirect

bandgap materials. However, due to the small energy separation between the direct and indirect bandgap (cf. Table 10), a portion of photo-generated electrons transfer from L- to Γ-valley via thermal activation, resulting in significantly enhanced direct bandgap emission. Therefore, the main peak of each spectrum in Fig. 41(a) is attributed to the direct bandgap transition [74]. The PL peak of indirect bandgap transition cannot be identified because its peak position is close to the direct peak and its intensity is weaker compared to that of the direct peak. The PL peak blue-shift at low temperature was observed as expected. At 300 K, the PL peaks at 0.636, 0.605 and 0.548 eV were obtained for the samples A, B, and C, respectively. In addition, the reduced PL intensity at low temperature was observed, which further confirms the indirectness of GeSn bandgap. The emission decreases with decreasing temperature can be explained as following: due to the small energy difference between direct and indirect bandgap, more thermal activated electrons populate the Γ-valley at 300 K, resulting in direct bandgap transition dominates the PL

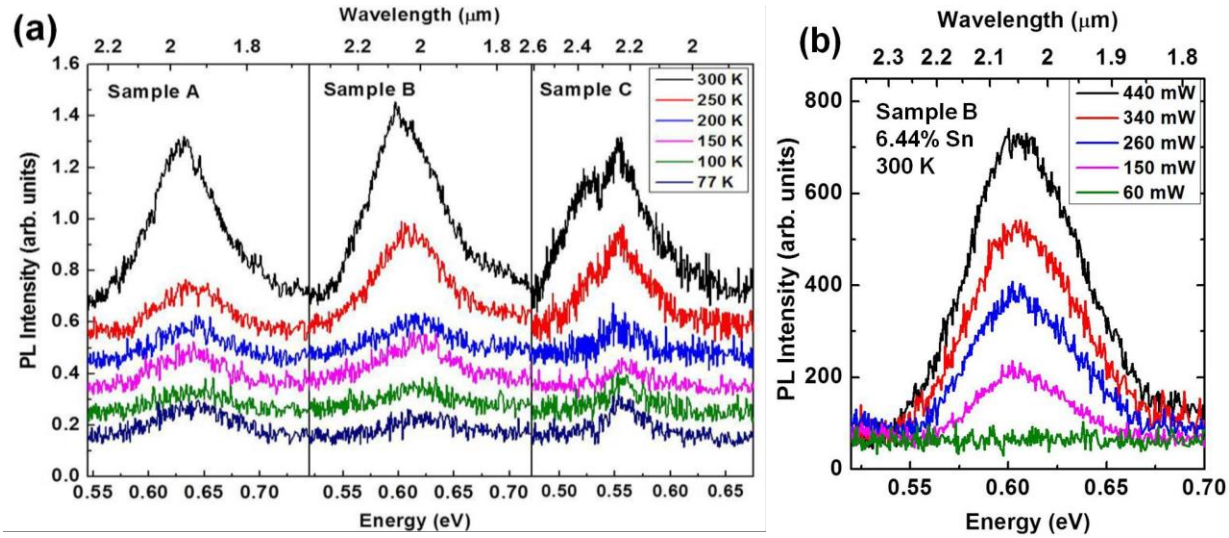

Figure 41. (a) Photoluminescence spectra of Ge/Ge1-xSnx/Ge DHS samples at the temperatures from 300 to 77 K. As temperature decreases, the blue-shift of the PL peak was observed for each sample. The decreased PL intensity at low temperature indicates the indirectness of GeSn bandgap; (b) Pumping power-dependent PL spectra for sample B at 300 K. plane of Ge and GeSn layers. The different strain states of the p- and n-type Ge layers results in the asymmetric contour plot of Ge. The GeSn layers are compressively strained. Reproduced from [72], with the permission of AIP Publishing.

spectrum. As temperature decreases, the PL intensity decreases with a more rapid drop of the direct peak than the indirect peak. This is due to the reduced thermal excitation of electrons and less phonon-assisted indirect radiative recombination. At the temperature below 100 K, the indirect bandgap transition dominates the PL spectrum. However, owing to the dramatically reduced indirect radiative recombination, the overall PL intensity significantly decreases.

The optical properties of the material were further studied by pumping power-dependent PL measurement. The typical PL spectra for sample B are plotted in Fig. 41(b). At low pumping power of 150 mW, both indirect and direct bandgap transitions contribute to the PL emission, resulting in the broad peak line-width. As pumping power increases, more carriers intend to populate the direct Γ-valley, therefore, the direct bandgap transition dominates the PL, which reduces the peak line-width at higher pumping power, as shown in Fig. 41(b).

The samples were fabricated into circular mesa structures with diameters of 100, 250 and 500 μm using photolithography and etching processes. Both dry etch (Reactive-ion etching, RIE) and wet chemical etch methods were investigated for mesa etching. The etching rate of RIE (reaction gases of 30 sccm CF_4 and 30 sccm Ar) was measured as 30 nm/min and it was found to be Sn compositional dependent: higher Sn composition resulting in the lower etching rate. The wet chemical etch (HCl: H_2O_2: H_2O = 1:1:20 at room temperature) showed a stable etching rate of 100 nm/min regardless of Sn composition, which was then utilized in this work. The detailed study of etching mechanism will be reported elsewhere. The p- and n-type metal contacts consist of 10 nm Cr and 200 nm Au defined by metal deposition and liftoff processes. Figures 42(a) and (b) show the schematic cross-sectional view and scanning electron microscope (SEM) top view of the device, respectively.

The diode characterization was performed using an independent measurement system (no

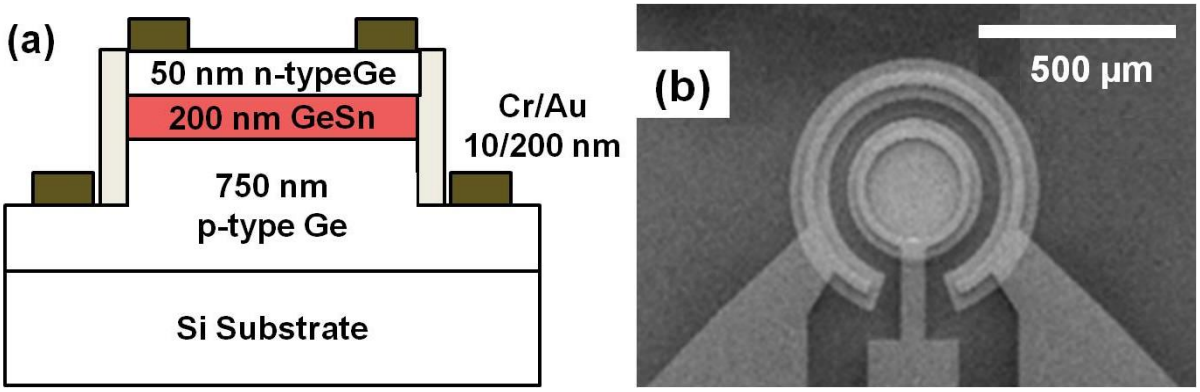

Figure 42. (a) Schematic cross-sectional view of GeSn LED. (b) Top view SEM image of the device. Reproduced from [72], with the permission of AIP Publishing.

component shared with the PL measurement system). The current-voltage (I-V) characteristic of the DHS LEDs was measured at temperatures from 300 to 77 K with a Keithley 236 (Keithley Instrument, Cleveland, OH) direct current (DC) source unit. A pulsed current source with a pulse width of 250 µs and duty cycle of 10% was applied for temperature dependent EL measurement. The EL emissions from the device were sent to a spectrometer through a carefully aligned optical system, and the collected light was then detected by a PbS detector.

Figure 43(a), (b) and (c) show the typical current-voltage (I-V) characteristics of the LED devices measured at temperatures from 300 to 77 K (mesa diameter of 500 µm). The rectifying characteristic was observed at each temperature. As the temperature increases, for each device, the current increases due to more thermally excited carriers. Moreover, the dark current increases as the Sn composition increases under the same bias voltage because of the further reduced bandgap. The dynamic resistances at room temperature were extracted as 52.9, 28.0, and 19.0 Ω (operating at around 0.5 V) for samples A, B, and C, respectively. The relatively high dynamic resistance may arise from the thin n-type contact layer (50 nm Ge cap).

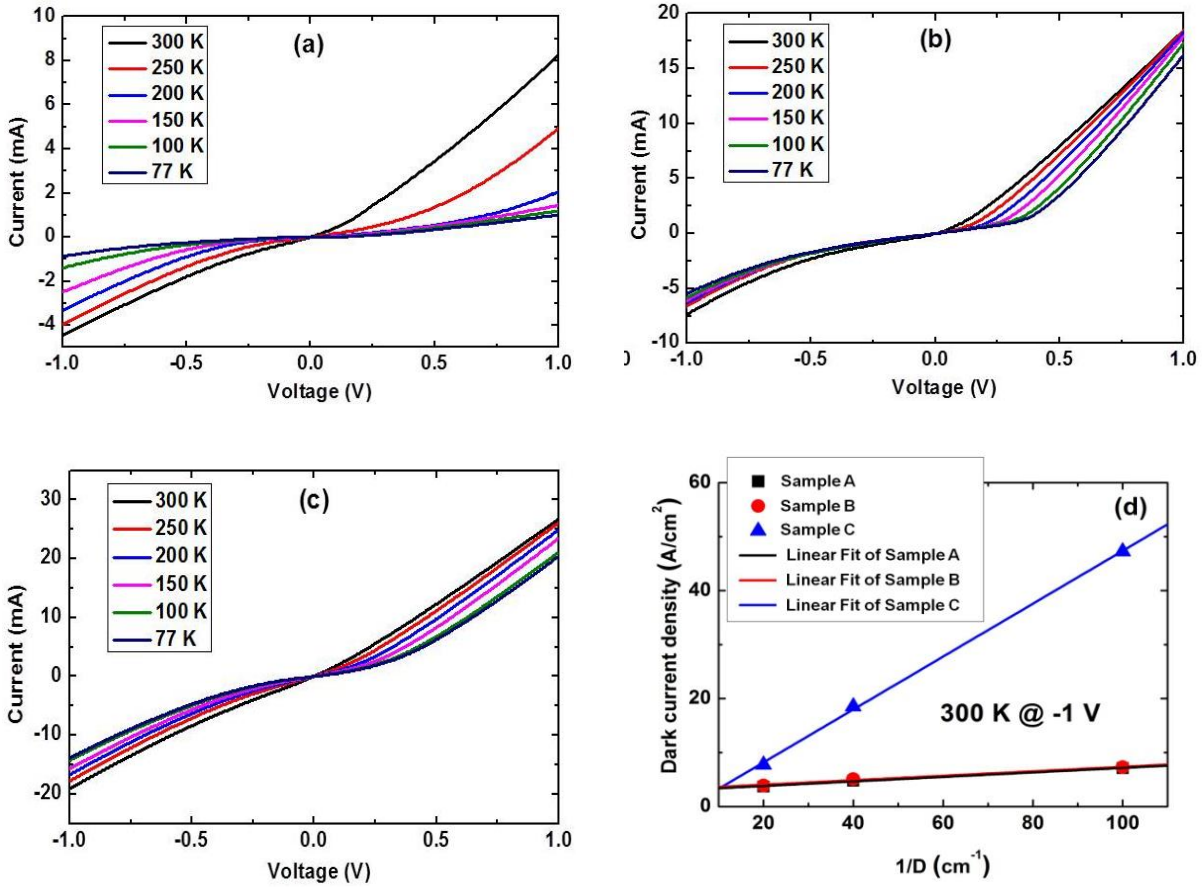

Figure 43. Dark current-voltage (I-V) characteristics of the devices Sn compositions of samples (a) A, (b) B and (c) C showing the rectifying behavior at the temperatures from 300 to 77 K (mesa diameter of 500 μm). (d) Dark current densities at -1 V as functions of 1/*D* (*D* = diameter of the mesa). Reproduced from [72], with the permission of AIP Publishing.

The room temperature dark current under reverse bias was further investigated. The dark current I_{dark} mainly consists of two components: bulk leakage current I_{leak} which is usually proportional to the device area and peripheral surface leakage current I_{surf} which relates to the periphery of the device. The dark current density can be described as:

$$J_{dark} = J_{leak} + 4J_{surf} / D \qquad \text{(Equation 4.1)}$$

where D is the diameter of the mesa, J_{dark}, J_{leak}, and J_{surf} are dark, bulk leakage and peripheral surface leakage current density, respectively. By linear fitting of the measured data and by using

equation (1) (see Fig. 43(d)), the Jsurf at -1 V were extracted as 10.2, 10.4 and 122.5 mA/cm for samples A, B and C, respectively.

As the Sn composition increases, the peripheral surface leakage current increases. The relatively high dark currents are mainly due to the following reasons: (1) No passivation for the surface and the sidewall of the mesa, resulting in the large peripheral surface leakage current; (2) The narrowed bandgap of Ge1-xSnx alloy leads to more thermally excited carriers; (3) As Sn composition increases, the lattice mismatch between GeSn and Ge increases, resulting in the increased defect density at the Ge/$Ge_{1-x}Sn_x$ interfaces, which contributes to the bulk leakage current. The peripheral surface leakage current can be reduced by depositing a passivation layer on the mesa surface and sidewall (reduces the surface recombination velocity) according to a report that showed the significantly suppressed dark current of a $Ge_{0.95}Sn_{0.05}$ photodiode with a Si passivation technique [75].

Temperature-dependent EL spectra under an injection current density of 255 A/cm^2 are shown in Fig. 44. The LEDs with mesa diameter of 500 μm were selected for EL study since they feature lower dark current density. For each device, as the temperature decreases from 300 to 77 K, the EL intensity decrease was observed, which agrees with the emission behavior of indirect bandgap material. The main emission peak at each temperature is determined to be the direct band-to-band transition. The position of the main peak blue-shifts as the temperature decreases from 300 to 77 K, which can be explained by the Varshni relation [22]. For the samples A, B and C, the main peak shifts from 0.638 to 0.650 eV, 0.606 to 0.612 eV and 0.537 to 0.546 eV, respectively. Note that since a lock-in amplifier and a chopper at the frequency of 377 Hz (selected as a trade-off of detector response frequency and the measurement time) were employed for the EL measurement, the signal is averaged over a complete pulse on-and-off cycle

(0.2 ms). Considering the low duty cycle, only the first harmonic is extracted by the lock-in amplifier. With the relatively short integration time, the signal-to-noise ratio (SNR) is low, resulting in an increased noise level of the EL spectra.

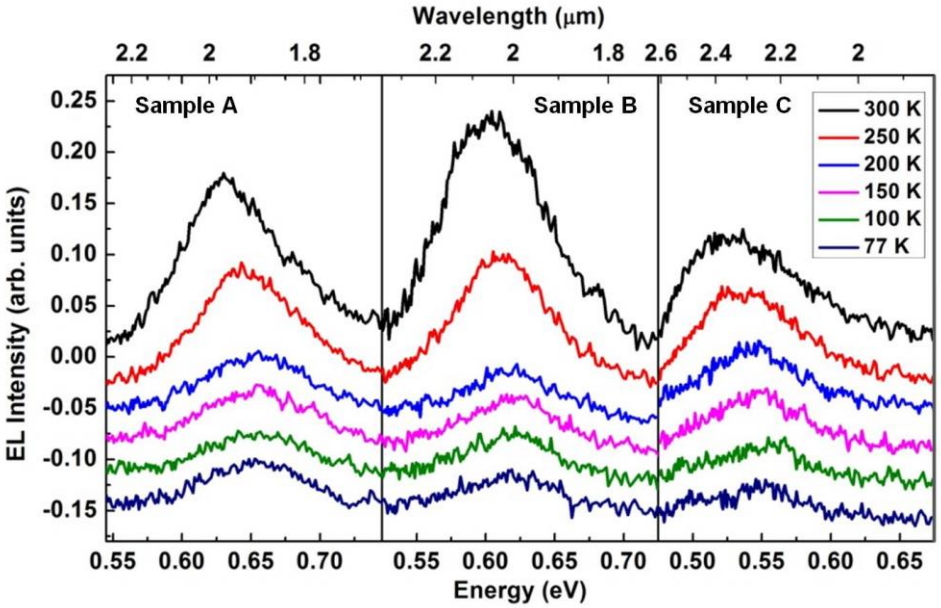

Figure 44. Electroluminescence spectra of Ge/Ge1-xSnx/Ge DHS samples at the temperatures from 300 to 77 K under an injection current density of 255 A/cm^2. Reproduced from [72], with the permission of AIP Publishing.

The peak positions of EL spectra were extracted via Gaussian fitting, as shown in Fig. 45(a) as solid symbols. The solid curves were fitted based on the Varshni relation: $E(T) = E(0)-\alpha T^2/(T+\beta)$, where T is the temperature, $E(0)$, α, and β are material-dependent parameters [76]. For samples A, B, and C, the values of $E(0)$, α, and β are summarized in Table 9.

Figure 45(b) shows the integrated EL intensities of the LED devices under various injection current densities from 102 to 357 A/cm^2. The monotonic increase of integrated EL intensities was observed for each sample, indicating that the maximum emission has not been reached yet. Theoretically, the device with the higher Sn composition would have the stronger

Table 9. Summary of parameters fitted by Varshni relation.
Reproduced from [72], with the permission of AIP Publishing.

Sample #	$E(0)$ (eV)	α (eV/K)	β (K)
A	0.662	1.94×10^{-4}	237
B	0.616	6.32×10^{-4}	258
C	0.558	1.58×10^{-4}	276

emission intensity at the same current injection and temperature due to more injected carriers populating the Γ-valley in the CB. However, sample B shows the highest EL intensity. This may be due to the better material quality compared to sample C. The lower material quality of sample C leads to enhanced non-radiative recombination such as SRH recombination (recombination through the defect energy levels), which reduces the emission efficiency, resulting in the weaker EL intensity. To deeply understand the DHS LED characteristics, the electronic band structures of the samples in this study are discussed in the following section.

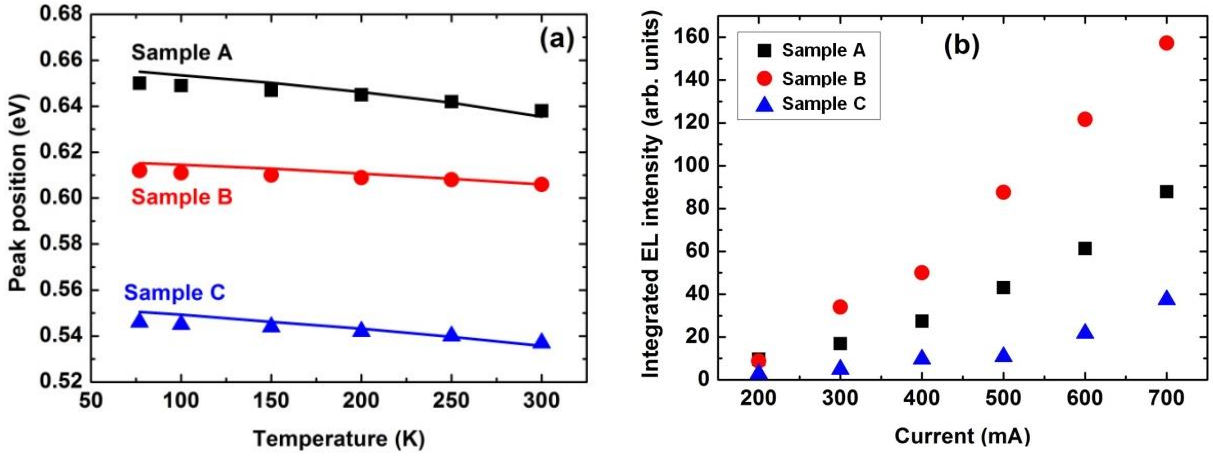

Figure 45. (a) EL peak positions at temperatures from 300 to 77 K. The solid symbols were extracted from Gaussian fitting and the solid curves were fitted based on Varshni relation; (b) Integrated EL intensities at 300 K under various current injection densities from 102 to 357 A/cm^2 of the GeSn DHS LEDs. Reproduced from [72], with the permission of AIP Publishing.

The electronic band structures of Ge/$Ge_{1-x}Sn_x$/Ge DHS samples were investigated. The bandgap energies were calculated using a quadratic equation with bowing parameters, and the strain induced bandgap changes were obtained using the deformation potential model [54,66]. Figure 46 shows the band structure diagram of GeSn alloys in this study. The E_g^{Γ} and E_g^{L} are direct and indirect bandgap energies, respectively. Their difference is represented as ΔE_g. It has been reported that the band structure of GeSn alloy is determined by two main factors [30,54,67]: 1) Sn composition. The incorporation of Sn into Ge pushes down both Γ- and L-valleys in the conduction band (CB), while lifting the valence band (VB); 2) Strain. Since the GeSn alloys were grown on Ge buffer layer in this study, the alloys are under compressive strain, which brings Γ-valley up, altering the band structure of alloy towards indirectness. In addition, the compressive strain splits the HH and LH degeneracy in the VB by lifting the HH band. Our calculation showed that all three samples in this study remain indirect bandgap material, which agrees well with the band structure analysis in Ref. 55, 66, and 67. The direct and indirect bandgap energies are summarized in Table 10.

For the estimation of band alignment, the method explained in Ref. 50 was followed, which applied the average band offset for VB based on Jaros' theory [29] and took the spin-orbit splitting into account but ignored the HH and LH bands separation. Figure 46(b) shows the band alignment diagram of DHS samples (not to scale). The ΔE_c^{Γ} and ΔE_c^{L} are barrier heights at Γ- and L-valleys in the CB, while the ΔE_{v1} is the barrier height in the VB between the p-type Ge and GeSn layers, respectively. Due to the in-plane tensile strain, the n-type Ge cap layer exhibits reduced bandgap energy, resulting in the reduced value of barrier height ΔE_{v2} between GeSn and n-type Ge layers. The E_g^{Γ} and E_g^{L} are energies of GeSn direct and indirect bandgap, respectively. The ΔE_1 represents the energy difference between the CB minimum at the L point

of the p-type Ge barrier and the CB minimum at the Γ point of the GeSn layer, while the ΔE_2 is the energy difference between the Γ-valley minimum of GeSn and the L-valley minimum of the n-type Ge cap layer. The reduced bandgap energy of the Ge cap layer leads to the smaller value of ΔE_2 compared to ΔE_1. The band alignment calculation results of all three samples are summarized in Table 10.

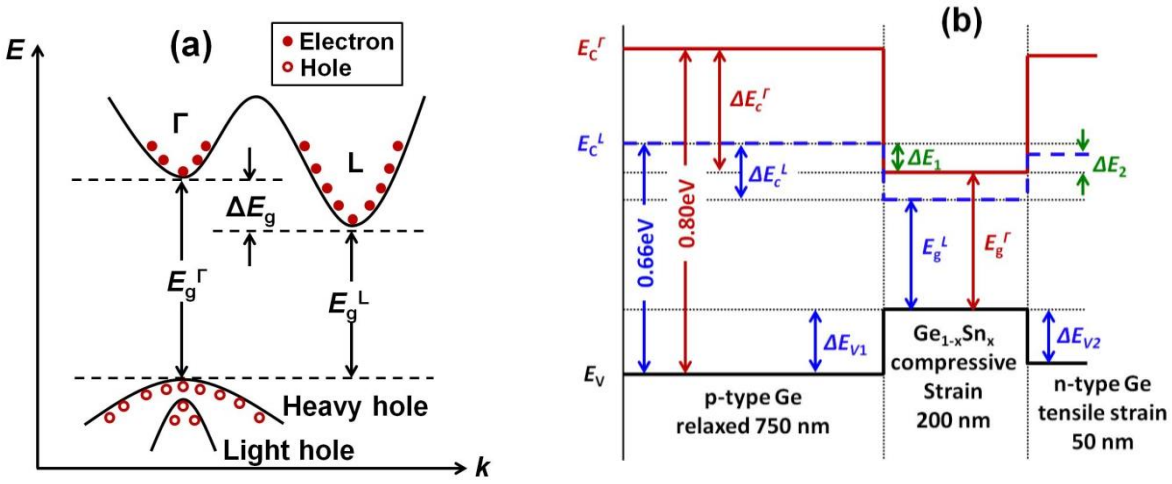

Figure 46. Ge/Ge1-xSnx/Ge DHS electronic band structure (not to scale). (a) Band structure diagram of GeSn alloys. All three samples in this study remain indirect bandgap material; (b) Band alignment diagram of DHS samples. Type-I band alignment was indicated for samples B and C, which provides a favorable carrier confinement for the devices. The Ge cap layer exhibits reduced bandgap energy due to the in-plane tensile strain. Reproduced from [72], with the permission of AIP Publishing.

Table 10. Summary of $Ge/Ge_{1-x}Sn_x/Ge$ DHS band structure. Reproduced from [72], with the permission of AIP Publishing.

Sample #	ΔE_c^{Γ} (meV)	ΔE_c^{L} (meV)	ΔE_{v1} (meV)	ΔE_{v2} (meV)	E_g^{Γ} (eV)	E_g^{L} (eV)	$\Delta E_g = E_g^{\Gamma} - E_g^{L}$ (meV)	ΔE_1 (meV)	ΔE_2 (meV)
A	120	28	43	40	0.637	0.589	48	-20	-28
B	162	46	66	62	0.572	0.548	24	22	12
C	187	64	72	46	0.541	0.524	17	47	11

For sample A, the DHS provides electron confinement at both Γ- and L-valleys in the CB

with the barrier heights of ΔEcΓ = 120 meV and ΔEcL = 28 meV, respectively. However, the CB minimum at the Γ point of GeSn is 20 (28) meV above the CB minimum at the L point of the p- (n-) type Ge layer (cf. Table 9, represented as negative values of ΔE1 and ΔE2), indicating the lack of electron confinement for Γ-valley. The barrier heights in VB were found to be 43 and 40 meV at p- and n-type Ge layers, respectively.

For samples B and C, the CB minima at the Γ points of GeSn are below the CB minimum at the L points of the p- and n-type Ge barriers, with ΔE_1 = 22, 47 meV, and ΔE_2 = 12, 11 meV for sample B and C, respectively, indicating the type-I band alignment of DHS, which provides a favorable carrier confinement for the device. It is worth noting that although type-I band alignment was achieved, since the barrier heights are smaller than the room temperature thermal energy (1 kBT $\approx$ 25 meV), the electron confinement for the Γ-valley is insufficient, resulting in the low efficiency of LED emission.

To optimize the DHS-based LED for improvement of emission efficiency, the following instructions are proposed: 1) using a direct bandgap GeSn well, which can be achieved either by incorporating more Sn or by growing a thicker GeSn layer to relax the material [31]. Based on the theoretical calculation, fully relaxed GeSn with 9% Sn or fully strained GeSn (compressively, pseudomorphic to Ge) with 15% Sn could achieve direct bandgap material. Therefore, the Sn composition can be selected from 9 to 15% with appropriate strain; 2) using ternary material SiGeSn as the barrier instead of Ge, which offers separate tuning of bandgap and lattice constant by varying the Si and Sn compositions [54]. Moreover, optimizing the doping profile (including contact layers and background doping of the GeSn active layer) would also improve the device performance in terms of reducing dark current and series resistance.

In summary, the Ge/GeSn/Ge DHS LEDs were investigated at temperatures from 300 to

77 K with Sn compositions up to 9.2%. A systematic study of I-V and EL characteristics has been conducted. The surface leakage current was extracted from I-V characteristics, whose relative high value is mainly due to the non-passivated surface of the device. The temperature-dependent EL spectra show blue-shift of the main peak that is attributed to the direct bandgap transition. The integrated EL intensity exhibits a monotonic increase as the current injection increases and has not yet reached the maximum output. The electronic band structures of DHS were further investigated. Type-I band alignment has been achieved for samples B and C. Since the carrier confinement for the samples in this study is insufficient, which results in the low-efficiency light output, viable solutions for the improvement of emission efficiency are proposed. With their CMOS compatibility and capability of monolithic integration on Si, the GeSn-based LED devices are considered as the robust alternatives to the III-V materials for mid-IR light sources integrated on Si.

4.2 GeSn homojunctions

With the understanding of the GeSn bulk structure growth characteristics, the GeSn active region directly grown on Ge buffer are limited on several aspects: a) large compressive strain, leading to the small or negative difference between the L and Γ valley minimum; b) the large lattice mismatch made it difficult to increase the Sn composition in the active region. Considering these limitations, the LED main factor is the GeSn quality within the active region. In such case, the compressive strain can be minimized by growing an SRE bulk GeSn using a homojunction structure. The GeSn total thickness can be increased so that the higher Sn can be incorporated into the active region while maintaining low compressive strain.

In this work, the GeSn was grown using similar method described in last section. The p-type doped Ge buffer layer was grown on Si substrate with a nominal thickness of 1000 nm. The intrinsic GeSn was grown with a thickness of 400 nm. SRE GeSn growth technique was applied to achieve a 11% Sn incorporation in this layer. A 150 nm n-type GeSn layer was grown as quasi neutral region with doping level of 1×10^{18} cm^{-3}. A 50 nm Ge cap layer was added with heavily doping level (1×10^{18} cm^{-3}). The cap layer kept the Sn composition same as the active region. SIMS was used to check the thickness, Sn composition, and doping level, as plotted in Fig. 47. The profile of Sn composition is increasing with a higher slope closed to Ge buffer and a steady Sn composition at surface. The decrease of Sn composition slope is a clear indication of the strain relaxation. The sample was measured using TEM to check the material quality and cross-check the thickness, shown in Fig. 48. The first 300 nm on the Ge buffer shows a high density of threading dislocation, which further confirms the relaxation. This relaxation mechanism is similar to the bulk GeSn growth for the optically pumped laser.

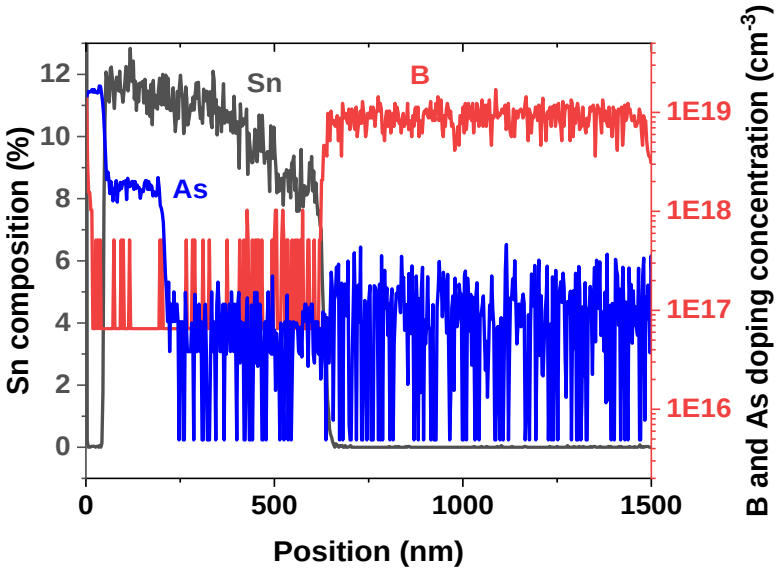

Figure 47. SIMS profile of the GeSn homojunction LED.

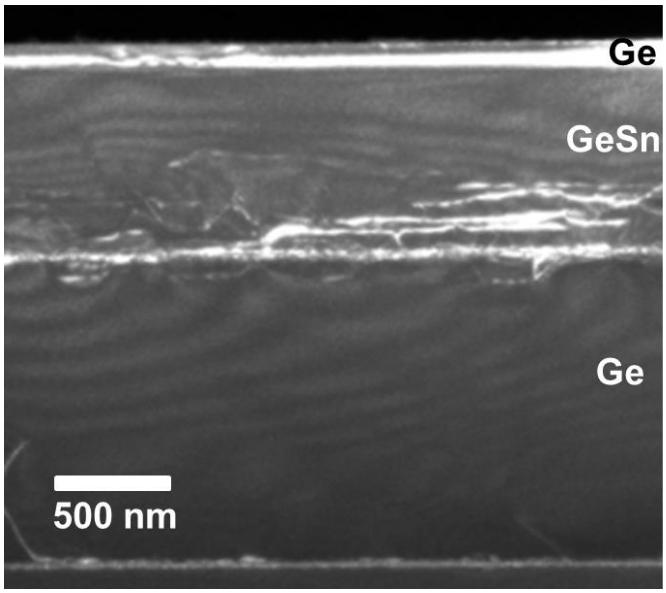

Figure 48. TEM of the GeSn homojunction.

The surface emitting LED was fabricated. The square mesa (500 μm□500 μm) was defined by chemical wet etching. The Ge buffer was exposed as p-type contact. Electron-beam evaporator was used to deposit the electrodes, including a first 10 nm Cr and a second 350 nm Au. Figure 49 depicts the cross-sectional schematic diagram of the surface emitting LED. The LED was diced and wire-bonded onto a silicon carrier chip with insulated metal contacts. The emission was collected from the surface by using a CaF_2 lens. The edge emitting LEDs was fabricated with a ridge waveguide structure with area of 80 μm × 1.5 mm. The ridge was etched same height as surface emitting LED. The device was cleaved and bonded onto the Si carrier chip. The emission was collected from a single facet of the ridge. The device emission properties were measured under pulse condition using the method described in previous section. The temperature dependent L-I and spectra was measured by using a spectrometer and a thermal-electrical cooled PbS detector.

The I-V of the surface emitting LED was measured, a clear rectify behavior can be

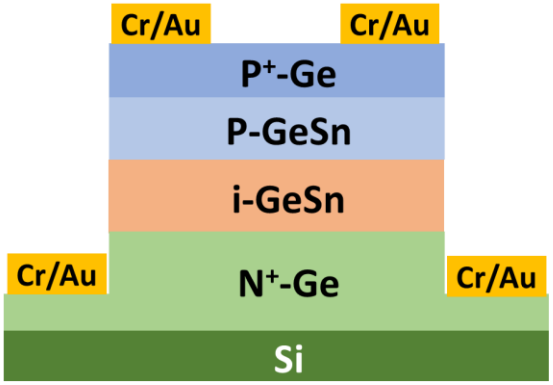

Figure 49. Schematic diagram of the fabricated surface emitting LED.

observed and a reverse current density of 1.1 A/cm^2 was measured at -1V bias. The series resistance was extracted as 0.11 Ω. The emission spectra from surface emitting LED were plotted in Fig. 50(b). The emission peak wavelength is measured at 2300 nm, agreed with the theoretical calculation of the bandgap of $Ge_{0.89}Sn_{0.11}$. As the temperature decrease from 300 to 77 K, the peak wavelength position shifts towards higher energy and the peak intensity becomes ~15× stronger. The injection dependent integrated EL intensity was measured at temperatures from 77 to 300 K. The current dependent EL intensity has a linear dependent at low current density and become saturate above the 400 A/cm^2. At injection above 350 A/cm^2, the emission intensity increases from 150 to 300 K.

The emission characteristics from edge-emitting LED were presented in Fig. 51. The behavior in general is the same as surface emitting LED except the lower intensity due to the smaller emission window area. At 77 K, emission intensity starts saturated at 180 A/cm^2. The reverse biased current density at -1V is about one order of magnitude smaller than that of the Ge/GeSn/Ge. The reduced reverse bias current density is a major sign of reduced trap density within the bandgap of the active region, showing a relatively improved material quality.

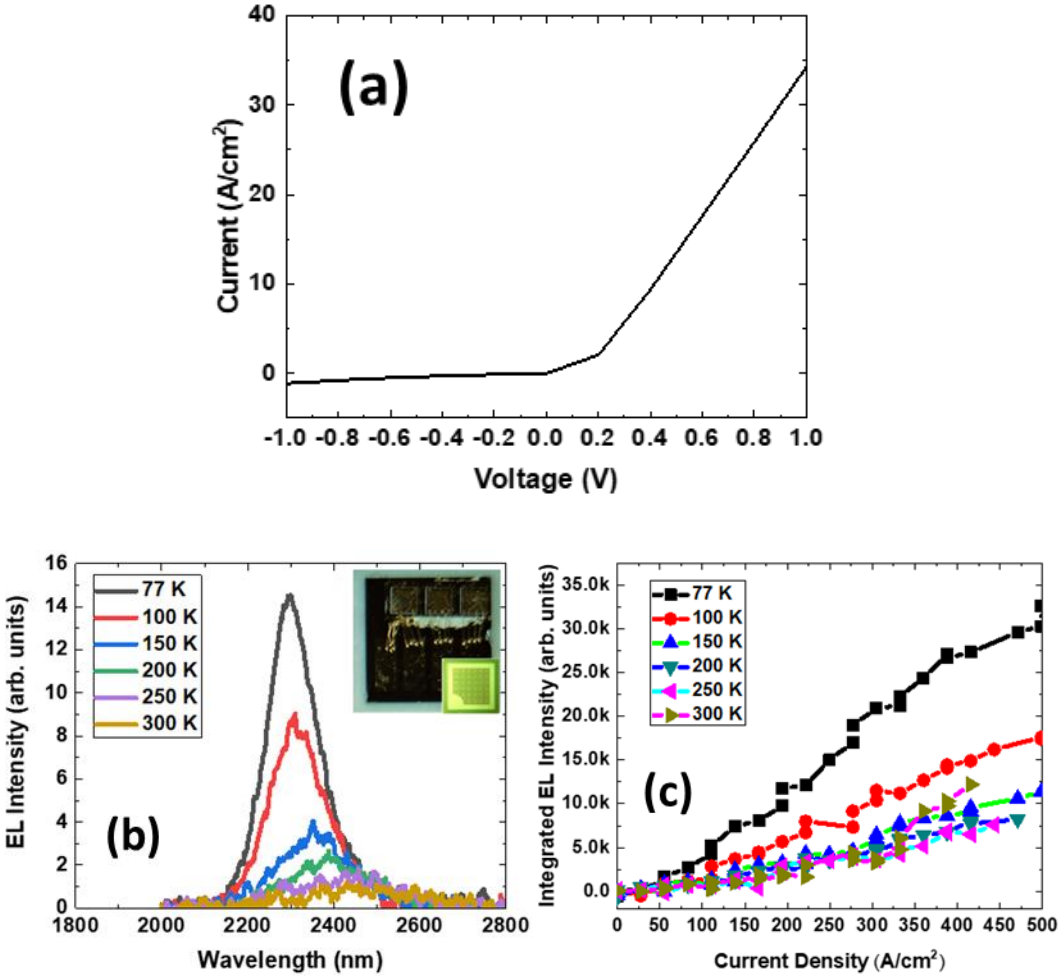

Figure 50. Surface emitting homojunction GeSn LED characteristics: (a) I-V at 300 K, (b) temperature dependent spectra measured at 300 A/cm^2, inset: optical image of the bonded device; and (c) temperature dependent L-I curve.

The emission characteristics agree to the behaviors from the PL of the direct bandgap GeSn. The emission spectra can be clearly identified with an improved signal to noise ratio, compared to the noisy spectra from the Ge/GeSn/Ge LEDs in last section.

The increase of intensity at higher temperature at high injection can be explained by the effect of radiative recombination through the indirect bandgap transition. At higher temperature, carriers interact with photons more frequently enabling the indirect transition. And the indirect transition has a significantly lower efficiency than the direct transition, so it can be observed at

sufficient injection level. The emerge of indirect transition was an evidence of the close energy alignment between the Γ and L valley.

The intensity saturation at high injection level is a sign of decreased of quantum efficiency of LED. This is partially caused by the homojunction design, where the carriers are little confined within the active region. This leads to the question that how to introduce the proper heterostructure for GeSn LEDs.

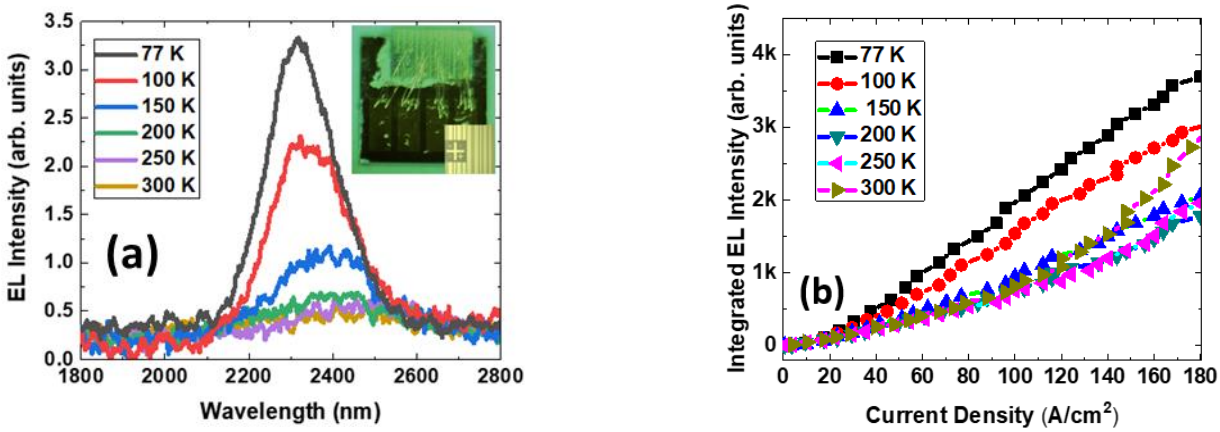

Figure 51. Edge emitting homojunction GeSn LED characteristics: (a) temperature dependent spectra, inset: optical image of the bonded device measured at 180 A/cm2; and (b) temperature dependent L-I curve.

4.3 GeSn/GeSn/(Si)GeSn double heterostructures

In previous sections, Sn composition was increased up to 11 % with a relatively thick (~400 nm) active region. The GeSn active layer has relatively low compressive strain thanks to the SRE growth technique. However, in a homojunction design, the density of state in the active region is relatively low, which is a result of missing carrier confinement. In this section, direct bandgap GeSn EL was measured from GeSn heterostructure LEDs. Two samples were studied with the comparison of using SiGeSn and GeSn as top barrier layer. The two materials used in the barrier both have reduced strain level comparing to Ge. The sample with SiGeSn barrier

showed a reduced leakage current and enhanced EL intensity.

The DHS structures were grown on Si by using ASM Epsilon® 2000 Plus RPCVD reactor. The first structure growth sequence involves: (1) a 900-nm-thick n-type doped Ge buffer layer; (2) a 400-nm-thick n-type doped GeSn buffer layer (Sn composition gradient from 8 to 11%); (3) a 600-nm-thick intrinsic $Ge_{0.89}Sn_{0.11}$ layer; (4) a 50-nm-thick p-type doped $Si_{0.03}Ge_{0.89}Sn_{0.08}$ barrier-I layer; and (5) a 50-nm-thick p-type doped $Si_{0.03}Ge_{0.89}Sn_{0.08}$ barrier-II layer. The doping concentrations for n-type Ge and GeSn buffer layers were 1×10^{19} cm^{-3}. The doping concentrations for barrier-I and -II layers were designed as 1×10^{18} and 1×10^{19} cm^{-3}, respectively. The second structure replaced the $Si_{0.03}Ge_{0.89}Sn_{0.08}$ by $Ge_{0.95}Sn_{0.05}$ in barrier-I and -II layers while keep other layers unchanged. The doping level and the thickness remain the same. The two samples were fabricated into squared mesa LEDs with side length of 500 μm. The chemical wet etching was used to form the mesa. Electron-beam evaporator was used to deposit 10-nm-thick Cr and 350-nm-thick Au for electrodes. The device schematic and optical image were illustrated in inset of Fig. 52. The current voltage (IV) characteristics measurement was performed by using a DC source measurement unit. The light emission from the surface was directly coupled to the spectrometer through CaF_2 lenses. The temperature dependent spectra were measured under DC injection. The PbS detector, covering wavelength range from 1 to 3 μm, was used to collect the emission signal. The current dependent EL measurement was taken under pulsed condition to eliminate the local heating particularly at high injection levels. The pulse source was set with 0.5% duty cycle and 171 Hz repetition rate, respectively.

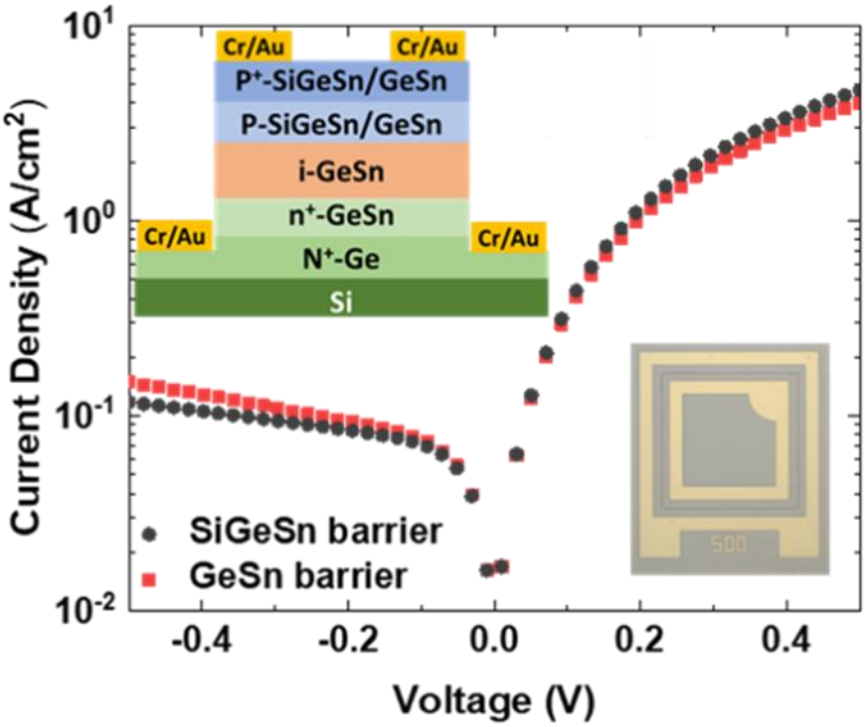

Figure 52. IV characteristics of the LED devices at room temperature, inset: schematic cross-sectional structure diagram (top left) and optical image (bottom right).

The barrier heights between the active and barrier layer in the conduction band were calculated as 91 and 56 meV for SiGeSn and GeSn barrier, respectively. Both SiGeSn and GeSn barrier have reduced strain level (0.64% and 1.02%, respectively), compared to 1.9% if Ge barrier was used. The room temperature IV characteristics was shown in Fig. 52. The series resistance was measured as 0.09 and 0,07 Ω for SiGeSn and GeSn barrier samples, respectively. The SiGeSn barrier sample showed a lower leakage current at reverse bias than GeSn barrier sample.

The EL spectra at 77 K were compared from two samples, shown in Fig. 53. The peak intensity from SiGeSn barrier sample is four times higher than the GeSn barrier sample, due to the improved carrier confinement. The temperature dependent EL spectra were collected from 77 to 300 K, shown in Fig. 54 and 55. The emission peak shift towards the lower energy as the

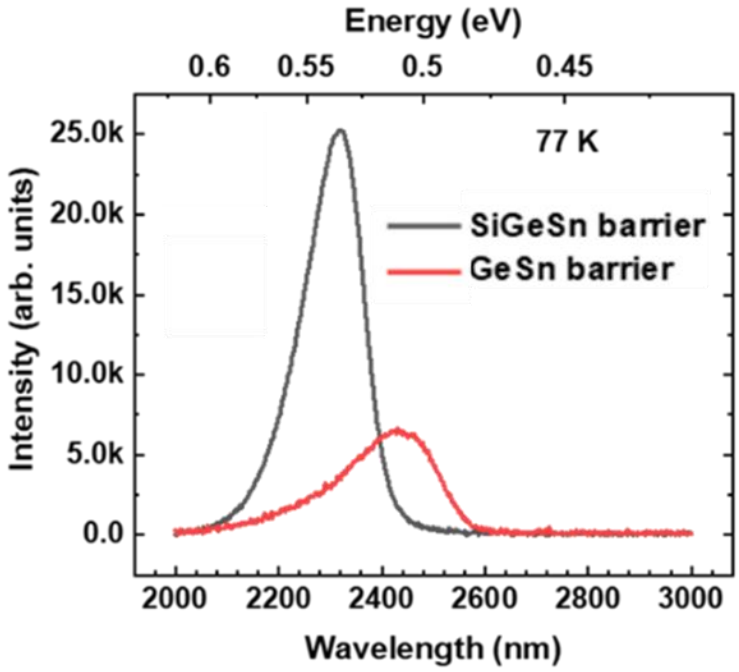

Figure 53. EL from two samples under 160 A/cm2 current injection at 77 K.

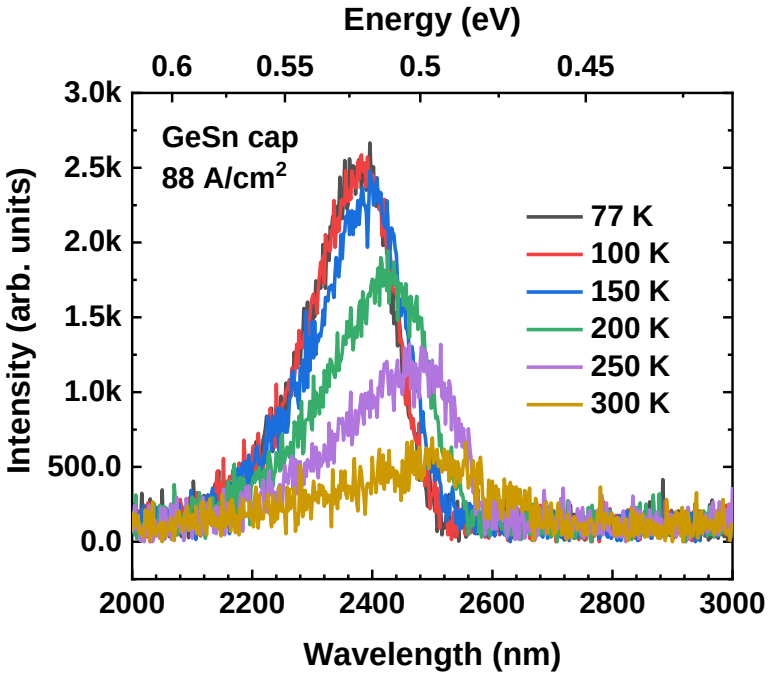

Figure 54. Temperature-dependent EL spectra of the GeSn barrier LED under 88 A/cm2 current injection, DC biased.

temperature increased. The transitions followed the Varshni's empirical relation on the

temperature dependency of the bandgap. The EL emission output vs. current was studied at 77 K under the pulse condition. The low duty cycle eliminated the thermal heating, confirmed by the no shift of the emission peaks at each current measured. The EL intensity against current injection was plotted in Fig. 56, showing a superliner dependency.

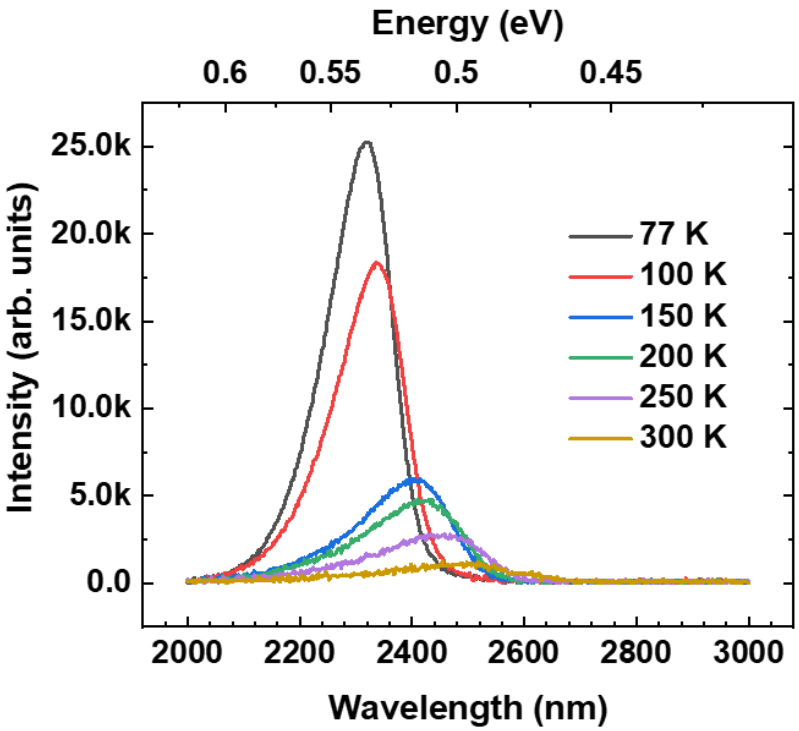

Figure 55. Temperature-dependent EL spectra of the SiGeSn barrier LED under 160 A/cm2 current injection, DC biased.

Figure 57 compares the emission spectra from the SiGeSn and GeSn capped LEDs and the GeSn homojunction LED in last section. A clear emission intensity increase was observed, showing the present of carrier confinement would increase the emission efficiency.

In the DHS LED design, the GeSn was grown by using SRE method. The Sn composition gradually increases along the growth direction. This Sn gradient naturally forms the energy cladding, where energy gap decreases along the growth direction. The large gradient region (GeSn buffer) serves as the bottom barrier layer. Further growing the GeSn lead to a

relaxation of GeSn and the Sn composition gradient ease. This small gradient layer is used as the active region where defect density is minimized. The GeSn (or SiGeSn) cap layer are selected with a larger bandgap with a lower Sn composition. The DHS is therefore formed with GeSn/GeSn/(Si)GeSn structure.

Two GeSn DHS LED samples with were characterized to evaluate barrier materials using SiGeSn and GeSn. The barrier heights in the conduction band for SiGeSn and GeSn barrier were calculated as 91 and 56 meV, respectively. Lower leakage current and high emission intensity was observed in SiGeSn barrier sample, compared to GeSn barrier sample. The results provide a feasible SiGeSn/GeSn heterostructure design to enhance carrier confinement in the GeSn light emitters for future mid-infrared sensing applications.

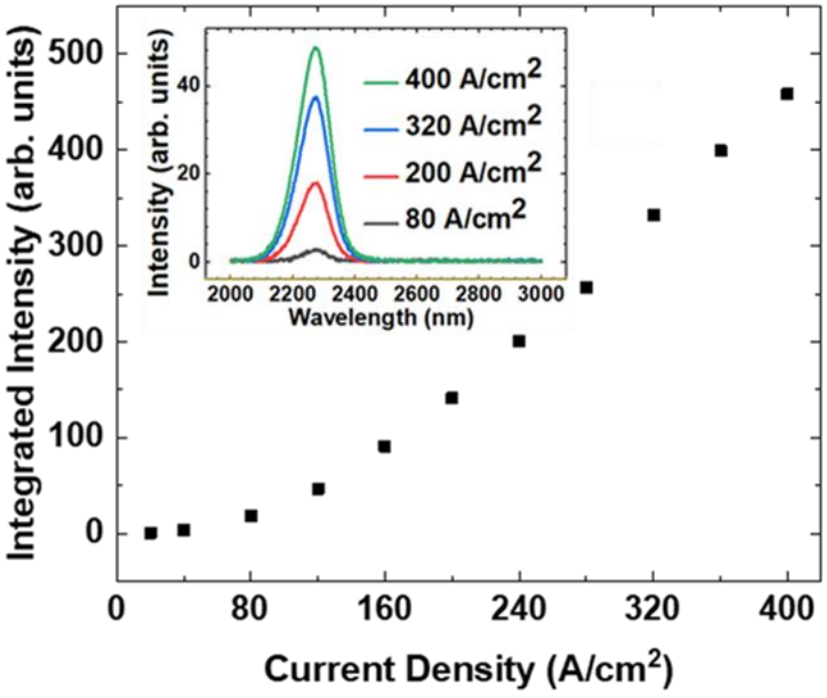

Figure 56. Integrated EL intensity under various current injection at 77 K under the pulsed current injection. Inset EL spectra under various current injections.

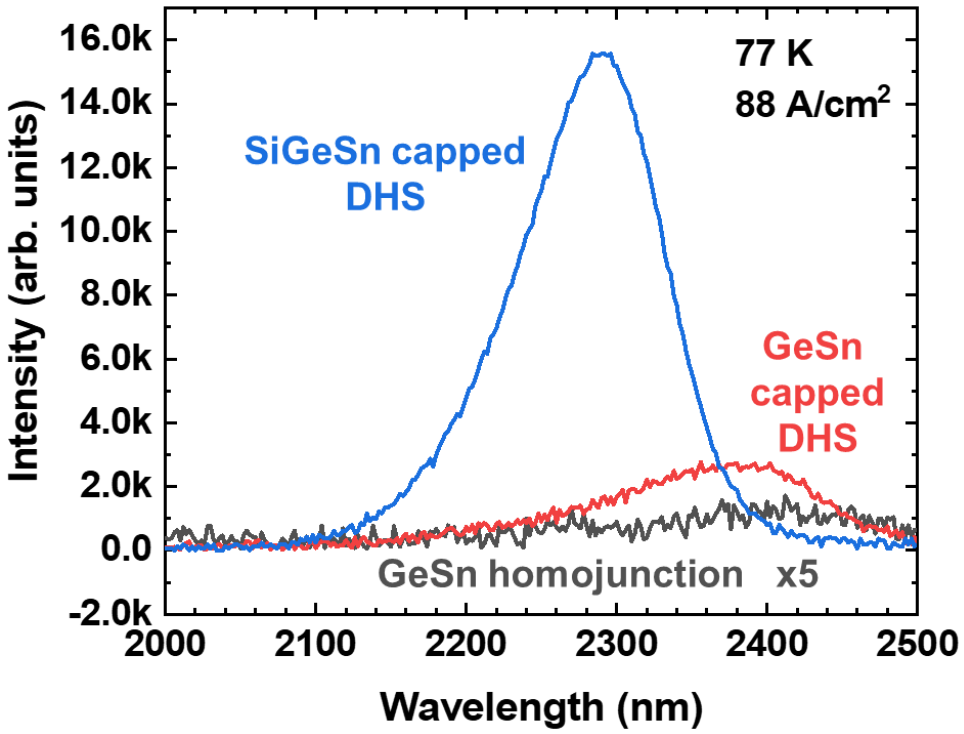

Figure 57. The emission spectra from the GeSn homojunction (in last section) and DHS (in this section) at 77 K under 80 A/cm^2.

Chapter 5: Electrically injected GeSn laser diodes

5.1 Demonstration lasing through electrically injection

In this section, the first electrically injected GeSn diode lasers were demonstrated. The GeSn/SiGeSn double-heterostructure was grown which ensures the carrier-and-optical confinement. To address the hole leakage due to a type-II band alignment between GeSn and the top SiGeSn barrier, the p-type top SiGeSn layer was designed to facilitate the hole injection. The ridge waveguide GeSn lasers were fabricated and pulsed lasing was observed up to 100 K. The threshold was measured at 598 A/cm^2 at 10 K. The characteristic temperature T_0 was extracted from 76 to 99 K at the temperature range of 10 to 77 K for different devices.

The laser diode structure was grown via an industry-standard CVD reactor using commercially available precursors on a 200-mm (100) Si substrate. Five epitaxial layers were grown from bottom to top: i) a nominal 500-nm-thick strain-relaxed Ge buffer layer, with n-type doping of 1×10^{19} cm^{-3}; ii) a 700-nm-thick GeSn buffer layer using the spontaneous relaxation enhanced growth method [44], with nominal Sn composition from 8% (bottom) to 11% (top), and n-type doping of 1×10^{19} cm^{-3}; iii) a nominally intrinsic 1000-nm-thick $Ge_{0.89}Sn_{0.11}$ active layer; iv) a 170-nm $Si_{0.03}Ge_{0.89}Sn_{0.08}$ cap layer with p-type doping of 1×10^{18} cm^{-3}; and v) a 70-nm $Si_{0.03}Ge_{0.89}Sn_{0.08}$ Ohmic contact layer with p-type doping of 1×10^{19} cm^{-3}. All doping growth was done in-situ by introducing corresponding doping gases. The cross-sectional schematic of the laser device is shown in Fig. 58(a). The compositions of Sn and the layer thickness were measured by XRD and TEM.

The TEM image in Fig. 59 provides thickness and crystalline information for each layer. The GeSn buffer remains a considerable density of threading dislocations. The GeSn buffer is

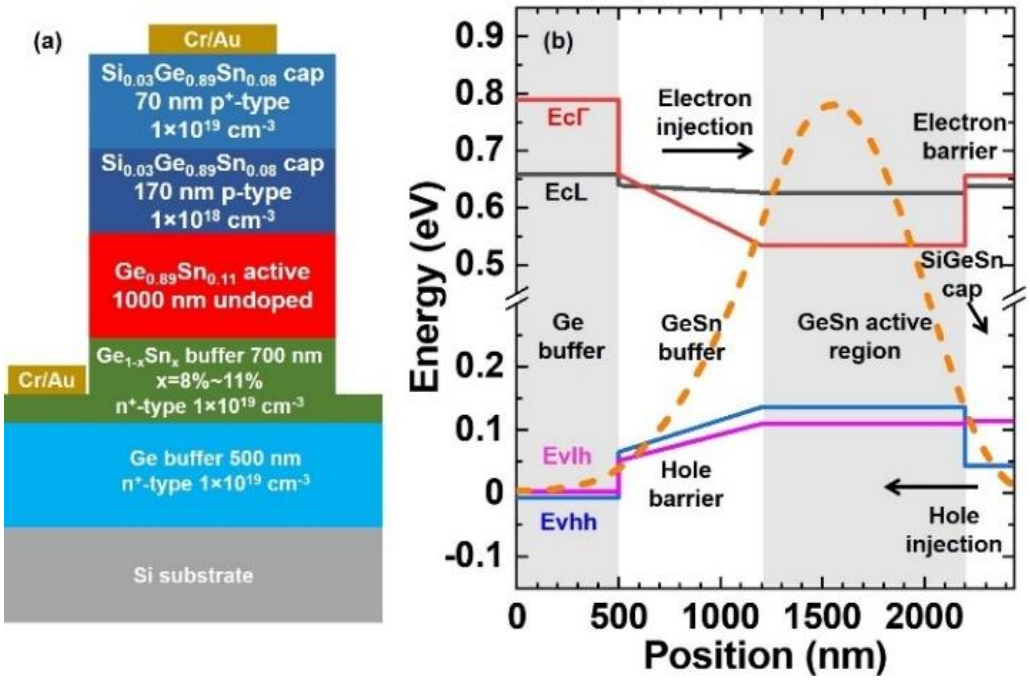

Figure 58. (a) Cross-sectional schematic of laser device; (b) Calculations of band structure and profile of fundamental TE mode. Band structure shows type II alignment between GeSn active and SiGeSn cap layers at LH band. Mode profile shows 75% of the of the optical field overlapped with the GeSn active region. Reprinted with permission from [77] © The Optical Society.

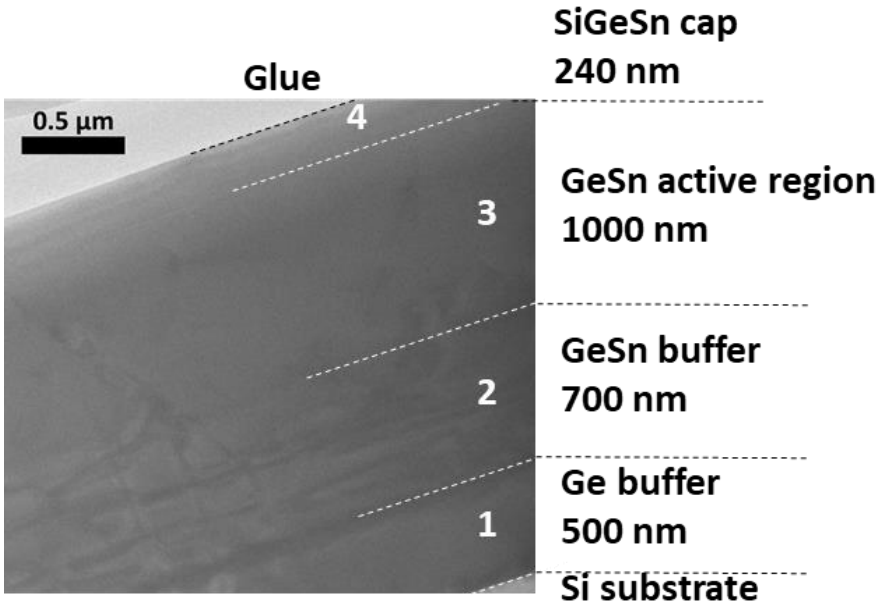

Figure 59. TEM imaging shows thickness and crystalline details of the structure. Reprinted with permission from [77] © The Optical Society.

aimed to release the compressive strain and increase the Sn content in the upper GeSn active region. From the TEM image, the GeSn active region has a much lower dislocation density compared to the GeSn buffer.

The XRD RSM showed the profile of crystalline strain information, as shown in Fig. 60. Three peaks (labeled as 1, 2, and 3) can be identified. Peak 1 is the Ge buffer peak. The peak 2 covers a broad range and connects to peak 3, which is a sign of changing lattice strain. It is mainly from the GeSn buffer. The peak 3 represents the GeSn active region. The GeSn active region peak has the highest intensity, with a small degree of residual compressive strain. Detailed GeSn bulk growth mechanism is explained in Ref 44. The SiGeSn peak cannot be clearly identified. Based on the calculation, the SiGeSn layer is expected to have a tensile strain and the in-plane lattice constant (a//) closed to that of the GeSn active region. The corresponding position is expected to be near peak 2 and below the R = 1 line. Another possibility is that the GeSn buffer and SiGeSn buffer peaks overlap and form the "peak 2". Table SI summarizes the Sn composition and strain extracted from the XRD RSM measurement.

After the growth, the sample was fabricated into ridge waveguide laser structures and then cleaved into individual devices with the cavity lengths of 0.3, 0.5, 0.8, and 1.7 mm. The 80-μm-wide ridges were formed by wet etching. The etching depth was controlled at 1.4 μm to expose the GeSn buffer layer for metal contacts. Electron beam evaporated Cr and Au were deposited as both p and n electrodes through a lift-off process with the thickness of 10 and 350 nm, respectively. The Si substrate was lapped down to 140 μm thick, followed by cleaving to form the Fabry-Perot cavity. Finally, the devices were wire-bonded to a Si chip carrier and mounted in a cryostat for low-temperature measurements.

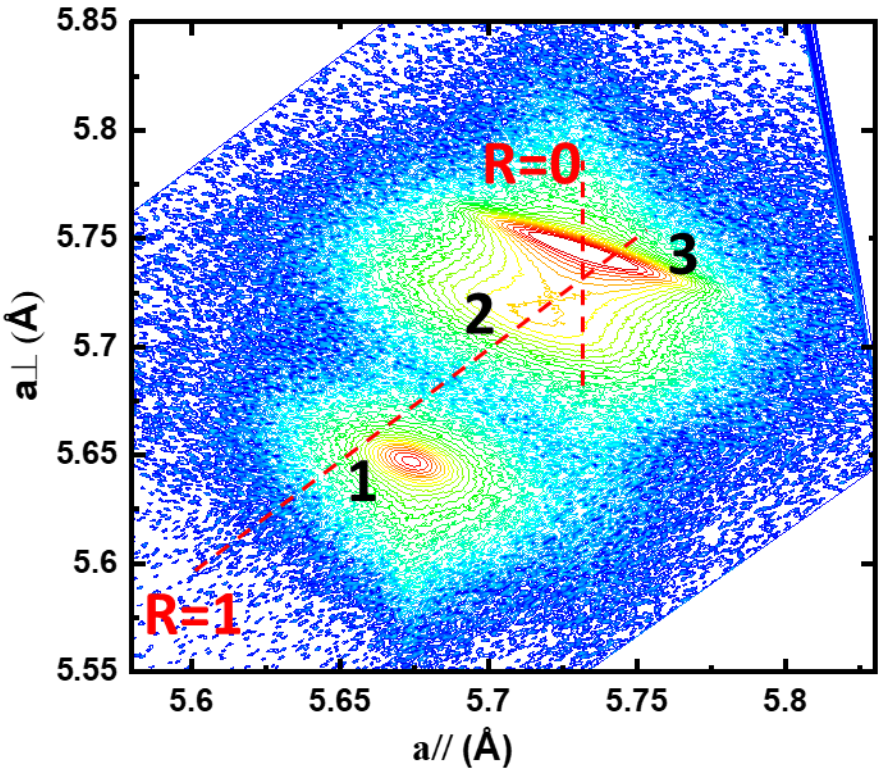

Figure 60. XRD RSM map showing the lattice information from the structure. Dashed lines labeled in R = 0 and R = 1 represent the relaxation levels for 0 and 100% relaxation, respectively. Reprinted with permission from [77] © The Optical Society.

The current-voltage (IV) measurement was performed using a direct current source measurement unit. For the pulsed measurement, a pulsed high compliance voltage source was used to drive the laser and the current was monitored by a calibrated magnetically coupled current meter. The repetition rate of 1 kHz and pulse width of 700 ns were used for the spectra and light output vs. injection current (LI) measurements. The EL and PL emission signal was collected and analyzed through a monochromator (10 nm resolution) and liquid-nitrogen-cooled-InSb detector (response range 1 - 5.5 μm). The high-resolution spectra were obtained by using a Fourier-transform infrared spectroscopy (FTIR) instrument equipped with the InSb detector. Step-scan mode was used with a 0.25 cm^{-1} resolution for the measurement.

The device band edge diagram at 300 K was calculated based method described in Ref.

78 and plotted in Fig. 58(b). Four sub-bands including indirect L (E_{cL}) and direct Γ ($E_{c\Gamma}$) valleys in the conduction band (CB) and heavy hole (E_{vhh}) and light hole (E_{vlh}) in the valence band (VB) were considered. The following features are obtained from Fig. 58(b): i) $Ge_{0.89}Sn_{0.11}$ active layer has a direct bandgap with the energy difference of 92 meV between L and Γ valleys. The high degree of relaxation in this layer results in the small difference between HH and LH band; ii) In the CB, both Γ and L valleys feature type-I alignment due to the wider bandgap energies of $Si_{0.03}Ge_{0.89}Sn_{0.08}$ cap and GeSn buffer. Note that the Sn composition increases in the GeSn buffer (8%~11%) along the growth direction, leading to the decrease of both Γ and L valleys in energy with the Γ more rapidly than the L valley; iii) In the VB, the HH band features type-I band alignment. The LH exhibits type-II band alignment at the cap/active layer interface, due to the tensile strain within the $Si_{0.03}Ge_{0.89}Sn_{0.08}$ cap.

The fundamental TE mode was plotted (dashed curve) to show the optical field distribution. The refractive index for each layer was taken from the previous study [63]. The optical confinement factor (optical field confined in $Ge_{0.89}Sn_{0.11}$ active region) was calculated as 75% using the wavelength at 2.3 μm.

The typical pulsed LI curves from the 0.8-mm cavity length device were plotted in Fig. 61(a) at temperatures from 10 to 100 K (maximum lasing temperature). The threshold current densities are measured as 0.74 and 3.9 kA/cm^2 at 10 and 100 K, respectively. At 10 K, the emission shows a saturation feature at 7.5 kA/cm^2. The maximum peak power was measured as 2.7 mW/facet.

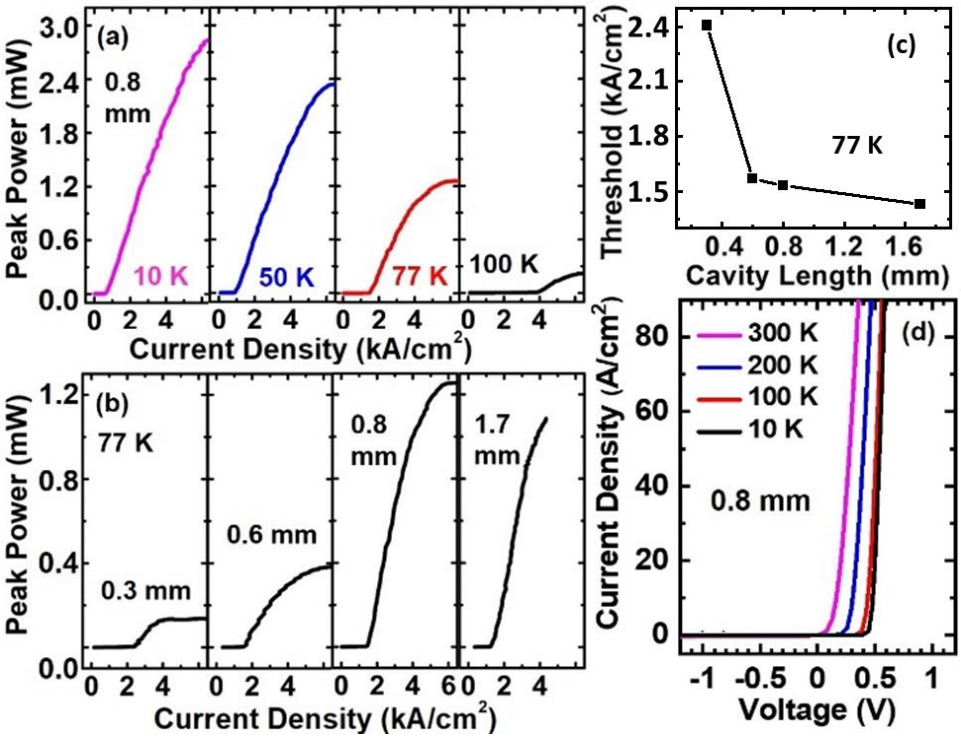

Figure 61. (a) LI curves of the 0.8-mm cavity length device from 10 to 100 K; (b) LI curves at 77 K for four devices with different cavity lengths; (c) Threshold of each device at 77 K; (d) Temperature-dependent IV of the 0.8-mm cavity length device. Reprinted with permission from [77] © The Optical Society.

The LI characteristics of devices with different cavity lengths were studied, as shown in Fig. 61 (b) at 77 K. The threshold current densities were measured as 2.4, 1.6, 1.5, and 1.4 kA/cm^2 for devices with cavity lengths of 0.3, 0.6, 0.8, and 1.7 mm, respectively, as shown in Fig. 61 (c). As cavity length (L) increases, the decreased lasing threshold is mainly due to the reduced mirror loss ($\propto 1/L$). The 1.7-mm device has the lowest threshold among four devices, with the value of 598 A/cm^2 at 10 K. The temperature-dependent thresholds for all four devices were extracted and summarized. Moreover, the saturated emission intensity increases as L increases, except for the 1.7-mm device (no higher current could be applied due to device damage).

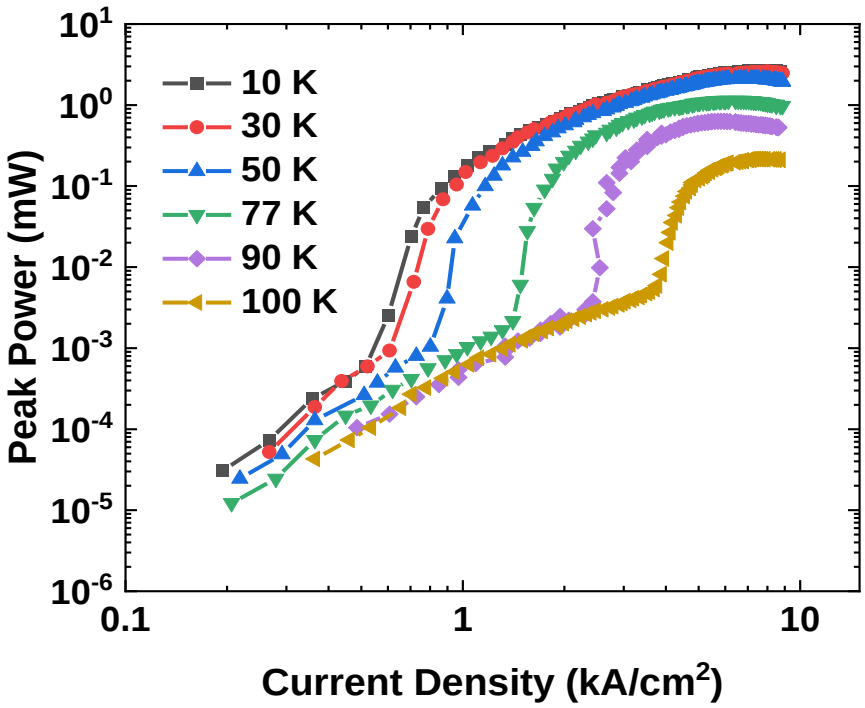

Figure 62. L-I curves of the 0.8 mm cavity length device from 10 to 100 K. Reprinted with permission from [77] © The Optical Society.

The L-I curves in Fig. 61(a) are re-plotted in a log-log scale in Fig. 62. Three regions with distinct slope values can be identified as the current injection increased at all temperatures. The emission intensity is significantly increased above the threshold with about two orders of magnitude enhancement.

The threshold current densities are plotted against the cavity length at each operating temperature, shown in Fig. 63. The threshold current values are summarized in Table 11 at measured temperatures.

Figure 64(b), (c), and (d) show the emission spectra of the 1.7-mm cavity length device at 10, 77, and 100 K, respectively. At each temperature, as the injection current density increases from below to above the threshold, the significantly increased peak intensity and reduced FWHM were observed, both being the evidence of the lasing characteristic.

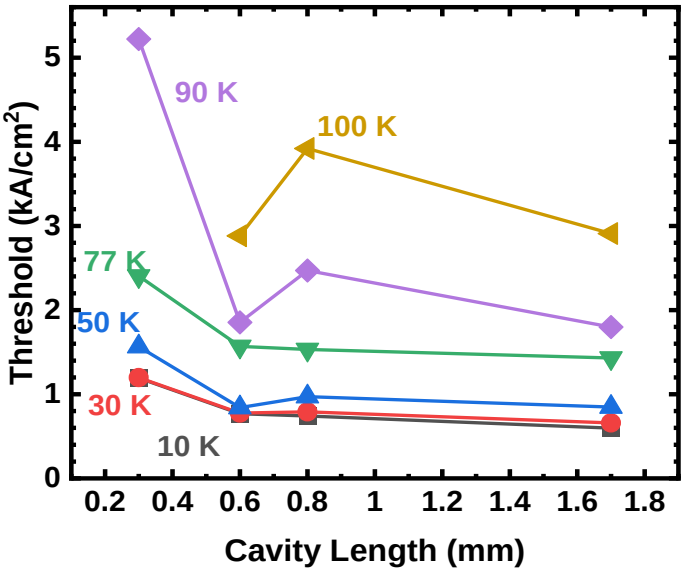

Figure 63. Threshold current density as a function of cavity length at each operating temperature. Reprinted with permission from [77] © The Optical Society.

At 10 K, the measured peak position is the same as for the 0.3-mm device, i.e., at 2250 nm. At 100 K, the lasing peak redshifts to 2300 nm as expected due to the narrowed bandgap. The log-scale plot of Fig. 64(d) is shown in (e). Above the threshold, the stimulated emission peak stands out from the broad spontaneous emission.

Generally speaking, the longer cavity length device features decreased mirror loss, and therefore it should outperform the short cavity length devices in terms of the lasing threshold. This trend can be observed from the extracted thresholds of four devices. Note that 0.6-mm and 0.8-mm devices show a few deviated data points. This can be explained by the additional optical loss mechanism other than mirror loss, which includes: (1) interface defects induced the mid-gap states, where photon absorptions could occur and lead to optical loss; (2) the surface roughness induced scattering loss; (3) the optical loss occurs at the semiconductor/metal interface, and the metal surface roughness also induces additional loss; and (4) FCA. Therefore, the device

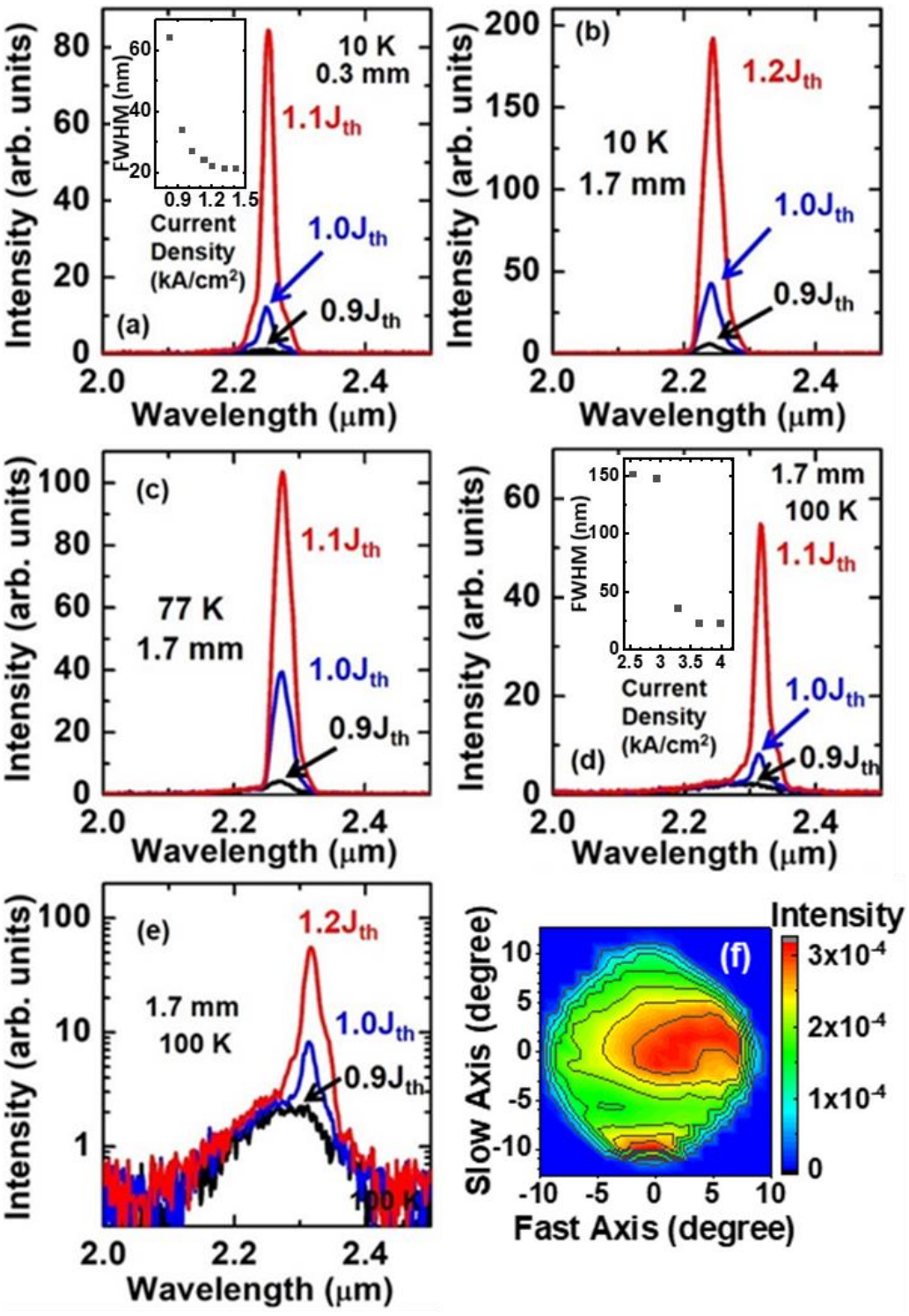

Figure 64. Emission spectra at various current injection levels. (a) 0.3-mm device at 10 K. Inset: extracted FWHM vs. current density (spectral resolution of 10 nm); (b), (c), and (d) 1.7-mm device at 10 K, 77 K, and 100 K. Inset in (d): extracted FWHM vs. current density; (e) log-scale plot of spectra in (d); (f) far field pattern from 1.7-mm device at 77 K. Reprinted with permission from [77] © The Optical Society.

performance may show some variations just like the 0.6-mm and 0.8-mm devices in this work. It is very difficult to quantitatively identify the loss contributed by each mechanism.

The typical IV characteristics of the 0.8-mm cavity length device were measured at various temperatures as plotted in Fig. 61(d). The series resistance is extracted as 1.2 Ω at 10 K. The IV characteristics are consistent with the previous GeSn diode studies [72,79], where the detailed IV analysis was reported. Under the pulsed current operation, low duty cycle and short pulse width were chosen to minimize the joule heating.

The emission spectra below and above threshold were investigated. Figure 64(a) shows the spectra of the 0.3-mm cavity length device under various current injection levels at 10 K. Below the threshold, the peak full-width half max (FWHM) was 64 nm, while above the threshold the FWHM became ~20 nm, as shown in Fig. 64 (a) inset. Note that the relative broad peak linewidth of 20 nm is due to the spectral resolution of 10 nm. At 10 K, the lasing emission peak was observed at 2250 nm.

Table 11. Threshold current density (in A/cm^2) for the laser diodes studied at each temperature. Reprinted with permission from [77] © The Optical Society.

	0.3 mm	0.6 mm	0.8 mm	1.7 mm
10 K	1193	769	741	598
30 K	1198	776	790	659
50 K	1565	842	972	848
77 K	2406	1569	1533	1431
90 K	5221	1854	2470	1799
100 K	NA	2882	3920	2910

The far-field pattern was measured at the cross-section plane 4 cm away from the laser facet. Two major peaks were observed, indicating multi-mode operation, as shown in Fig. 64(f). The FWHMs of the major peak at the center are estimated around 16 and 12 degrees along the fast and slow axis, respectively.

The 10 nm resolution setting for spectrometer comprised the resolution to obtain the spontaneous emission with reasonably signal to noise ratio. The spectra were measured from the 0.3-mm cavity length device using a spectrometer setup with the slit width set to ~1 nm minimum resolution. Under the current density of 6 kA/cm^2, a multi-mode spectrum was observed. Although the resolution is not enough to resolve the full shape of individual peaks, the longitudinal mode peaks that appeared from the spectra could still be identified and labeled in Fig. 65. The peaks positions of longitudinal modes at around 2300 nm were plotted in the inset. The free spectral range of the f-p cavity follows the relation $\Delta\nu_{FSR} = c/n_gL$, where the $\Delta\nu_{FSR}$ is the frequency spacing between each mode, n_g is the group index, and L is the cavity length. The spacing between two adjacent longitudinal modes agreed with the calculated free spectral range of the Fabry-Perot cavity. The shoulder peaks closed to 2270 nm were observed. The two lasing regions (2270 and 2300 nm) are suspected from the extended gain bandwidth due to the Sn composition gradient within the GeSn layer.

To further study the lasing characteristic, high-resolution spectra were measured using a FTIR. Figure 66 shows the spectra of the 0.8-mm cavity length device at 77 K under various current injections. Above the threshold, the multi-mode lasing characteristic was clearly observed. The minimum FWHM of the individual peak is measured as 0.13 nm (or 0.06 meV). The dramatically reduced peak linewidth under higher injection is one of the lasing characteristics. At above 1.42 × threshold, the peak at 2307 nm dominates the lasing spectrum.

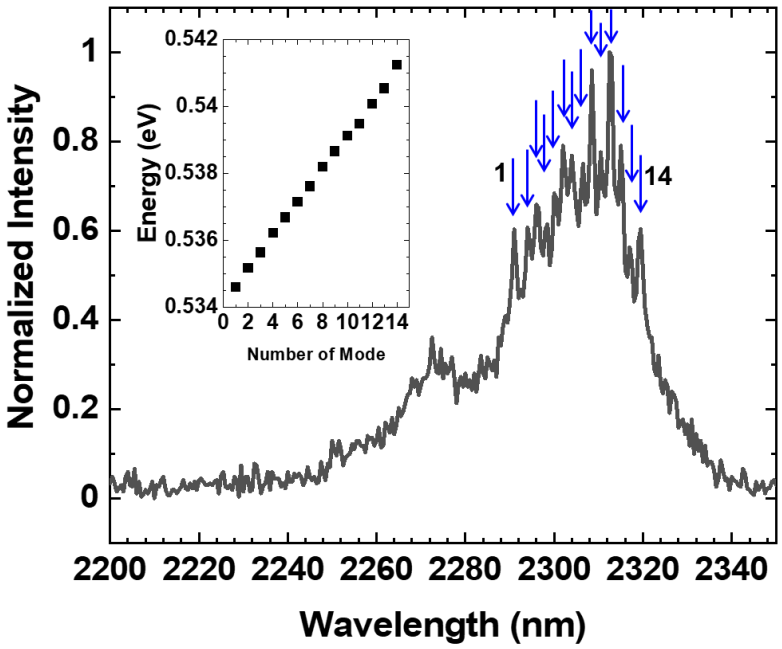

Figure 65. High-resolution spectrum was obtained from device with 0.3-mm cavity length at 77 K. Inset: longitudinal mode from the peaks labeled by the arrows. Reprinted with permission from [77] © The Optical Society.

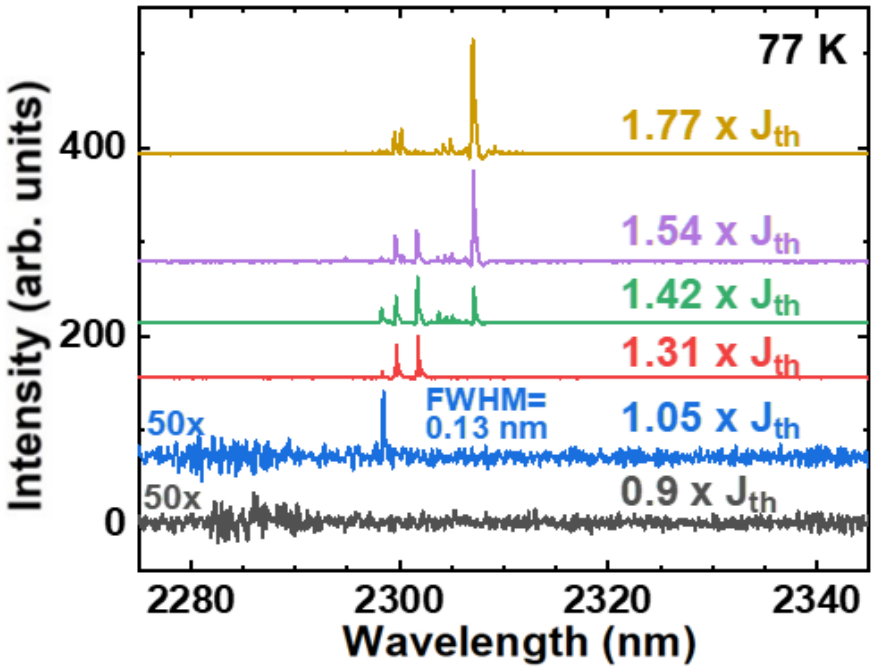

Figure 66. High-resolution spectra of 0.8-mm cavity length device at 77 K under various current injections. Reprinted with permission from [77] © The Optical Society.

The temperature-dependent threshold for each device was analyzed. The characteristic temperature T_0 was extracted using the empirical relation [80] $J_{th} = J_0 \exp(T/T_0)$, where J_{th} is the threshold current density, J_0 is a constant, T is the temperature. For each device, two regions, from 10 to 77 K and from 77 to 100 K can be clearly observed, as shown in Fig. 67 (except the 0.3-mm device whose maximum lasing temperature is 90 K). From 10 to 77 K, three devices (0.3, 0.6 and 0.8 mm) exhibited $\boldsymbol{T_0}$ above 90 K, while the 1.7-mm device showed $\boldsymbol{T_0}$ of 76 K. From 77 to 100 K, three devices show $\boldsymbol{T_0}$ values close to ~30 K, as a result of the significantly increased threshold.

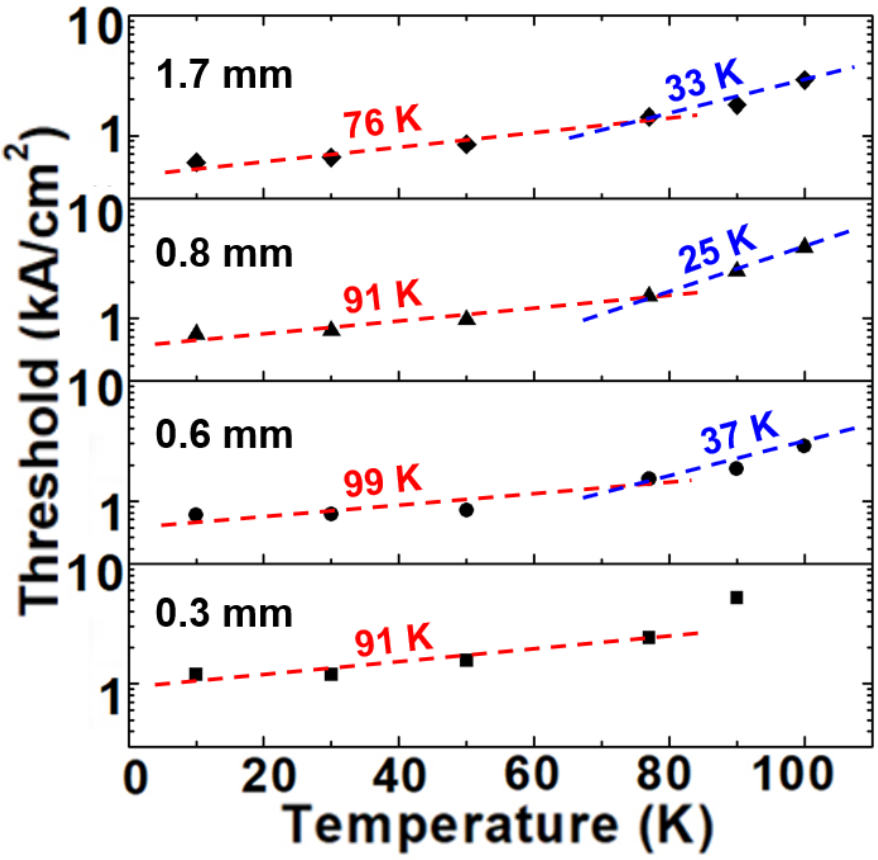

Figure 67. Extracted T_0 for each device. For the 0.3-mm device, the data point of threshold at 90 K was excluded from data fitting. Reprinted with permission from [77] © The Optical Society.

The 0.8 mm device exhibits the highest maximum peak power output at 2.7 mW (single facet) under 7 kA/cm^2 at 10 K. The external quantum efficiency of the 0.8 mm device is extracted at 0.3%. The maximum power conversion efficiency is measured at 0.03% at 1.5 kA/cm^2. Considering the ~0.55 V voltage drop on the junction and 1.77 V of total bias, the power conversion efficiency is ~0.1% for the junction.

In comparison with obtaining optically pumped lasers, there are special considerations for both carrier confinement and optical confinement in this work for the device structure design. In considering the carrier confinement in these laser devices, the result of the band structure calculation shown in Fig. 58(b) reveals that a type-II band alignment between the GeSn active and SiGeSn cap layers in LH at VB. The type-II alignment is originated from the tensile strain of the SiGeSn cap lifting the LH band above that in the GeSn active layer. As a result, the hole leakage at the top surface could lead to an increase in the lasing threshold. Therefore, this design is not ideal for optically pumped devices. However, for electrically injected devices, in order to address this poor hole-confinement issue, the top SiGeSn layer was intentionally doped as p-type in this work. As the holes are injected from the top SiGeSn cap layer, they are forced to flow to the GeSn active region. Since there are hole barriers in both HH and LH bands at VB between GeSn active and GeSn buffer layers, the holes could be confined in the active region to facilitate the population inversion. While the electrons are injected from the bottom GeSn buffer with the n-type contact, the electron barrier in Γ valley (lower band than L valley) in CB between the GeSn active and the top SiGeSn cap prevent the leakage of electrons and confine them in the active region. This p-i-n device structure design, rather than the n-i-p structure which may utilize the p-type unintentionally background doping of the GeSn buffer, effectively minimizes the hole leakage and enhances the carrier confinement. Similar asymmetric confinement structure design

can be found in early III-V double-heterostructure lasers [81,82].

In order to increase the optical confinement, it is necessary to address the small difference in the refractive index between Ge (4.03 at 2.3 μm) and GeSn (4.1~4.2 with different Sn %). To increase the mode overlap with the GeSn active layer, an overall 240-nm-thick SiGeSn cap layer was grown on top of the GeSn active layer, which pushes the peak intensity of the optical field into the active region, resulting in a 75% mode overlap with the GeSn core layer whose thickness is 1000 nm, as shown in Fig. 58(a). For optically pumped laser devices, the optical field can be well confined since there is nothing but the air above the cap layer. However, for the electrically injected laser devices, due to the metal contact above the cap layer, the thickness of the SiGeSn cap needs to be carefully optimized to minimize the optical loss via the metal thin film. The current thickness is selected as a compromise of the SiGeSn growth capability and the metal optical loss.

The lasing spectra were further examined with the PL study of the active region. PL was measured from the structure to compare with the EL, plotted in Fig. 68. Sample A is the original unprocessed sample with the SiGeSn cap remained. Sample B has the SiGeSn cap layer removed and GeSn active region is exposed at the surface. The EL spectrum was taken from the 0.8 mm cavity length device under 1.54x threshold at 77 K. Note that the 532 nm pumping laser was used to probe the bandgap from the top few tens of nanometer. PL from sample A as measured with a peak position at 2184 nm, corresponding to the emission of the SiGeSn cap. PL Peak position at 2390 nm was observed from sample B, corresponding to the light emission of the GeSn active layer. The lasing peak at 2300 nm features a clear blue shift, which can be attributed to the band filling effect. The lasing peak linewidth of ~ 23 nm is almost one order of magnitude narrower than the 163 nm and 205 nm linewidth for the PL from sample A and B,

respectively. In addition, the 23 nm linewidth is from the low-resolution peak, which is the envelope constructed by the multiple longitudinal mode peaks. Each individual peak features a sub-nanometer linewidth as shown in Fig. 66.

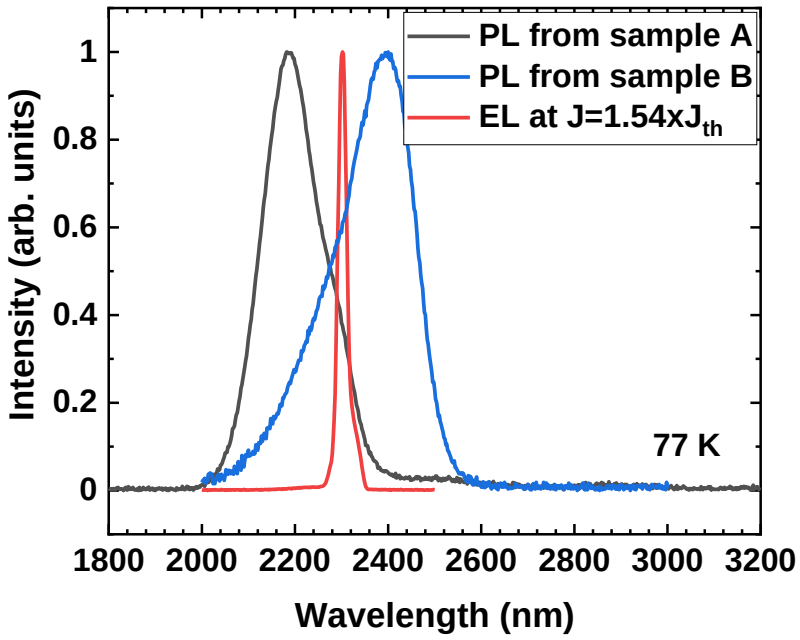

Figure 68. Comparison between PL and EL spectra at 77 K. Reprinted with permission from [77] © The Optical Society.

The lasing peak from the 0.8-mm cavity length device features a narrow linewidth (~23 nm) compared to that of the PL spectrum (205 nm). In addition, the 77 K high-resolution spectra in Fig. 66 reveals the details of the spectrum, where the multiple longitudinal peaks (with sub-nanometer individual peaks) form an envelope that shown as a single peak in the low-resolution measurement. The dramatic reduction of peak linewidth indicates the onset of lasing.

T_0 of ~90 K in the temperature range below 77 K is comparable with earlier reported III-V double heterostructure laser diodes [81,83]. As temperature increases above 77 K, the carriers in the GeSn active region could gain sufficient thermal energy to overcome the barriers and leak into the SiGeSn cap and GeSn buffer layers, resulting in significantly increased lasing threshold.

This leads to the considerably reduction of T_0 above 77 K, ranging from 25 to 37 K, as shown in Fig. 67. By optimizing the design of the cap and buffer layers, the improved carrier confinement at higher temperatures can be obtained and thus higher T_0 is expected.

Note that although 2.7 mW/facet peak power was obtained, the external quantum efficiency (EQE) was estimated as 0.3% (both facets power counted), which is relatively low even compared with early reported III-V double-heterostructure lasers [81]. This might be attributed to low injection efficiency due to the material band structure (close to indirect bandgap), current leakage due to poor carrier confinement, and the high internal optical loss. A thorough study will be the next step to quantitatively investigate the origin of low EQE.

To further improving the device performance, investigations of new structure designs are underway, which include: i) Increasing the Sn content to increase the bandgap directness so that injection efficiency can be increased; ii) Adding an SiGeSn buffer on the n layer to enhance the hole confinement; iii) improving material quality and fabrication technique to minimize the interface defects and surface roughness, so that internal optical loss can be reduced; and iv) reducing doping levels to minimize the FCA.

We have demonstrated electrically injected GeSn/SiGeSn heterostructure lasers that were grown on a Si wafer using a commercial CVD reactor. The narrow peak linewidth of 0.13 nm (0.06 eV) and L-I curve characteristics evidentially confirm the lasing. The multi-mode lasing characteristics were observed by high-resolution spectra. The lasing threshold of 598 A/cm^2 at 10 K was obtained. The maximum lasing temperature was measured as 100 K with 2300 nm peak wavelength. The p-i-n structure design enhances the carrier confinement by reducing the hole leakage through the type-II band aligned cap layer. The peak power was measured as 2.7 mW/facet at 10 K, corresponding to calculated EQE of ~0.3%.

5.2 Structure study of GeSn laser diode

In this work, several electrically injected GeSn heterostructure laser diodes with different cap layers and active layer material were compared. Increased cap thickness improves the optical confinement factor in the gain region and reduces the optical loss from the metal contact significantly. The devices with a thicker cap layer demonstrated reduced threshold, compared to the devices with a thinner cap. Cap layer materials with different conduction band barrier heights were also studied. The $Si_{0.03}Ge_{0.89}Sn_{0.08}$ capped devices with a 114 meV barrier exhibited a lower threshold and higher T_{max}, compared to the devices with $Ge_{0.95}Sn_{0.05}$ cap with a 58 meV barrier, which is due to the improvement on the electron confinement. Devices with 11% and 13% Sn composition in the GeSn active region are compared to probe the effect of intrinsic GeSn gain within the laser diode. Beyond the observation that lasing at a longer wavelength was recorded at 2682 nm at 90 K, the increase of Sn composition did not show improvement on threshold and T_{max}, implying that extrinsic structure property deteriorates the performance.

Layer structure of the laser diodes: The sample structures were grown on the 200-nm Si (100) wafer using RPCVD reactor. The five layers were epitaxially grown in the sequence of: (i) a 500 nm Ge buffer, n-type doped (phosphorus) at 1×10^{19} cm^{-3}; (ii) a 700 nm spontaneous-relaxation-enhanced GeSn buffer, n-type doped at 1×10^{19} cm^{-3}; (iii) a 1000 nm GeSn active region, undoped; (iv) the first GeSn or SiGeSn cap layer with p-type doping (boron) at 1×10^{18} cm^{-3}; (v) a 50 nm (Si)GeSn cap layer with p-type doping at 1×10^{19} cm^{-3}. The GeSn buffer layers had a varied Sn composition: 7-11% in samples A to D and 10-13% in sample E. The GeSn active region had a composition of 11% in samples A to D, and 13% in sample E. The dislocations induced by the crystalline strain relaxation is expected within the GeSn buffer layer.

The relaxation leads to a Sn gradient within the GeSn buffer. The dislocations are expected to cause a Sn gradient within the GeSn buffer and confined within some few hundreds of nanometers. The GeSn active region was then grown with the same recipe and low defect density. The standard in-situ dopant gas was introduced to form the n-type and p-type regions. A schematic of the laser structure is described in Fig. 69(a). The device actual thickness, composition, and the corresponding conduction band barrier height ΔEc between the cap layer and active region are summarized in Table 12.

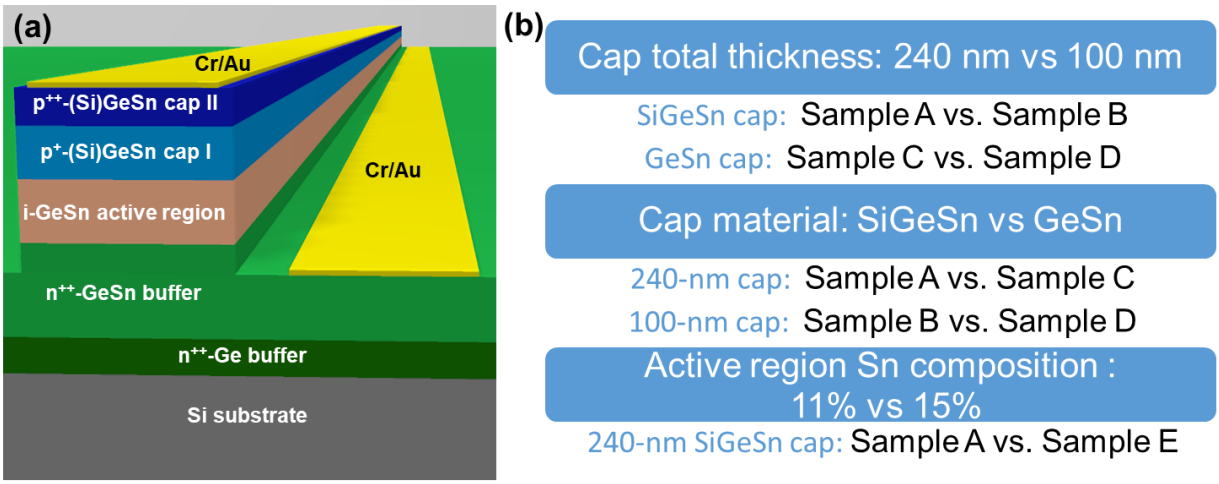

Figure 69. (a) 3D schematic of the ridge waveguide laser structure; (b) three experiment groups are studied with tuning of the total cap thickness, cap layer material, and active region Sn composition.

Table 12. Summary of laser structure

Sample	p-type Cap			GeSn Active Region		n-type Buffer	
	Material	Thickness (nm)	ΔE_c^* (meV)	Sn %	Thickness (nm)	Material	Thickness (nm)
A	$Si_{0.03}Ge_{0.89}Sn_{0.08}$	190	114	11.2	610	$Ge_{0.93}Sn_{0.07}$	950
B	$Si_{0.03}Ge_{0.89}Sn_{0.08}$	150	114	10.8	430	$Ge_{0.93}Sn_{0.07}$	670
C	$Ge_{0.95}Sn_{0.05}$	220	58	11.2	520	$Ge_{0.93}Sn_{0.07}$	650
D	$Ge_{0.95}Sn_{0.05}$	100	58	11.5	450	$Ge_{0.93}Sn_{0.07}$	610
E	$Si_{0.03}Ge_{0.89}Sn_{0.08}$	180	131	13.1	540	$Ge_{0.93}Sn_{0.07}$	540

The XRD RSMs are shown in Fig. 70. Four peaks (from peak 1 to 4) can be identified corresponding to four layers of the heterostructure: Ge buffer, GeSn buffer, GeSn active region, and (Si)GeSn cap, respectively. Samples A and C have similar peak position for peaks 1 to 3. The peak position of the SiGeSn cap in sample A is difficult to identify; it may overlap with the peak 2. In sample C, the GeSn cap has a smaller lattice constant because of the smaller Sn content. This leads to a larger tensile strain within the layer. In sample E, the higher Sn composition in the active region resulted in a larger in-plane and out-of-plane lattice constant in the active region and the SiGeSn cap layer. The extracted composition and strain information is summarized in Table 13.

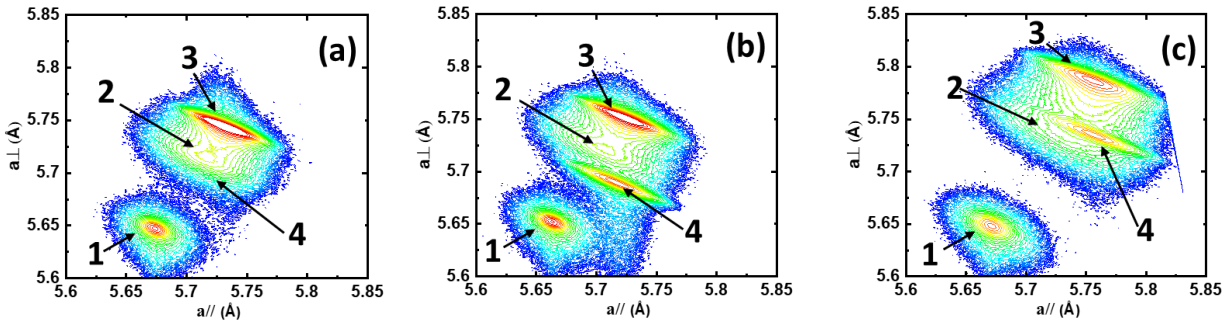

Figure 70. XRD RSM map for (a) sample A; (b) sample C; and (c) sample E.

Table 13. Sn composition and in plane strain extracted from XRD RSM

		Sample A	Sample C	Sample E
Peak 1 Ge buffer	Sn %	0	0	0
	Strain (%)	+0.10	+0.20	+0.13
Peak 2 GeSn buffer	Sn %	7.3	7.6	N.A.
	Strain (%)	-0.14	-0.07	N.A.
Peak 3 GeSn active region	Sn %	10.3	10.7	14.7
	Strain (%)	-0.27	-0.19	-0.39
Peak 4 (Si)GeSn Cap	Sn %	N.A.	5.8	N.A.
	Strain (%)	N.A.	+0.37	+0.12

The typical laser band-structure schematic diagrams are plotted in Fig. 71. The GeSn buffers feature a Sn composition gradient as the result of the spontaneous relaxation for the Sn composition enhancement growth technique. The Sn gradient forms the graded barrier in both conduction and valence bands. The GeSn active region keeps direct bandgap material thanks to the low residual compressive strain. In each sample, the cap layer experiences the tensile strain, leading to the light hole in the valence band having a weak type-II alignment. The GeSn cap in sample C has the lowest conduction band barrier height. And the SiGeSn cap in samples A and E features a higher barrier height, which enhances the electron confinement.

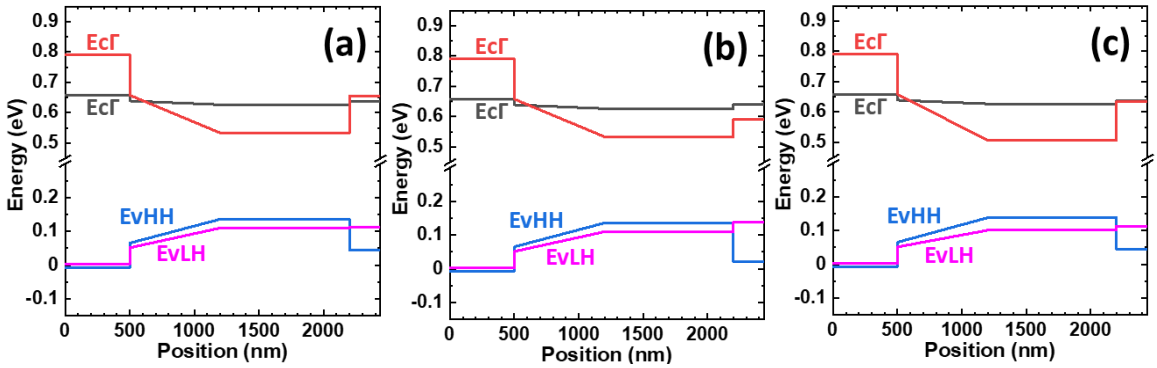

Figure 71. Schematic band diagrams for (a) sample A; (b) sample C; and (c) sample E.

Device fabrication: The laser diode devices were fabricated into ridge waveguide laser structure. The 80-μm-wide ridge structure was formed by standard photolithography and wet chemical etching. The ridge was etched to the n-type GeSn buffer (200 nm etched into the buffer layer). The metal contacts (10 nm Cr + 350 nm Au) were deposited by using an electron beam evaporator. The Si substrate on the back side was reduced to ~140 μm thickness by lapping, followed by a cleaving to form the facets. The cavity length falls between 1.2 and 1.7 mm. The laser diodes were wire-bonded onto a Si carrier with isolated Au bonding pads.

Experimental design: Three sets of experiments were designed to study the GeSn laser

structures, summarized in Fig. 69(b). The first set adjusts the total thickness of the cap layer in order to evaluate the optical mode-profile effect on the optical confinement factor as well as the absorption loss. Samples A and C have the total cap thickness of 190 nm compared to 150 nm in samples B and D, respectively. The second variable is the material used in the cap layers that changes conduction-band barrier height in the heterostructure. $Si_{0.03}Ge_{0.89}Sn_{0.08}$ with 114 meV of barrier height is used in samples A and B, compared to $Ge_{0.95}Sn_{0.05}$ with 58 meV barrier height used in samples C and D. The last experiment evaluates the device performance affected by the Sn composition in the GeSn active region. Sample E has a nominal 13% of Sn in the active region, compared to 11% in sample A. Note that sample A which has been described in section 5.1 as reference in this work.

Experimental methods: The PL was measured from the cap-removed sample. The heterostructure sample was chemically etched. And the top 600 nm of structure was removed, and the active region was exposed at the surface for PL characterization. The sample surface was excited by using the 532-nm continuous wave laser at 500 mW. The emission was collected through the spectrometer with the InSb detector. The signal was recorded via a standard lock-in technique.

For the electrically injected laser measurement, the chip was mounted in a temperature-controlled cryostat for the characterization. The device operated under a pulsed mode to avoid Joule heating. The pulsed voltage source was used as the pumping source with a 1-kHz repetition rate and 700 ns of pulse width. The emission power and spectra were characterized using a grating-based spectrometer equipped with a liquid-nitrogen-cooled InSb detector (detection range 1.0-5.5 μm). The spectra presented in this paper focus on comparing the peak wavelength and on demonstrating the emission below and above the lasing threshold. Therefore,

the resolution of the spectrometer is set at 10 nm, which is compromised to obtain a reasonable signal-to-noise ratio for the spectrum, especially at the low intensity level below the threshold. The absolute optical power was measured using a calibrated power meter. The emission from the facet was coupled by a pair of convex lenses and focused on the power meter. Note that the reflection and absorption losses through the cryostat window and lens were calculated and were added to the power meter readout aiming to report more accurate emission power. The emission was then guided onto the InSb detector through the spectrometer for the L-I and spectral measurements. The detailed description of the high-resolution spectra and the absolute power calibration process can be found in section 5.1.

Observation of Lasing: To validate the lasing operation, the devices characteristics were measured using the same method that was detailed in last section. According to measurement results, all devices show unambiguous lasing characteristics, as the threshold indicating the onset of lasing, dramatically reduced peak linewidth and increased peak intensity were clearly observed, which were acknowledged to identify the lasing of sample A in section 5.1. The typical characterization results of sample E are shown in Fig. 72.

Figure 72(a) displays the temperature dependent light output-current injection (L-I) curves for sample E. The threshold characteristic can be clearly resolved. The lasing was observed at temperatures 10 to 90 K, with the threshold from 1.4 to 3.6 kA/cm^2. The characteristic temperature T_0 was extracted as 81 K. The maximum output was measured of 0.7 mW/facet under 4 kA/cm^2 at 30 K. From 10 to 50 K, the kink can be observed at ~ 1.5×J_{th}, which may be due to the switch of lasing-mode.

Figure 72(b) shows the emission spectra below and above the lasing threshold at 10 K. The PL spectrum at 10 K was also plotted for comparison (dotted line). Compared to the PL

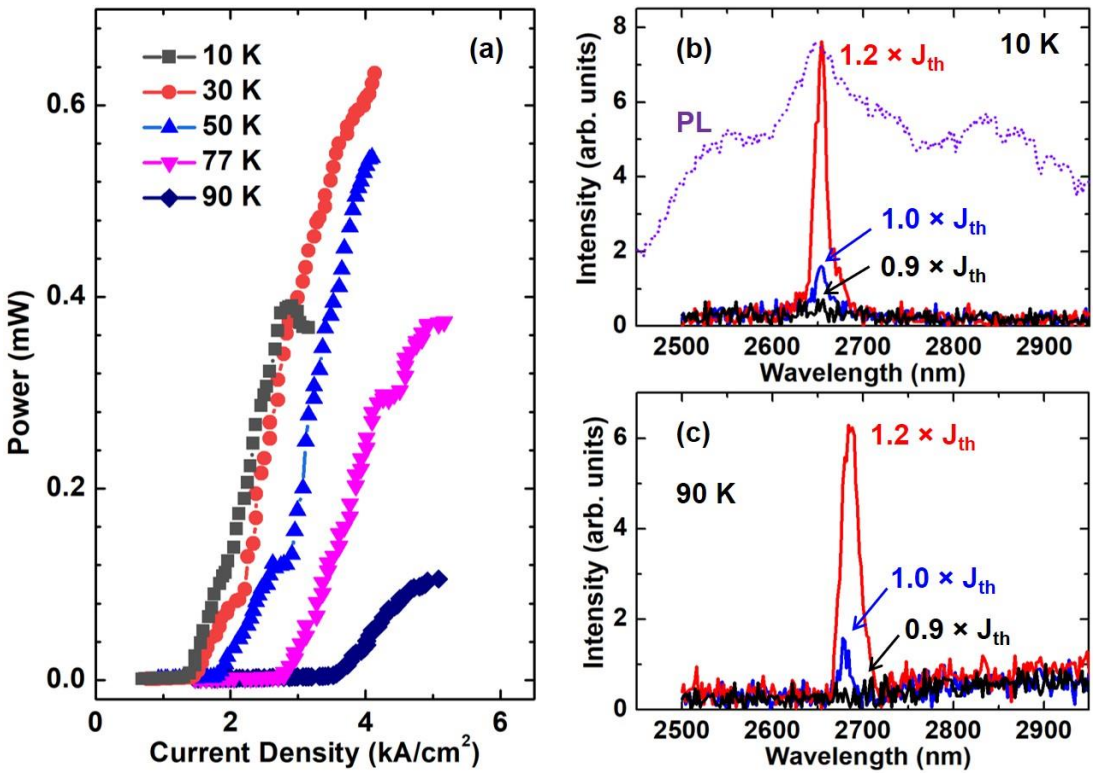

Figure 72. Characterizations of Sample E. (a) Temperature dependent L-I curve; (b) Lasing spectra under injections below and above threshold at 10 K. The PL spectrum was also plotted for comparison; (c) Emission spectra under injections below and above.

peak, the significantly reduced emission peak linewidth indicates the onset of lasing. Note that based on the previous study [35,46,77], the devices feature multi-mode operation, and therefore the observed peak consists of multi-mode peaks (e.g. see the spectra in Fig. 72(b) for $1.2\times J_{th}$ and that in Fig. 72(c) for $1.0\times J_{th}$), which cannot be further resolved due to the spectrometer resolution of 10 nm. As current injection increases to above threshold, a narrower linewidth peak sitting on background spontaneous emission emerges, whose intensity dramatically increases at $1.2\times J_{th}$. This trend indicates the unambiguous lasing characteristic. The lasing peak wavelength was measured as 2654 nm at $1.2\times J_{th}$ at 10 K. The emission spectra at 90 K are plotted in Fig. 72(c). The spontaneous emission (at $0.9\times J_{th}$) from the active region cannot be resolved due to the low intensity. In a semi-log plot, below threshold ($0.9\times J_{th}$), a broad peak at ~2600 to 3000 nm with

relatively weak intensity was obtained, suggesting the spontaneous emission. The linewidth difference between stimulated and spontaneous emission can be clearly identified from the semi-log spectra. The intensity of the broad emission peak has barely changed intensity as the injection increased, which is due to the pinning of the carrier density contributing to the spontaneous emission. The lasing peak can be clearly identified at injection above the threshold. Under injection of $1.2\times J_{th}$ at 90 K, the lasing wavelength was measured as 2682 nm.

Light output-current injection characteristics: The L-I curves of all devices at 10 K are plotted in Fig. 73(a). Sample A features the lowest threshold while sample D has the highest threshold, which are 0.6 and 3.4 kA/cm^2, respectively. It is worth noting that regarding the curve slope above the threshold, samples A, C, and E exhibit similar slope, which is higher than that of samples B and D. Except for reference sample A, sample C shows the maximum output power of 1.05 mW/facet under 5.5 kA/cm^2.

As temperature increases, sample D stops lasing above 10 K. Figure 73(b) shows L-I curves of all other samples at 50 K. The lowest and highest thresholds are 0.8 kA/cm^2 (sample

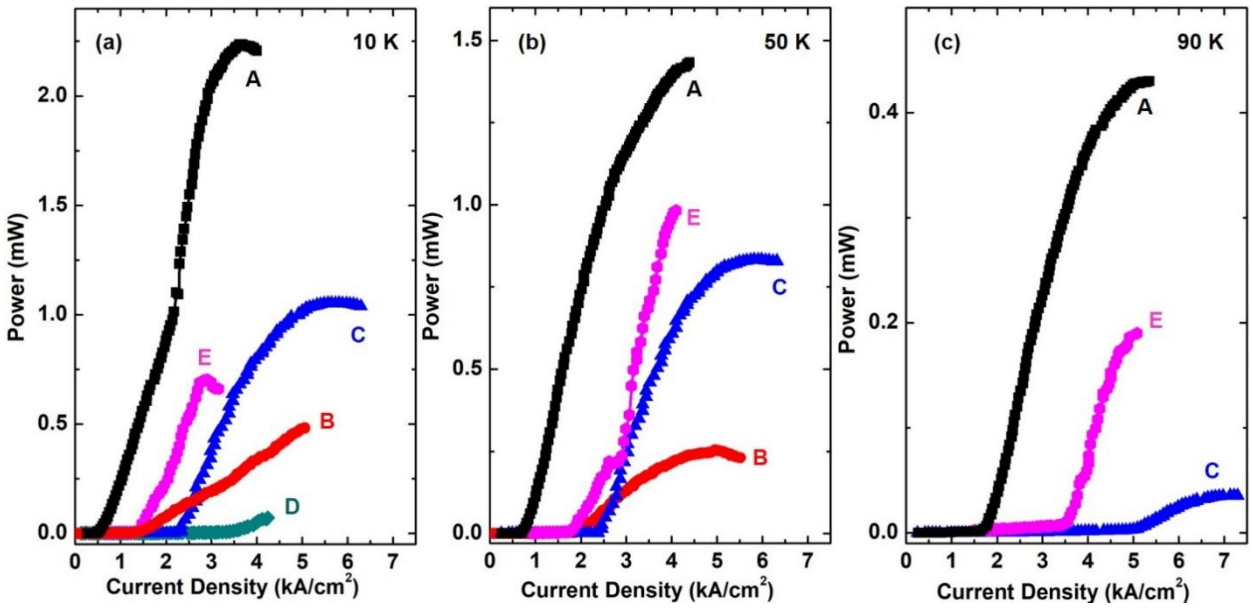

Figure 73. L-I curves of each sample at (a) 10 K; (b) 50 K; and (c) 90 K.

A) and 2.5 kA/cm^2 (sample C), respectively. Sample B shows a lower curve slope above the threshold compared to the other three samples. As temperature further increases, sample B stops lasing above 50 K. The L-I curves of samples A, C, and E at 90 K are shown in Fig. 73(c), with the corresponding thresholds of 1.8, 5.1, and 3.6 3.4 kA/cm^2, respectively. The maximum operational temperature of samples C and E is 90 K, while for sample A it is 100 K, which has been reported in section 5.1.

Figure 74 shows the laser peak emission under injection of 1.1×J_{th}. At 10 K, the lasing peak of sample A was obtained at 2240 nm. While for samples B, C, and D the lasing peaks were observed at ~2270-2290 nm. This is due to the slight difference of Sn compositions in the active region. The lasing peak of sample E is at 2654 nm, much longer than the rest of the samples due to the higher Sn composition (13% vs. 11%) in active region. As the temperature increases, the peak emission shifts towards longer wavelength as expected, which represents a narrower bandgap at higher temperature. At 90 K, the lasing peak was obtained at 2682 nm for sample E. Note that the lasing spectra peak shift is almost equivalent to the temperature shift of bandgap energy, i.e., following the Varshni relation:

$$E_{GeSn}(T) = E_{GeSn}(0) - \alpha T^2/(T + \beta) \qquad \text{(Equation 5.1)}$$

where $E_{GeSn}(0)$ is the bandgap energy at 0 K, and α and β are the material-dependent parameters. The values of α and β were studied in our previous work [84], which are comparable to III-V material system (α ~10^{-4} eV/K^2 and β ~200 K).

For samples A to E, the full widths at half maximum (FWHM) incorporating all lasing modes were measured as 32, 29, 18, 34, and 16 nm (under the 10 nm resolution spectrometer), respectively at 10 K. Our previous studies revealed that due to the relatively large area of cross section, all laser devices feature multi-mode operation. The high-resolution lasing spectra

showing well-resolved multi-peaks of sample A was reported in last section. The characteristics for all laser devices are summarized in Table 14.

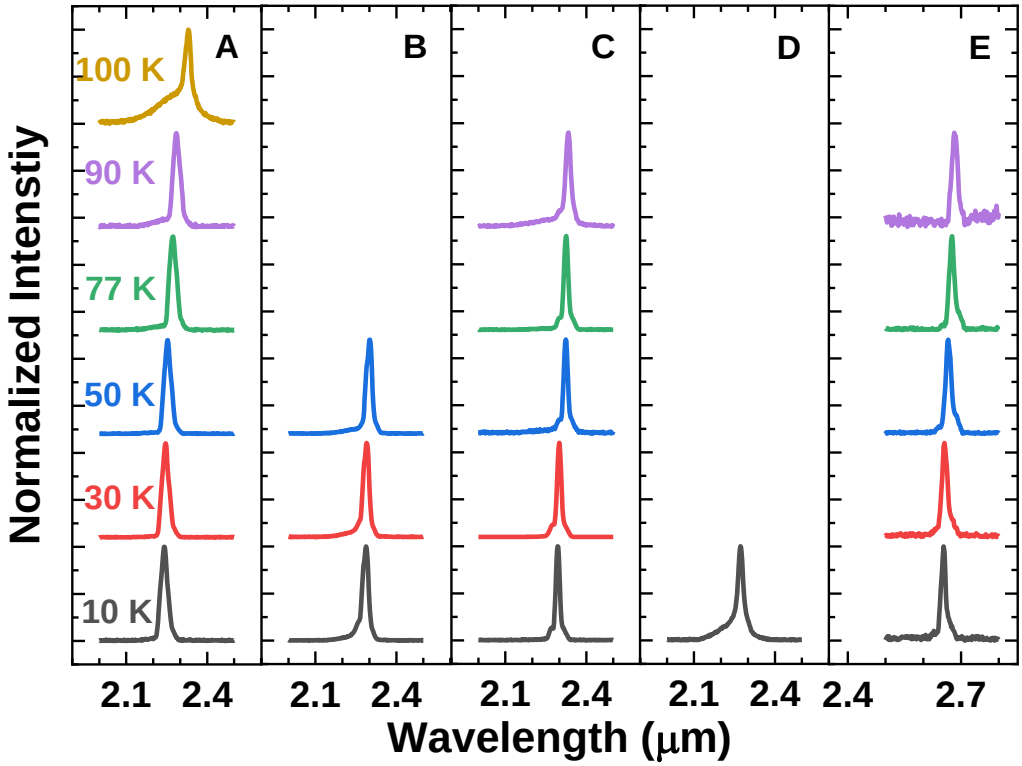

Figure 74. Normalized spectra showing the lasing peaks under 1.1×J_{th} injection for each sample at the corresponding operational temperatures.

Table 14. Summary of laser characteristics.

Sample	Cap Layer Material	Cap Layer Thickness (nm)	Sn % in Active Region	J_{th} at 10 K (kA/cm^2)	J_{th} at 77 K (kA/cm^2)	T_{max} (K)	T_0 (K)	Lasing Wave-length at 10 K (nm)
A	$Si_{0.03}Ge_{0.89}Sn_{0.08}$	190	11	0.6	1.4	100	76	2238
B	$Si_{0.03}Ge_{0.89}Sn_{0.08}$	150	11	1.4	N.A.	50	119	2281
C	$Ge_{0.95}Sn_{0.05}$	220	11	2.4	3.1	90	123	2294
D	$Ge_{0.95}Sn_{0.05}$	100	11	3.4	N.A.	10	N.A.	2272
E	$Si_{0.03}Ge_{0.89}Sn_{0.08}$	180	13	1.4	2.9	90	81	2654

Thickness of cap layer (first experimental group in Fig. 69(b)): The total thickness of the

cap layer affects considerably the lasing performance. Both comparisons (A vs. B and C vs. D) show the same trend, no matter whether SiGeSn or GeSn is used as cap layer material - that a thicker cap device has a lower lasing threshold as well as higher maximum operating temperature: at 10 K; sample A has a threshold that is 0.43 of that of sample B; while sample C has a lower threshold that is 0.70 of sample D. For the maximum operating temperature, 100 K for sample A vs. 50 K for sample B, and 90 K for sample C vs. 10 K for sample D were observed. The change of cap layer thickness affects the laser performance by the following factors: (i) optical loss from the metal contact plays the major role, (ii) FCA within the heavily doped cap layers, and (iii) optical confinement factor in the active region.

The optical loss on the metal contacts was originated from the imaginary part of the refractive index [85]. The metal absorption was extracted from the dielectric waveguide simulation. Using structure in sample A, the metal absorption loss is plotted as a function of SiGeSn cap total thickness in Fig. 75. As cap layer thickness increases, the absorption loss decreases. The metal absorption loss is reduced from 1287 to 554 cm^{-1} (from sample B to A)

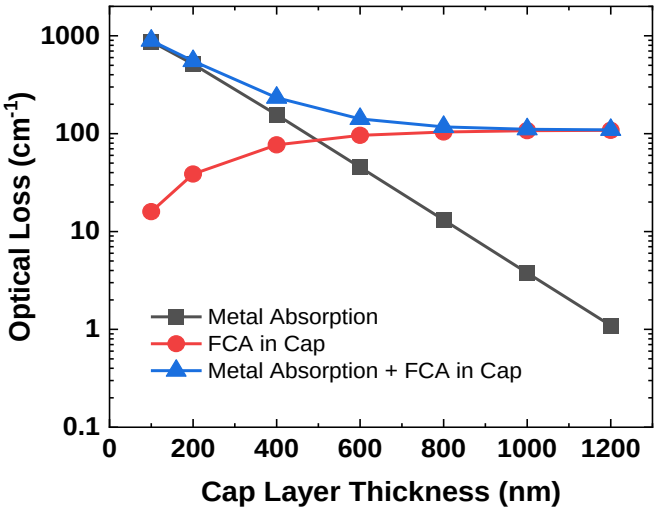

Figure 75. Calculated metal absorption loss and FCA loss in p-type cap layer for sample A as the functions of SiGeSn cap layer total thickness.

and from 1724 to 720 cm^{-1} (from sample D to C) when the cap thickness increased from 100 (B and D) to ~200 nm (A, C, and E). As the cap layer thickness increases from 100 to 1200 nm, the absorption loss decreases to as low as 1 cm^{-1}. The calculated metal absorption loss for each sample is summarized in Table 15. Compared to other source of optical loss, the metal absorption is the dominating loss mechanism in the structure. Note that the metal scattering loss is not counted here.

Table 15. Calculated Loss.

Sample #	P-type Cap Free Carrier Absorption Loss (cm^{-1})	Active Region Free Carrier Absorption Loss (cm^{-1})	N-type Buffer Free Carrier Absorption Loss (cm^{-1})	Metal Absorption Loss (cm^{-1})	Total Loss (cm^{-1})
A	0.7	22.3	0.17	4.9	28.1
B	2.3	22.9	0.15	10	35.4
C	0.8	22.4	0.17	4.9	28.3
D	2.7	23.0	0.15	10	35.9
E	1.2	23.1	0.17	5.3	29.8

The FCA loss of each layer was calculated based on the doping level and the carrier injection [86], as summarized in Table 15. Considerable amount of FCA is introduced in the active region, serving as the second dominating loss mechanism. The n-type doped GeSn buffer shows a relatively small value (6~11 cm^{-1}) in each sample, while the p-type doped cap layer exhibits higher values (36 and 72 cm^{-1}). In active region, the FCA level is taken assuming high injection at 5.0×10^{18} cm^{-3}. Sample E exhibits a higher FCA loss due to a longer emission wavelength. In Fig. 75, the FCA in the p-type cap was plotted as a function of cap thickness using structure of sample A. The FCA in the cap increases as the cap thickness increases. The combination of metal absorption and FCA in cap can be reduced to ~110 cm^{-1} as the cap thickness reach beyond 800 nm. This promises the total loss for sample A can be reduced by

half at the threshold.

Overall, it can be seen that the higher total loss results in a larger threshold, comparing B to A (or D to C). The metal absorption loss dramatically decreases as the cap layer thickness increases, while the FCA loss shows limited change. As a result, the total loss would not further decrease with the thicker cap. Moreover, with very thick cap layer (~1000 nm), the optical confinement in active region may decrease due to the relatively small refractive index difference (~0.2) between active region and cap. On the other hand, since the critical thickness of SiGeSn cap on GeSn is less than 100 nm, the further relaxation of SiGeSn would result in material degradation due to the generation of dislocations.

Cap layer materials (second experimental group in Fig. 69(b)): The cap layer also serves as the top barrier with respect to active region. $Si_{0.03}Ge_{0.89}Sn_{0.08}$ and $Ge_{0.95}Sn_{0.05}$ are compared as the cap layer materials. Note that both cap materials feature tensile strain due to relatively smaller lattice constants with respect to the active layer, leading to type-II band alignment being obtained in the LH in the valence band (VB) at the cap/active interface, which creates a hole leakage channel. This issue was addressed by injecting holes from the top so that the holes flow from the p-type cap layer towards the n-type GeSn buffer, where the barrier at the active/GeSn buffer interface could confine the holes in the active region, as described in section 5.1. Therefore, the electron confinement offered by cap layers is a focus in this experiment.

The conduction band (CB) barrier height of each sample was calculated. For both comparisons (A vs. C and B vs. D: $Si_{0.03}Ge_{0.89}Sn_{0.08}$ vs. $Ge_{0.95}Sn_{0.05}$), no matter whether the cap layer thickness is 240 nm or 100 nm, the samples using $Si_{0.03}Ge_{0.89}Sn_{0.08}$ cap have the barrier height of 114 meV, while the samples using $Ge_{0.95}Sn_{0.05}$ cap show a lower barrier height of 58 meV. The higher barrier height improves the device performance due to better electron

confinement: (i) at 10 K, sample A has a much lower threshold that is 0.25 of that of sample C, while sample B has a threshold that is 0.41 of sample D. The similar threshold reduction was also reported on III-V laser devices [87]; (ii) for the maximum operating temperature, 100 K for sample A vs. 90 K for sample C, and 50 K for sample B vs. 10 K for sample D were obtained. As temperature increases, due to increased thermal energy k_BT that can be absorbed by carriers, the electron confinement capability is weakened, leading to the result that the samples using $Ge_{0.95}Sn_{0.05}$ cap (lower barrier height) stop lasing prior to those using $Si_{0.03}Ge_{0.89}Sn_{0.08}$ cap (higher barrier height). Note for sample D, because of its thin $Ge_{0.95}Sn_{0.05}$ cap (100 nm), it can only lase at 10 K.

The VB barrier height between the GeSn active and the GeSn buffer was calculated for each sample as well. Samples A to D show similar hole barrier height of ~30 meV. At room temperature, such a barrier is slightly greater than 1 k_BT, and therefore it is insufficient for hole confinement. A wider bandgap material, i.e., SiGeSn, can be used to replace the GeSn buffer for higher band barrier height in VB, to enhance hole confinement.

Sn compositions in the active region (third experimental group in Fig. 69(b)): Samples A ($Ge_{0.89}Sn_{0.11}$) and E ($Ge_{0.85}Sn_{0.13}$) are compared for the active region materials. Our previous studies on GeSn optically pumped lasers indicated that the increase of Sn composition in the active region led to the increase of the maximum operating temperature and reduction of lasing threshold [34,38,46]. This is attributed to the higher-Sn-induced greater directness of bandgap in the active region, which facilitates the electron populating the Γ valley. However, in this experiment, the electrically injected device with higher Sn composition neither shows reduced threshold nor exhibits increased operating temperature: At 10 and 77 K, the thresholds of sample E (1.4 and 2.9 kA/cm^2) are doubled compared to those of sample A (0.6 and 1.4 kA/cm^2); the

maximum lasing temperature of 90 K for sample E is 10 K lower than that of sample A. This can be interpreted as follows: (i) The total loss is calculated higher in sample E than in sample A. This is mainly due to the thinner well of sample E that leads to larger modal overlap with metal layer and elevated FCA loss at longer emission wavelength; (ii) The optically pumped lasers rely on optical absorption to collect the carriers. For a certain wavelength of incident light, the absorption coefficient increases as Sn composition in the GeSn active region increases due to narrower bandgap. However, for electrically injected lasers, the carrier injection efficiency does not show obvious improvement with sample E. Characterization of band offset could provide more detailed information; (iii) The GeSn active region with higher Sn composition has a larger lattice constant. The increased lattice mismatch between active region and buffer leads to increased dislocation density in the active region. Such dislocations serve as the non-radiative recombination center that reduce the carrier injection efficiency. Recent studies on GeSn DHS LEDs show similar issue that an increase of Sn composition does not directly improve the emission intensity [72, 26]. Therefore, a higher Sn composition in GeSn buffer might be helpful to maintain the high-quality active region; (iv) Sample A has a slightly longer cavity length of 1.7 mm compared to 1.3 mm for sample E. The longer cavity features reduced mirror loss, leading to a better performance. Note that the difference of mirror loss between samples A and E is relatively small (6 cm^{-1} vs 8 cm^{-1}) compared to other loss, and thus it is not a dominant factor in this experiment.

Additional considerations: In addition to the loss mechanism abovementioned, other factors that affect the device performance are elaborated as follows: (i) active layer thickness. In this work, the design of sample structure is inherited from the former optically pumped lasers, in which a thicker active layer is preferred, aiming to have higher light absorption. However, such

absorption enhancement with a thicker active layer does not apply to electrically injected lasers. In fact, growing a thinner active region could effectively reduce the threshold [88]. (ii) absorption loss in the GeSn buffer and the SiGeSn/GeSn cap. Since the GeSn buffer is almost relaxed and heavily doped, the high density of dislocations due to lattice mismatch would create defect energy levels in the bandgap, resulting in additional absorption loss. The absorption tails have been reported in GeSn materials, which lead to below-band-gap absorption with the orders of 1~10 cm^{-1} for extra loss [63,89]. Likewise, once the thicker cap layer beyond the critical thickness is employed, the gradually relaxed material would introduce considerable density of dislocations. Therefore, the lattice-matched cap layer is desirable, which again relies on the advance of SiGeSn material growth capability; (iii) the scattering loss induced by sidewall roughness. The relatively rough sidewall would result in additional scattering loss, especially for the device with a relatively wide ridge. Reducing the sidewall roughness by improving the fabrication procedure is a viable solution to reduce the scattering loss.

In conclusion, electrically injected GeSn laser diodes were studied with an evaluation of three factors in the structure: cap layer thickness, cap materials, and active region materials. The thicker capped devices feature lower metal absorption loss, offering a reduction of threshold and an elevation of maximum operating temperature. The devices with a $Si_{0.03}Ge_{0.89}Sn_{0.08}$ cap show lower threshold and higher maximum operating temperature compared to the devices using a $Ge_{0.95}Sn_{0.05}$ cap, which is due to the higher barrier height at the active/cap interface when employing the $Si_{0.03}Ge_{0.89}Sn_{0.08}$ cap. The 13% Sn in the active region, however, does not improve the device performance in terms of lasing threshold and temperature compared to an 11% Sn device, when the same $Si_{0.03}Ge_{0.89}Sn_{0.08}$ cap was used. The performance of high-Sn composition devices can be improved by employing a thinner active layer and a cap with less

lattice mismatch, which could reduce the dislocation density. The maximum lasing peak wavelength was measured at 2682 nm at 90 K from the devices with $Ge_{0.87}Sn_{0.13}$ in the active region.

Chapter 6: Summary and future works

6.1 Summary

This dissertation presented the GeSn based emitter development. The optically pumped lasers were studied using GeSn bulk and SiGeSn/GeSn MQW structure. Three generations of GeSn LED structures were developed, leading to a success demonstration of electrically injected GeSn lasers.

The bulk GeSn optically pumped laser was achieved T_{max} at temperatures up to 270 K. As the Sn incorporation increased to 20 %, the T_{max} was therefore elevated. The side-wall surface recombination effect was minimized by adopting a wide ridge waveguide, which the pumping light was mostly absorbed at top of the ridge.

The SiGeSn/GeSn/SiGeSn MQW optically pumped lasers were characterized. The thinner well device had a lower T_{max} at 20 K compared to 90 K for the thicker well device. The minimum threshold was measured at 25 and 62 kW/cm^2 at 10 and 77 K, respectively. The difference of the performance was tentatively interpreted as the diffidence of the gain volume (modal gain) between the two structures. The impact of QW number was studied at low temperatures. The result supported that the certain gain volume is required to overcome the internal loss in the device. The MQW structure was optimized by adding SiGeSn cap, which is expected to improve the optical confinement factor and, therefore, to increase the modal gain.

The Ge/GeSn/Ge DHS diodes with Sn composition up to 9.2% was characterized at temperatures from 77 to 300 K. The bandgap calculation revealed that all GeSn lasers are indirect bandgap material. The type-I alignment was achieved with the barrier height from 11 to 47 meV. Since the higher probability from the direct bandgap than from indirect bandgap, the

direct bandgap emission was observed. GeSn homojunction diode with Sn composition of 11% was characterized. The direct bandgap GeSn active region was achieved by the relaxation thanks to the SRE growth technique. The direct bandgap emission was observed with operation under higher duty cycle pulse injection. The emission wavelength reached to 2470 nm at 300 K. The GeSn/GeSn/(Si)GeSn DHS LEDs were characterized. Temperature dependent spectra under CW injection was achieved. The higher barriers from SiGeSn cap offered an enhanced emission intensity compared to GeSn capped device.

Electrically injected laser was firstly demonstrated with the GeSn/GeSn/SiGeSn DHS structure. The minimum threshold was measured as 0.6 kA/cm^2 at 10 K. The device exhibited multimode transition with individual peak linewidth as small as 0.13 nm. Optical power was measured with maximum at 2.7 mW/facet and 0.3% external quantum efficiency. The DHS lasers were evaluated by varying the cap thickness, cap material, and active region Sn composition. At 10 K, the thicker cap (240 nm) devices had reduced threshold and elevated T_{max} compared to thinner cap (100 nm) devices. The SiGeSn capped devices had reduced threshold and elevated T_{max} compared to GeSn capped devices. The device with Sn composition at 15% in active region was compared to the device with Sn composition at 11%. The emission peak wavelength was reached to 2682 nm at 90 K. The threshold was elevated and the T_{max} was reduced to 10 K.

6.2 Future work

With the study presented in previous chapters, there are still open areas to be developed in GeSn laser diodes. Defect management, optical loss reduction, and carrier confinement are three potential directions. Moreover, a MQW structure could be used to replace the GeSn bulk,

to reduce the threshold towards CW operation at room temperature.

Defect management is always one of the most critical factors for lasers. Threading dislocations induced by the lattice mismatch play a significant role in the GeSn laser performance. This type of defect can be greatly reduced by using the lattice-matched layers that significantly reduce the lattice mismatch in the active region. To achieve the epitaxial growth of lattice-matched layers, it would require exploring the growth recipes with designed compositions. With a low level of defect density, the carrier injection can be improved and the SRH recombination can be reduced, both promising a higher laser efficiency.

The optical loss was discussed in chapter 5. The metal absorption can be further reduced by increase the thickness cap of the cap layer. The thick cap is preferred to separate the optical mode and the metal contact. In addition, the thicker cap would simultaneously increase the series resistance and the FCA. Both side effects would potentially impact the laser negatively. The increase of series resistance would result in more power consumption and higher temperature. The FCA would be increased in the cap layer as more mode is pushed towards the cap layer. Inevitably, an optimization effort would help to find the right cap thickness and doping profile so that the conflicts mentioned above would be balanced.

One would acknowledge that the band offset of the SiGeSn has not been experimentally examined. A thorough investigation of the band offset in SiGeSn heterostructures would benefit the GeSn laser significantly. The study would provide more confidence for bandgap engineering. The carrier confinement of the GeSn DHS can be further investigated by adopting the optimization methods applied in conventional III-V lasers. A broad opportunity awaits to apply the knowledge of bandgap engineering on GeSn lasers.

As the DHS structure laser diodes developed, the MQW structure is of great interest to

further enhance the carrier confinement by using quantum confinement. The enhanced confinement would promise a lower threshold and higher T_{max} by using the MQW structure. Although the optically pumped GeSn MQW was discussed in chapter 3, the mechanism of low T_{max} remains to be carefully investigated. Finally, the electrically injected GeSn MQW laser is the next milestone to be achieved.

To achieve the monolithic lasers on the Si platform requires tremendous efforts, yet the outcome is quite attractive—the monolithic integration of Si photonics. By standing on the shoulders of giants, the light of the GeSn laser is glaring and beaming forwards.

References

[1] Y. development, "Silicon photonics: datacom, yes, but not only…'," Press Release, May 5, 2020. http://www.yole.fr/Si_Photonics_Datacom_Sensing.aspx. Accessed 08 Oct. 2020.

[2] A. Rickman, "The commercialization of silicon photonics," Nature Photonics 8, pp. 579-582 (2014).

[3] X. Sun, L. Zhang, Q. Zhang, and W. Zhang, "Si Photonics for Practical LiDAR Solutions," Applied Sciences-Basel 9 (2019).

[4] R. Soref, "Silicon Photonics: A Review of Recent Literature," Silicon 2, 1-6 (2010).

[5] A. E.-J. Lim, J. Song, Q. Fang, C. Li, X. Tu, N. Duan, K. K. Chen, R. P.-C. Tern, and T.-Y. Liow., "Review of Silicon Photonics Foundry Efforts," IEEE Journal of Selected Topics in Quantum Electronics, vol. 20, no. 4, pp. 405-416, Art no. 8300112 (2014).

[6] R. Soref, "The past, present, and future of silicon photonics," Ieee Journal of Selected Topics in Quantum Electronics 12, 1678-1687 (2006).

[7] J. Bradley, R. Stoffer, L. Agazzi, F. Ay, K. Worhoff, and M. Pollnau, "Integrated Al2O3:Er3+ ring lasers on silicon with wide wavelength selectivity," Optics Letters 35, 73-75 (2010).

[8] E. Bernhardi, H. van Wolferen, L. Agazzi, M. Khan, C. Roeloffzen, K. Worhoff, M. Pollnau, and R. de Ridder, "Ultra-narrow-linewidth, single-frequency distributed feedback waveguide laser in Al2O3:Er3+ on silicon," Optics Letters 35, 2394-2396 (2010).

[9] H. Rong, A. Liu, R. Jones, O. Cohen, D. Hak, R. Nicolaescu, A. Fang, and M. Paniccia, "An all-silicon Raman laser," Nature 433, 292-294 (2005).

[10] J. Liu, X. Sun, R. Camacho-Aguilera, L. Kimerling, and J. Michel, "Ge-on-Si laser operating at room temperature," Optics Letters 35, 679-681 (2010).

[11] H. Park, A. W. Fang, S. Kodama, and J. E. Bowers, "Hybrid silicon evanescent laser fabricated with a silicon waveguide and III-V offset quantum wells," Opt. Express 13, 9460-9464 (2005).

[12] S. Chen, W. Li, J. Wu, Q. Jiang, M. Tang, S. Shutts, S. N. Elliott, A. Sobiesierski, A. J. Seeds, I. Ross, P. M. Smowton, and H. Liu, "Electrically pumped continuous-wave III-V quantum dot lasers on silicon," Nature Photonics 10, 307-311 (2016).

[13] R. Soref “Silicon-based silicon–germanium–tin heterostructure photonics,” Phil. Trans. R. Soc. A.37220130113 (2014).

[14] R. Soref, and L. Friedman, “Direct-gap Ge/GeSn/Si and GeSn/Ge/Si heterostructures," Superlattices and Microstructures 14, 189-193 (1993).

[15] B. R. Conley, A. Mosleh, S. A. Ghetmiri, H. A. Naseem, J. Tolle, and S.-Q. Yu, "CVD growth of Ge1-xSnx using large scale Si process for higher efficient multi-junctionsolar cells," in Photovoltaic Specialists Conference (PVSC), 2013 IEEE 39th, pp. 1346-1349 (2013).

[16] S. I. Shah, J. E. Green, L. L. Abels, Y. Yao, and P. M. Raccah, “Growth of single-crystal metastable Ge1-xSnx alloys on Ge(100) and GaAs(100) substrates,” J. Cryst. Growth, vol.83, no. 1, pp. 3–10 (1987).

[17] H. Höchst, M. A. Engelhardt, and I. Hernandez-Calderan, “Angle-resolved photoemission study of thin molecular-beam-epitaxy-grown -Sn1-xGex films with x0.5,” Phys. Rev. B, vol. 40, no. 14, pp. 9703–9708 (1989).

[18] J. Taraci, S. Zollner, M. R. McCartney, J. Menendez, M. A. Santana-Aranda, D. J. Smith, A. Haaland, A. V. Tutukin, G. Gundersen, G. Wolf, and J. Kouvetakis, “Synthesis of silicon-based infrared semiconductors in the Ge-Sn system using molecular chemistry methods,” J. Am. Chem. Soc., vol. 123, no. 44, pp. 10980–10987 (2001).

[19] R. Roucka, J. Mathews, R. T. Beeler, J. Tolle, J. Kouvetakis, and J. Menéndez, "Direct gap electroluminescence from Si/Ge1−ySny p-i-n heterostructure diodes," Applied Physics Letters 98, 061109 (2011).

[20] M. Oehme, J. Werner, M. Gollhofer, M. Schmid, M. Kaschel, E. Kasper, and J. Schulze, "Room-Temperature Electroluminescence From GeSn Light-Emitting Pin Diodes on Si," IEEE Photonics Technology Letters 23, 1751-1753 (2011).

[21] H. H. Tseng, K. Y. Wu, H. Li, V. Mashanov, H. H. Cheng, G. Sun, and R. A. Soref, "Mid-infrared electroluminescence from a Ge/Ge0.922Sn0.078/Ge double heterostructure p-i-n diode on a Si substrate," Applied Physics Letters 102, 182106 (2013).

[22] J. P. Gupta, N. Bhargava, S. Kim, T. Adam, and J. Kolodzey, "Infrared electroluminescence from GeSn heterojunction diodes grown by molecular beam epitaxy," Applied Physics Letters 102, 251117 (2013).

[23] J. D. Gallagher, C. L. Senaratne, P. Sims, T. Aoki, J. Menéndez, and J. Kouvetakis, "Electroluminescence from GeSn heterostructure pin diodes at the indirect to direct transition," Applied Physics Letters 106, 091103 (2015).

[24] B. Schwartz, M. Oehme, K. Kostecki, D. Widmann, M. Gollhofer, R. Koerner, S. Bechler, I. A. Fischer, T. Wendav, E. Kasper, J. Schulze, and M. Kittler,

"Electroluminescence of GeSn/Ge MQW LEDs on Si substrate," Optics Letters 40, 3209-3212 (2015).

[25] D. Stange, N. von den Driesch, D. Rainko, S. Roesgaard, I. Povstugar, J.-M. Hartmann, T. Stoica, Z. Ikonic, S. Mantl, D. Grützmacher, and D. Buca, "Short-wave infrared LEDs from GeSn/SiGeSn multiple quantum wells," Optica 4, 185-188 (2017).

[26] M. Bertrand, N. Pauc, Q. M. Thai, J. Chrétien, L. Casiez, A. Quintero, P. Rodriguez, R. Khazaka, J. Aubin, J. M. Hartmann, A. Chelnokov, V. Calvo, and V. Reboud, "Mid-Infrared GeSn-Based LEDs with Sn Content up to 16%," in 2019 IEEE 16th International Conference on Group IV Photonics (GFP), pp. 1-2 (2019).

[27] G. Sun, R. A. Soref, and H. H. Cheng, "Design of an electrically pumped SiGeSn/GeSn/SiGeSn double-heterostructure midinfrared laser," Journal of Applied Physics, vol. 108, no. 3, p. 033107 (2010).

[28] G. Chang, S. Chang and S. L. Chuang, "Strain-Balanced Ge_zSn_{1-z}—$Si_xGe_ySn_{1-x-y}$ Multiple-Quantum-Well Lasers," in IEEE Journal of Quantum Electronics, vol. 46, no. 12, pp. 1813-1820 (2010).

[29] Sun, R. A. Soref, and H. H. Cheng, "Design of a Si-based lattice-matched room-temperature GeSn/GeSiSn multi-quantum-well mid-infrared laser diode," Optics Express, vol. 18, no. 19, pp. 19957-19965 (2010).

[30] R. Chen, S. Gupta, Y.-C. Huang, Y. Huo, C. W. Rudy, E. Sanchez, Y. Kim, T. I. Kamins, K. C. Saraswat, and J. S. Harris, "Demonstration of a Ge/GeSn/Ge Quantum-Well Microdisk Resonator on Silicon: Enabling High-Quality Ge(Sn) Materials for Micro- and Nanophotonics," Nano Letters 14, 37-43 (2014).

[31] S. A. Ghetmiri, W. Du, J. Margetis, A. Mosleh, L. Cousar, B. R. Conley, L. Domulevicz, A. Nazzal, G. Sun, R. A. Soref, J. Tolle, B. Li, H. A. Naseem, and S.-Q. Yu, "Direct-bandgap GeSn grown on silicon with 2230 nm photoluminescence," Applied Physics Letters 105, 151109 (2014).

[32] S. Wirths, R. Geiger, N. von den Driesch, G. Mussler, T. Stoica, S. Mantl, Z. Ikonic, M. Luysberg, S. Chiussi, J. M. Hartmann, H. Sigg, J. Faist, D. Buca, and D. Grützmacher, "Lasing in direct-bandgap GeSn alloy grown on Si," Nature Photonics 9, 88 (2015).

[33] D. Stange, N. v. d. Driesch, T. Zabel, F. Armand-Pilon, B. Marzban, D. Rainko, J. Hartmann, G. Capellini, T. Schroeder, H. Sigg, J. Witzens, D. Grützmacher, and D. Buca, "Reduced threshold microdisk lasers from GeSn/SiGeSn heterostructures," in 2017 IEEE 14th International Conference on Group IV Photonics (GFP)(2017), pp. 15-16.

[34] V. Reboud, A. Gassenq, N. Pauc, J. Aubin, L. Milord, Q. M. Thai, M. Bertrand, K. Guilloy, D. Rouchon, J. Rothman, T. Zabel, F. Armand Pilon, H. Sigg, A. Chelnokov, J.

Hartmann, and V. Calvo, “Optically pumped GeSn micro-disks with 16% Sn lasing at 3.1 μm up to 180 K,” Appl. Phys. Lett. 111, 092101 (2017).

[35] J. Margetis, S. Al-Kabi, W. Du, W. Dou, Y. Zhou, T. Pham, P. Grant, S. Ghetmiri, A. Mosleh, B. Li, J. Liu, G. Sun, R. Soref, J. Tolle, M. Mortazavi, and S. Yu, “Si-based GeSn lasers with wavelength coverage of 2–3 μm and operating temperatures up to 180 K,” ACS Photon. 5, 827–833 (2017).

[36] D. Stange, S. Wirths, R. Geiger, C. Schulte-Braucks, B. Marzban, N. von den Driesch, G. Mussler, T. Zabel, T. Stoica, J.-M. Hartmann, S. Mantl, Z. Ikonic, D. Grützmacher, H. Sigg, J. Witzens, and D. Buca, "Optically Pumped GeSn Microdisk Lasers on Si," ACS Photonics 3, 1279-1285 (2016).

[37] W. Dou, Y. Zhou, J. Margetis, S. A. Ghetmiri, S. Al-Kabi, W. Du, J. Liu, G. Sun, R. A. Soref, J. Tolle, B. Li, M. Mortazavi, and S.-Q. Yu, "Optically pumped lasing at 3 μm from compositionally graded GeSn with tin up to 22.3%," Opt. Lett. 43, 4558-4561 (2018)

[38] Q. M. Thai, N. Pauc, J. Aubin, M. Bertrand, J. Chrétien, V. Delaye, A. Chelnokov, J.-M. Hartmann, V. Reboud, and V. Calvo, "GeSn heterostructure micro-disk laser operating at 230 K," Opt. Express 26, 32500-32508 (2018).

[39] D. Stange, N. von den Driesch, T. Zabel, F. Armand-Pilon, D. Rainko, B. Marzban, P. Zaumseil, J.-M. Hartmann, Z. Ikonic, G. Capellini, S. Mantl, H. Sigg, J. Witzens, D. Grützmacher, and D. Buca, "GeSn/SiGeSn Heterostructure and Multi Quantum Well Lasers," ACS Photonics 5, 4628-4636 (2018).

[40] W. Du, Q. Thai, J. Chretien, M. Bertrand, L. Casiez, Y. Zhou, J. Margetis, N. Pauc, A. Chelnokov, V. Reboud, V. Calvo, J. Tolle, B. Li, and S. Yu, "Study of Si-Based GeSn Optically Pumped Lasers With Micro-Disk and Ridge Waveguide Structures," Frontiers in Physics 7 (2019).

[41] A. Elbaz, R. Arefin, E. Sakat, B. Wang, E. Herth, G. Patriarche, A. Foti, R. Ossikovski, S. Sauvage, X. Checoury, K. Pantzas, I. Sagnes, J. Chrétien, L. Casiez, M. Bertrand, V. Calvo, N. Pauc, A. Chelnokov, P. Boucaud, F. Boeuf, V. Reboud, J.-M. Hartmann, and M. El Kurdi, "Reduced Lasing Thresholds in GeSn Microdisk Cavities with Defect Management of the Optically Active Region," ACS Photonics, 7, 10, 2713–2722 (2020).

[42] A. Elbaz, D. Buca, N. von den Driesch, K. Pantzas, G. Patriarche, N. Zerounian, E. Herth, X. Checoury, S. Sauvage, I. Sagnes, A. Foti, R. Ossikovski, J. Hartmann, F. Boeuf, Z. Ikonic, P. Boucaud, D. Grutzmacher, and M. El Kurdi, "Ultra-low-threshold continuous-wave and pulsed lasing in tensile-strained GeSn alloys," Nature Photonics 14, 375 (2020).

[43] P. C. Grant, J. Margetis, Y. Zhou, W. Dou, G. Abernathy, A. Kuchuk, W. Du, B. Li, J. Tolle, J. Liu, G. Sun, R. A. Soref, M. Mortazavi, and S.-Q. Yu, "Direct bandgap type-I

GeSn/GeSn quantum well on a GeSn- and Ge- buffered Si substrate," AIP Advances 8, 025104 (2018).

[44] W. Dou, M. Benamara, A. Mosleh, J. Margetis, P. Grant, Y. Zhou, S. Al-Kabi, W. Du, J. Tolle, B. Li, M. Mortazavi, and S.-Q. Yu, "Investigation of GeSn Strain Relaxation and Spontaneous Composition Gradient for Low-Defect and High-Sn Alloy Growth," Scientific Reports 8, 5640 (2018).

[45] J. Margetis, S.-Q. Yu, N. Bhargava, B. Li, W. Du, and J. Tolle, "Strain engineering in epitaxial Ge1−xSnx: a path towards low-defect and high Sn-content layers," Semiconductor Science and Technology 32, 124006 (2017).

[46] Y. Zhou, W. Dou, W. Du, S. Ojo, H. Tran, S. A. Ghetmiri, J. Liu, G. Sun, R. Soref, J. Margetis, J. Tolle, B. Li, Z. Chen, M. Mortazavi, and S.-Q. Yu, "Optically Pumped GeSn Lasers Operating at 270 K with Broad Waveguide Structures on Si," ACS Photonics 6, 1434-1441 (2019).

[47] M. Jaros, “Simple analytic model for heterojunction band offsets,” Phys. Rev. B, Condens. Matter.37, 7112 (1988).

[48] J. Menéndez, and J. Kouvetakis, "Type-I Ge ⁄ Ge1−x−ySixSny strained-layer heterostructures with a direct Ge bandgap," Applied Physics Letters 85, 1175-1177 (2004).

[49] V. R. D’Costa, C. S. Cook, A. G. Birdwell, C. L. Littler, M. Canonico, S. Zollner, J. Kouvetakis, and J. Menéndez, "Optical critical points of thin-film Ge1−ySny alloys: A comparative Ge1−ySny/Ge1−xSix study," Physical Review B 73, 125207 (2006).

[50] P. Moontragoon, R. A. Soref, and Z. Ikonic, "The direct and indirect bandgaps of unstrained SixGe1−x−ySny and their photonic device applications," Journal of Applied Physics 112, 073106 (2012).

[51] W.-J. Yin, X.-G. Gong, and S.-H. Wei, "Origin of the unusually large band-gap bowing and the breakdown of the band-edge distribution rule in the Ge1−ySny alloys," Physical Review B 78, 161203 (2008).

[52] L. Jiang, J. D. Gallagher, C. L. Senaratne, T. Aoki, J. Mathews, J. Kouvetakis, and J. Menéndez, "Compositional dependence of the direct and indirect band gaps in Ge1−ySnyalloys from room temperature photoluminescence: implications for the indirect to direct gap crossover in intrinsic andn-type materials," Semiconductor Science and Technology 29, 115028 (2014).

[53] S. Al-Kabi, S. A. Ghetmiri, J. Margetis, T. Pham, Y. Zhou, W. Dou, B. Collier, R. Quinde, W. Du, A. Mosleh, J. Liu, G. Sun, R. A. Soref, J. Tolle, B. Li, M. Mortazavi, H.

A. Naseem, and S.-Q. Yu, "An optically pumped 2.5 μm GeSn laser on Si operating at 110 K," Applied Physics Letters 109, 171105 (2016).

[54] S. A. Ghetmiri, Y. Zhou, J. Margetis, S. Al-Kabi, W. Dou, A. Mosleh, W. Du, A. Kuchuk, J. Liu, G. Sun, R. A. Soref, J. Tolle, H. A. Naseem, B. Li, M. Mortazavi, and S.-Q. Yu, "Study of a SiGeSn/GeSn/SiGeSn structure toward direct bandgap type-I quantum well for all group-IV optoelectronics," Opt. Lett. 42, 387-390 (2017).

[55] D. Stange, N. von den Driesch, D. Rainko, C. Schulte-Braucks, S. Wirths, G. Mussler, A. T. Tiedemann, T. Stoica, J. M. Hartmann, Z. Ikonic, S. Mantl, D. Grützmacher, and D. Buca, "Study of GeSn based heterostructures: towards optimized group IV MQW LEDs," Opt. Express 24, 1358-1367 (2016).

[56] J. Zheng, S. Wang, H. Cong, C. S. Fenrich, Z. Liu, C. Xue, C. Li, Y. Zuo, B. Cheng, J. S. Harris, and Q. Wang, "Characterization of a Ge1−x−ySiySnx/Ge1−xSnx multiple quantum well structure grown by sputtering epitaxy," Opt. Lett. 42, 1608-1611 (2017).

[57] W. Du, S. A. Ghetmiri, J. Margetis, S. Al-Kabi, Y. Zhou, J. Liu, G. Sun, R. A. Soref, J. Tolle, B. Li, M. Mortazavi, and S.-Q. Yu, "Investigation of optical transitions in a SiGeSn/GeSn/SiGeSn single quantum well structure," Journal of Applied Physics 122, 123102 (2017).

[58] H. S. Maczko, R. Kudrawiec, and M. Gladysiewicz, “Material gain engineering in GeSn/Ge quantum wells integrated with an Si platform,” Sci. Rep. 6, 34082 (2016).

[59] N. von den Driesch, D. Stange, D. Rainko, I. Povstugar, I. Zaumseil, G. Capellini, T. Schröder, T. Denneulin, Z. Ikonic, J.-M. Hartmann, H. Sigg, S. Mantl, D. Grützmacher and D. Buca, Advanced GeSn/SiGeSn Group IV Heterostructure Lasers, Adv. Sci. 5, 1700955 (2018).

[60] N. von den Driesch, D. Stange, D. Rainko, Z. Ikonic, J.-M. Hartmann, S. Mantl, H. Sigg, J. Witzens, D. Grutzmacher, and D. Buca, in IEEE Summer Topical Meeting, Waikoloa, Hawaii, USA, 9–11 July 2018.

[61] J. Margetis, S. A. Ghetmiri, W. Du, B. R. Conley, A. Mosleh, R. A. Soref, G. Sun, L. Domulevicz, H. A. Naseem, S.-Q. Yu, and J. Tolle “Growth and Characterization of Epitaxial Ge1-xSnx Alloys and Heterostructures Using a Commercial CVD System,” ECS Trans. 64, 711 (2014).

[62] J. Margetis, Y. Zhou, W. Dou, P. C. Grant, B. Alharthi, W. Du, A. Wadsworth, Q. Guo, H. Tran, S. Ojo, G. Abernathy, A. Mosleh, S. A Ghetmiri, G.B Thompson, J. Liu, G. Sun, R. Soref, J. Tolle, B. Li, M. Mortazavi, S.-Q. Yu, “All group-IV SiGeSn/GeSn/SiGeSn QW laser on Si operating up to 90 K,” Appl. Phys. Lett. 113, 221104 (2018).

[63] H. Tran, W. Du, S. A. Ghetmiri, A. Mosleh, G. Sun, R. A. Soref, J. Margetis, J. Tolle, B. Li, H. A. Naseem, and S.-Q. Yu, "Systematic study of Ge1−xSnx absorption coefficient

and refractive index for the device applications of Si-based optoelectronics," Journal of Applied Physics 119, 103106 (2016).

[64] Y. Arakawa and A. Yariv, “Quantum Well Lasers-Gain, Spectra, Dynamics,” IEEE J. Quantum, Electron., 22, 9, 1887 (1986).

[65] T. N. Pham, W. Du, B. R. Conley, J. Margetis, G. Sun, R. A. Soref, J. Tolle, B. Li, and S.-Q. Yu, “Si-based Ge0.9Sn0.1 photodetector with peak responsivity of 2.85 A/W and longwave cutoff at 2.4 μm,” Electron. Lett. 51, 854–856 (2015).

[66] W. Du, Y. Zhou, S. A. Ghetmiri, A. Mosleh, B. R. Conley, A. Nazzal, R. A. Soref, G. Sun, J. Tolle, J. Margetis, H. A. Naseem, and S.-Q. Yu, “Room-temperature electroluminescence from Ge/Ge1-xSnx/Ge diodes on Si substrates,” Appl. Phys. Lett. 104, 241110 (2014).

[67] J. D. Gallagher, C. L. Senaratne, C. Xu, P. Sims, T. Aoki, D. J. Smith, J. Menendez, and J. Kouvetakis, “Non-radiative recombination in Ge1−ySny light emitting diodes: The role of strain relaxation in tuned heterostructure designs,” J. Appl. Phys. 117, 245704 (2015).

[68] B. R. Conley, J. Margetis, W. Du, H. Tran, A. Mosleh, S. A. Ghetmiri, J. Tolle, G. Sun, R. A. Soref, B. Li, H. A. Naseem, and S.-Q. Yu, “Si based GeSn photoconductors with a 1.63 A/W peak responsivity and a 2.4 μm long-wavelength cutoff,” Appl. Phys. Lett. 105, 221117 (2014).

[69] M. Oehme, K. Kostecki, T. Arguirov, G. Mussler, K. Ye, M. Gollhofer, M. Schmid, M. Kaschel, R. A. Korner, M. Kittler, D. Buca, E. Kasper, and J. Schulze, “GeSn heterojunction LEDs on Si substrates,” IEEE Photonics Technol. Lett. 26, 187 (2014).

[70] E. Kasper and M. Oehme, Jpn. “Germanium tin light emitters on silicon,” J. Appl. Phys., Part 1 54, 04DG11 (2015).

[71] S.-Q. Yu, S. A. Ghetmiri, W. Du, J. Margetis, Y. Zhou, A. Mosleh, S. Al-Kabi, A. Nazzal, G. Sun, R. A. Soref, J. Tolle, B. Li, and H. A. Naseem, “Si based GeSn light emitter: mid-infrared devices in Si photonics,” Proc. SPIE 9367, 93670R (2015).

[72] Y. Zhou, W. Dou, W. Du, T. Pham, S. Ghetmiri, S. Al-Kabi, A. Mosleh, M. Alher, J. Margetis, J. Tolle, G. Sun, R. Soref, B. Li, M. Mortazavi, H. Naseem, and S. Yu, “Systematic study of GeSn heterostructure-based light-emitting diodes towards mid-infrared applications,” J. Appl. Phys. 120, 023102 (2016).

[73] J. E. Ayers, “The measurement of threading dislocation densities in semiconductor crystals by X-ray diffraction,” J. Cryst. Growth. 135, 71–77 (1994).

[74] W. Du, S. A. Ghetmiri, B. R. Conley, A. Mosleh, A. Nazzal, R. A. Soref, G. Sun, J. Tolle, J. Margetis, H. A. Naseem, and S.-Q. Yu, “Competition of optical transitions

between direct and indirect bandgaps in Ge1−xSnx," Appl. Phys. Lett. 105, 051104 (2014).

[75] Y. Dong, W. Wang, D. Lei, X. Gong, Q. Zhou, S. Y. Lee, W. K. Loke, S.-F. Yoon, E. S. Tok, G. Liang, and Y.-C. Yeo, "Suppression of dark current in germanium-tin on silicon p-i-n photodiode by a silicon surface passivation technique," Opt. Express 23, 18611–18619 (2015).

[76] C. Chang, H. Li, S.-H. Huang, L.-C. Lin, and H.-H. Cheng, "Temperature-dependent electroluminescence from GeSn heterojunction light-emitting diode on Si substrate," Jpn, J. Appl. Phys., Part 1 55, 04EH03 (2016).

[77] Y. Zhou, Y. Miao, S. Ojo, H. Tran, G. Abernathy, J. M. Grant, S. Amoah, G. Salamo, w. Du, J. Liu, J. Margetis, J. Tolle, Y.-H. Zhang, G. Sun, R. A. Soref, B. Li, and S.-Q. Yu, "Electrically injected GeSn lasers on Si operating up to 100 K," Optica 7, 924-928 (2020).

[78] G. Sun, H. H. Cheng, J. Menéndez, J. B. Khurgin, and R. A. Soref, "Strain-free Ge/GeSiSn quantum cascade lasers based on L-valley intersubband transitions," Appl. Phys. Lett. 90, 251105 (2007).

[79] H. Tran, T. Pham, J. Margetis, Y. Zhou, W. Dou, P. Grant, J. Grant, S. Al-Kabi, G. Sun, R. Soref, J. Tolle, Y. Zhang, W. Du, B. Li, M. Mortazavi, and S. Yu, "Si-Based GeSn photodetectors toward Mid-infrared imaging applications," ACS Photon. 6, 2807–2815 (2019).

[80] J. Pankove, "Temperature dependence of emission efficiency and lasing threshold in laser diodes," IEEE J. Quantum Electron. 4, 119–122 (1968).

[81] I. Hayashi and M. B. Panish, "GaAs–GaxAl1−xAs heterostructure injection lasers which exhibit low thresholds at room temperature," J. Appl. Phys. 41, 150 (1970).

[82] I. Hayashi, M. B. Panish, and F. K. Reinhart, "GaAs–AlxGa1−xAs double heterostructure injection lasers," J. Appl. Phys. 42, 1929 (1971).

[83] C. J. Nuese, M. Ettenberg, and G. Olsen, "Room-temperature heterojunction laser diodes from vapor-grown In1−xGaxP/GaAs structures," Appl. Phys. Lett. 25, 612 (1974).

[84] S. A. Ghetmiri, W. Du, B. R. Conley, A. Mosleh, A. Nazzal, G. Sun, R. A. Soref, J. Margetis, T. Joe, H. A. Naseem, and S. Q. Yu, "Shortwave-infrared photoluminescence from Ge1-xSnx thin films on silicon," J. Vac. Sci. Technol. B 32(6), 060601 (2014).

[85] E. Garmire and H. Stoll, "Propagation losses in metal-film-substrate optical waveguides, in IEEE Journal of Quantum Electronics," 8, 763-766 (1972).

[86] G.-E. Chang, S.-W. Chang, and S. L. Chuang, "Theory for n-type doped, tensile-strained Ge-SixGeySn1-x-y quantum-well lasers at telecom wavelength," Opt. Express 17, 11246-11258 (2009).

[87] C. Chaminant, J. Charil, J.-C. Bouley, and E.V.K. Rao, “Growth and properties of GaAsSb/GaAIAsSb double heterostructure lasers,” IEEE Trans. Electron. Devices, 3, 196 – 200 (1979).

[88] S. L. Chuang, Physics of Photonic Devices, chapter 10, pp. 416-417, Wiley Publishing, 2nd Edition.

[89] S. V. Kondratenko, Y. V. Hyrka, Y. I. Mazur, A. V. Kuchuk, W. Dou, H. Tran, J. Margetis, J. Tolle, S. Q. Yu, and G. J. Salamo, "Photovoltage spectroscopy of direct and indirect bandgaps of strained Ge1-xSnx thin films on a Ge/Si(001) substrate," Acta Materialia 171, 40-47 (2019).

Appendix

Appendix A: Far-field pattern and laser optical power output measurement setup

A1. Far-field pattern measurement setup

The spectrometer measurement setup was modified with a movable circular pinhole with 2-mm diameter, schematized in Fig. A1. The slit is placed at 4 cm away from the diode facet and is able to move along the x and y axis. The intensity was recorded by using the x and y coordinate with the slit. Then the coordinate is converted into the angle. The optic path remains the same as spectra measurements using the spectrometer. The liquid-nitrogen-cooled InSb photodetector was used.

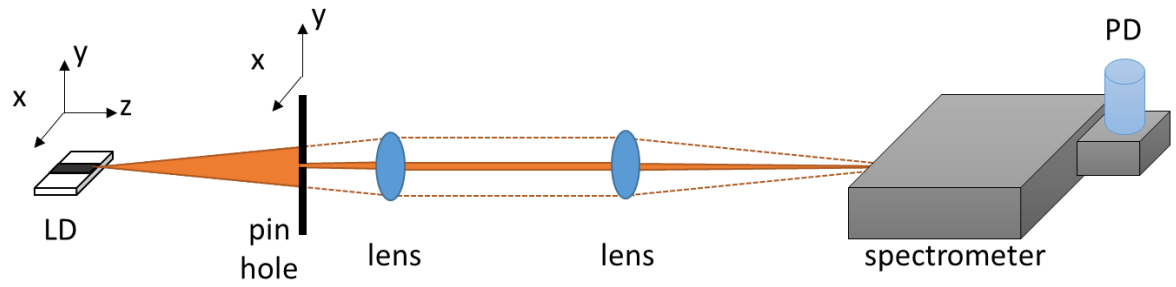

Figure A1 Schematic of the far-field pattern measured using the spectrometer setup.

A2. Laser power measurement

The laser output was measured using a power meter with a calibrated optical path to correct the collection efficiency. A 2-micro cw laser was brought into the optical path by an optical fiber aligning to the location of the laser diode in the cryostat. The emission transmits through the window and two lenses, focusing on the power meter. The collection efficiency was measured $\eta = I/I_0$, where I is the power value measured after lens, I_0 is the power value emitted

from the fiber. The device average power is therefore calibrated using the same optical path, as shown in Fig. A2(b). The actual emitted power was measured with the consideration of the transmission of the optics. The optics are made of CaF_2, which transmittance values at 2 and 2.3 μm are considered as the same.

The emission is guided into the spectrometer using a zero-order grating to deflect all light to the InSb photodetector. The response signal obtained from the photodetector is calibrated using the setup in Fig. A2(c). Under the schematic of laser characterization in Fig. A2 (d), then the detector response signal (pulsed) to the laser diode emission is calculated into peak power (average power divided by the duty cycle). Due to the response frequency limit of the photodetector, the pulsed signal is distorted due to the bandwidth limitation. A linear low-pass filter transfer function model is then added to exclude the effect from the detector bandwidth. Under such practice, peak power can be measured using the spectrometer setup, the power emission level is agreed with the value evaluated using the setup in Fig. A2 (a) and (b). The total power output (single facet) is added into the y scale of the L-I curve shown in Fig. 61 (a) and (b).

The effect from the numerical aperture limit is analyzed here. The fiber emission has no numerical aperture limit and can be collected entirely by the lens. However, the emission from the laser diode device may have some emission projected outside the lens. Based on the far-field pattern measurement in Fig. 64(f), the major emission modes can be well collected, while the broad-angle emission (mostly spontaneous emission) is cut off by the lens collectable angle (at ~10 degrees). Therefore, the power obtained here is still lower than the total emission, but the order of magnitude won't be affected as the major peak is collected.

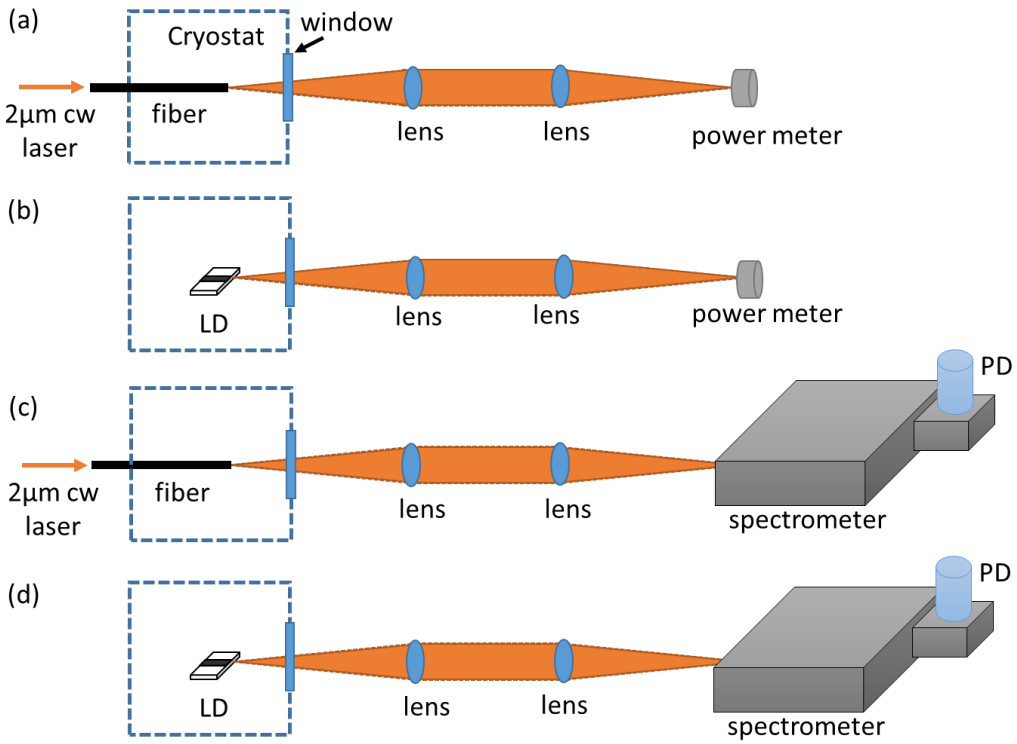

Figure A2. Calibration schematic of power output calibration: (a) The collection optical path loss was calibrated using 2μm cw laser; (b) the laser output was evaluated through the collection optical path; (c) photodetector signal response power calibration; and (d) laser diode power measurement.

Appendix B: Description of Research for Popular Publication

Almost every electronic device is now getting “smart” nowadays. One would immediately come out with an example: the smart phone. People intensively interact with smart devices to read the news, talk to friends, make payments, play games, listen to music, send emails, order foods, and so on. These functions mostly depend on two things: the internet and sensing. The cheap solutions for high-speed internet are always welcome. Optical sensors probe the shape, distance, color, or even the chemical composition of the objects. From the face recognition to LiDAR for automobiles, optical sensors serve as the eyes and noses for the machine to feel the world from all kinds of aspects. The instruments with such capabilities can free up people’s labor time, just like the cleaning robot.

Si photonics is such a platform that promises all the above-mentioned functions by building the optical components together on a single Si chip. It features compact, low-cost, high-performance, and reliable. However, building the light emission components onto this platform remains challenging due to the lack of compatible materials. Although the III-V semiconductor makes discrete light emission components, there is still a high cost on improving the yield when it comes to building on to Si a hard time directly grown on Si at a low cost. It would be highly desirable to have capable materials for the proper light emission capability.

SiGeSn alloy is a semiconductor that was found to be promising to serve as the proper material for light emission. Mr. Yiyin Zhou, a Ph.D. student in the Microelectronic-Photonics Program at the University of Arkansas, has been working on the research that makes SiGeSn into the light emitters on Si. He is in the research group led by Dr. Fisher Yu, Professor of the Department of Electrical Engineering. The research promotes the SiGeSn semiconductor into

light-emitting devices that could potentially beat the current markets, which compromise the III-V materials at a higher cost.

The study showed that the laser, a type of high-efficiency light-emitting device, operated at a higher temperature when incorporating Sn into Ge, as the GeSn alloy. The maximum operating temperature of the optically pumped laser (a laser fueled by light) reached 270 K (or 26 Degree Fahrenheit) from 180 K in the previous report.

In addition, the researcher has set feet on improving the device efficiency by introducing the multiple quantum well structure, which consists of nanometer-scale layers that promise a better emission efficiency. Optically pumped lasers showed light emission while reduced the fueling power to sustain light emission.

The light-emitting diodes are the light emitters fueled by electricity instead of light. The research showed a few generations of developments, leading to a decent improvement in the performance.

In recent discoveries, Mr. Zhou demonstrated the electrically injected (fueled by electric) lasers and their properties. The electrically injected lasers have much higher efficiency than the LEDs and are commonly used for the industry. This demonstration symbols the SiGeSn research has reached another milestone towards the commercialization for the market.

Appendix C: Executive Summary of Newly Created Intellectual Property

The following list of new intellectual property items were created during this research project and should be considered from both a patent and commercialization perspective.

1. A DHS p-i-n diode structure for GeSn LED and laser device. The DHS laser diode structure consists of a n-type Ge and GeSn buffer, an intrinsic GeSn active layer, a p-type SiGeSn cap layer. The SiGeSn cap layer is expected to be tensile strained, where a type-II band alignment is formed between the active layer and the cap layer. Therefore, a p-type doped cap as a hole injector would be preferred than a n-type doped cap, as the type-II alignment would not have proper hole confinement. Instead, the cap can be a hole injector for a p-i-n diode, where holes can be confinement by the GeSn buffer layer.
2. A diode structure with SiGeSn/GeSn SCH tensile-strained MQW for laser. The structure includes a tensile strained SiGeSn/GeSn/SiGeSn MQW structure, a SCH, and a stepped-composition SiGeSn buffer with large lattice constant. The tensile strained GeSn not only have larger directness, but also potentially have a reduced threshold.

Appendix D: Potential Patent and Commercialization Aspects of Listed Intellectual Property Items

D.1 Patentability of Intellectual Property (Could Each Item be Patented)

The items listed were considered first from the perspective of whether or not the item could be patented.

1. The DHS structure demonstrated in this research can be patented since the experimental results support theoretical design. The structure identified the limitation of the carrier confinement within prior DHS structure and was not mentioned in any prior study. The structure not only made LED functional with an improved emission intensity, but also achieved the first demonstration of electrically injected GeSn diode laser.
2. The proposed structure of item (2) can be patented as such structure has never been experimentally practiced. It might be argued that concepts of the DHS MQW structure and the strained MQW were commonly applied for III-V laser diodes. However, the tensile strain effect on the directness of GeSn layer is a unique feature for the GeSn material. The method of applying tensile strain in well by introducing large lattice constant SiGeSn buffer would have considerable potential impact for the GeSn based laser.

D.2 Commercialization Prospects (Should Each Item Be Patented)

The two items listed were then considered from the perspective of whether or not the item should be patented.

1. The structure of DHS diode structure should be patented. There are clear evidence that this structure offered the improved performance than prior art design. And the diode design is simple to be applied to commercial product to compete the current market.
2. The structure of SCH strained MQW diode laser should be patented. It has several advantages compared to current GeSn laser design and has potential to reach to the performance which makes the product highly competitive.

D.3 Possible Prior Disclosure of IP

The following items were discussed in a public forum or have published information that could impact the patentability of the listed IP.

1. This structure in item (1) was originally posted online at Arxiv on April 4, 2020.
2. The structure in item (2) has not yet been disclosed or discussed publicly.

Appendix E: Broader Impact of Research

E.1 Applicability of Research Methods to Other Problems

The compound semiconductor laser theory is well documented. There will be limited impact of in other problems. The method of pumping laser photon energy impacted to reduce the quantum defect related heating could be applied to other optically pumped scenarios. The high photon energy induces the electron to high energy levels and thermally relaxed to a lower energy level. relaxation difference of photon energy. The heating of sample would be reduced if the pumping laser photon energy is reduced but remain within the range of absorption.

E.2 Impact of Research Results on U.S. and Global Society

The results from this research have a significant impact on U.S. and Global Society. The group-IV based laser diodes on Si is a disruptive technology that could potentially boost the Si photonics technology to a new level by greatly reducing the cost of laser integration. There are global markets on data communications and bio/chemical sensing using Si Photonics, where the applications could range from the consumer electronics to medical/industrial sensor for specific purposes.

E.3 Impact of Research Results on the Environment

Although the semiconductor device processing involves many steps of adverse impact from the chemical used and produced, the research in this work would have limited since conventional process remains. On the bright side, the potential environment damage would

overall reduce in large volume of production comparing to the low-volume, discrete device production. The Si Photonics aims at compact integration of photonic devices, which makes the system to be energy efficient, contributing to the environment positively.

Appendix F: Microsoft Project for PhD MicroEP Degree Plan

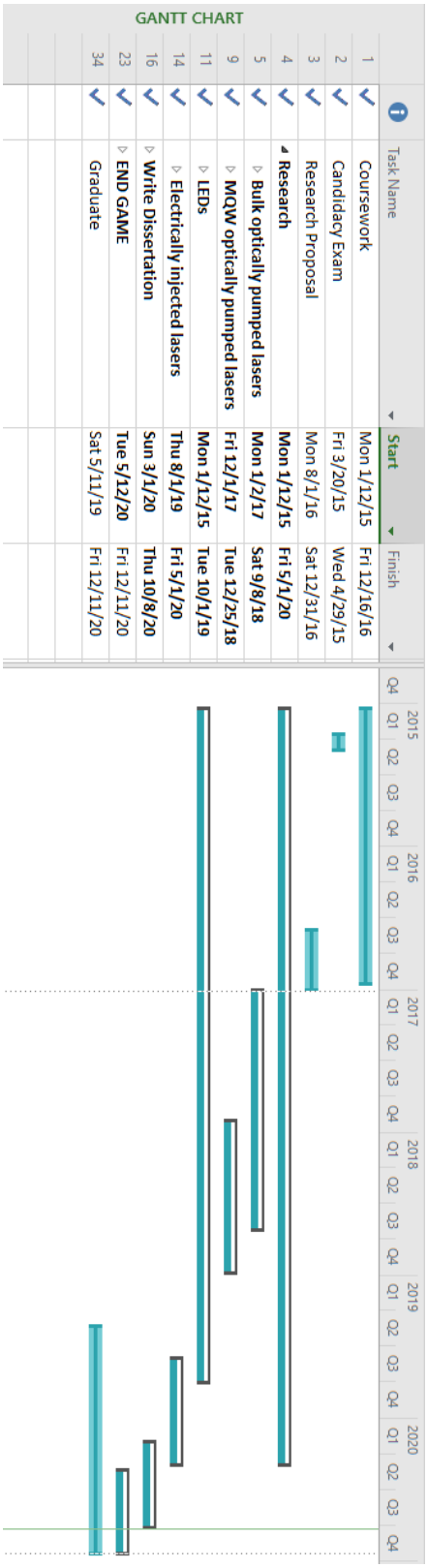

Appendix G: Identification of All Software Used in Research and Dissertation Generation

Computer #1:
- Model Number: Lenovo Y400
- Serial Number: YB00433081
- Location: Personal laptop
- Owner: Yiyin Zhou

Software #1:
- Name: Microsoft Office 365 ProPlus
- Provided by: University of Arkansas

Software #2:
- Name: MATLAB R2019b
- Provided by: University of Arkansas

Software #3:
- Name: Origin 2020b
- Purchased by: Yiyin Zhou

Software #4:
- Name: Microsoft Project 2016
- Provided by: University of Arkansas

Computer #2:
- Computer Name: ELEG-R3615w08
- Location: ENRC #3615
- Owner: Dr. Shui-Qing Yu

Software #1:
- Name: RSoft Photonic CAD Suite
- Purchased by: Dr. Shui-Qing Yu

Software #2:
- Name: Silvaco
- Purchased by: Department of Electrical Engineering, University of Arkansas

Computer #3:
- Computer Name: ELEG-R2933w01
- Location: ENRC #2933
- Owner: Dr. Shui-Qing Yu

Software #1:
- Name: LabVIEW
- Purchased by: Department of Electrical Engineering, University of Arkansas

Appendix H: All Publications Published, Submitted and Planned

H.1 Articles in Refereed Journals

2021

19 Yiyin Zhou, Solomon Ojo, Chen-Wei Wu, Yuanhao Miao, Huong Tran, Joshua M. Grant, Grey Abernathy, Sylvester Amoah, Jake Bass, Gregory Salamo, Wei Du, Guo-En Chang, Jifeng Liu, Joe Margetis, John Tolle, Yong-Hang Zhang, Greg Sun, Richard A. Soref, Baohua Li, Shui-Qing Yu, Electrically injected GeSn lasers with peak wavelength up to 2.7 μm, submitted to Photonics Research.

2021

18 Yiyin Zhou, Yuanhao Miao, Solomon Ojo, Grey Abernathy, Sylvester Amoah, Wei Du, Jifeng Liu, Yonghang Zhang, Greg Sun, Richard A. Soref, Baohua Li, Shui-Qing Yu, Electrically injected GeSn lasers on Si operating up to 100 K, Optica, 9, pp.924-928 (2020).

2019

17 Alejandra Vanessa Cuervo Covian, Yiyin Zhou, Xiaoxin Wang, Shui-Qing Yu, Jifeng Liu, Sn Nanodots-Induced Composition Enhancement (NICE) to Achieve 26 at.% Sn in GeSn for Mid-Infrared Integrated Photonics, ECS Transactions, 93 (1), 49-50 (2019).

16 Wei Du, Quang M. Thai, Jeremie Chrétien, Mathieu Bertrand, Lara Casiez, Yiyin Zhou, Joe Margetis, Nicolas Pauc, Alexei Chelnokov, Vincent Reboud, Vincent Calvo, John Tolle, Baohua Li and Shui-Qing Yu, Study of Si-based GeSn optically pumped lasers with micro-disk and ridge waveguide structures, Front. Phys. 7:147., doi: 10.3389/fphy.2019.00147.

15 Huong Tran, Thach Pham, Joe Margetis, Yiyin Zhou, Wei Dou, Perry C. Grant, Joshua M. Grant, Sattar Alkabi, Wei Du, Greg Sun, Richard A. Soref, John Tolle, Baohua Li, Mansour Mortazavi, and Shui-Qing Yu, Si-based GeSn photodetectors towards mid-infrared imaging applications, ACS Photonics 2019, DOI: 10.1021/acsphotonics.9b00845.

14 T. D. Eales, I. P. Marko, S. Schulz, E. O'Halloran, S. A. Ghetmiri, W. Du, Y. Zhou, S.Q. Yu, J. Margetis, J. Tolle, E. P. O'Reilly, and S. J. Sweeney, Ge1−xSnx alloys: Consequences of band mixing effects for the evolution of the band gap Γ-character with Sn concentration, Scientific Reports 9, 1, 1-10 (2019).

13 Yiyin Zhou, Wei Dou, Wei Du, Solomon Ojo, Huong Tran, Seyed A. Ghetmiri, Jifeng Liu, Greg Sun, Richard Soref, Joe Margetis, John Tolle, Baohua Li, Zhong Chen, Mansour Mortazavi, Shui-Qing Yu, Si-based GeSn lasers with ridge and planar waveguide structures and operating temperatures up to 270 K, ACS Photonics 6, 1434 (2019).

2018

12 Joe Margetis, Yiyin Zhou, Wei Dou, Perry C. Grant, Wei Du, Bader Alharthi, Huong Tran, Solomon Ojo, Grey Abernathy, Seyed A. Ghetmiri, Jifeng Liu, Greg Sun, Richard Soref, John Tolle, Baohua Li, Mansour Mortazavi, Shui-Qing Yu, All group-IV SiGeSn/GeSn/SiGeSn QW laser on Si operating up to 90 K, Applied Physics Letters 113 (22), 221104 (2018).

11 Perry Grant, Joe Margetis, Wei Du, Yiyin Zhou, Wei Dou, Grey Abernathy, Andrian Kuchuk, Baohua Li, John Tolle, Jifeng Liu, Greg Sun, Richard Soref, Mansour Mortazavi, Shui-Qing Yu, Study of Direct Bandgap Type-I GeSn/GeSn Double Quantum Well with Improved Carrier Confinement, Nanotechnology 29 (46), 465201 (2018).

10 Wei Dou, Yiyin Zhou, Joe Margetis, Seyed Amir Ghetmiri, Sattar Al-Kabi, Wei Du, Jifeng Liu, Greg Sun, Richard A. Soref, John Tolle, Baohua Li, Mansour Mortazavi, and Shui-Qing Yu, Optically pumped lasing at 3 μm from compositionally graded GeSn with Sn up to 22.3%, Optics letters 43 (19), 4558-4561 (2018).

9 Perry C. Grant, Joe Margetis, Yiyin Zhou, Wei Dou, Grey Abernathy, Wei Du, Baohua Li, John Tolle, Jifeng Liu, Greg Sun, Richard A. Soref, Mansour Mortazavi, Shui-Qing Yu, Direct Bandgap Type-I GeSn/GeSn Quantum Well on Si substrate, AIP Advances 8, 025104 (2018).

8 Wei Dou, Mourad Benamara, Aboozar Mosleh, Joe Margetis, Perry Grant, Yiyin Zhou, Sattar Al-Kabi, Wei Du, John Tolle, Baohua Li, Mansour Mortazavi, Shui-Qing Yu, Investigation of GeSn Strain Relaxation and Spontaneous Composition Gradient for Low-Defect and High-Sn Alloy Growth, Scientific Reports (Nature Publisher Group) vol. 8, pp. 1-11 (2018).

7 Joe Margetis, Sattar Al-Kabi, Wei Du, Wei Dou, Yiyin Zhou, Thach Pham, Perry Grant, Seyed Ghetmiri, Aboozar Mosleh, Baohua Li, Jifeng Liu, Greg Sun, Richard Soref, John Tolle, Mansour Mortazavi, Shui-Qing Yu, Si-based GeSn lasers with wavelength coverage of 2 to 3 μm and operating temperatures up to 180 K, ACS Photonics, ACS Photonics, 5 (3), pp 827–833 (2018)

2017

6 Wei Du, Seyed Amir Ghetmiri, Joe Margetis, Sattar Al-Kabi, Yiyin Zhou, Jifeng Liu, Greg Sun, Richard A. Soref, John Tolle, Baohua Li, Mansour Mortazavi, and Shui-Qing Yu, Investigation of optical transitions in a SiGeSn/GeSn/SiGeSn single quantum well structure, Journal of Applied Physics 122, 123102 (2017).

5 Seyed A. Ghetmiri, Yiyin Zhou, Joe Margetis, Sattar Al-Kabi, Wei Dou, Aboozar Mosleh, Wei Du, Andrian Kuchuk, Jifeng Liu, Greg Sun, Richard A. Soref, John Tolle, Hameed A. Naseem, Baohua LI, Mansour Mortazavi, and Shui-Qing Yu, Study of SiGeSn/GeSn/SiGeSn structure towards direct bandgap type-I quantum well for all group-IV-optoelectronics, Optics Letters, Vol. 42, No. 3, pp 387- 390 (2017).

2016

4 Sattar Al-Kabi, Seyed Ghetmiri, Joe Margetis, Thach Pham, Yiyin Zhou, Bria Collier, Randy Quinde, Wei Du, Aboozar Mosleh, Jifeng Liu, Greg Sun, Richard Soref, John Tolle, Baohua Li, Mansour Mortazavi, Hameed Naseem, and Shui-Qing Yu, An optically pumped 2.5 μm GeSn laser on Si operating at 110 K, Applied Physics Letters 109, 171105 (2016).

3 Wei Dou, Seyed Ghetmiri, Sattar Al-Kabi, Aboozar Mosleh, Yiyin Zhou, Bader Alharthi, Wei Du, Joe Margetis, John Tolle, Andrian Kuchuk, Mourad Benamara, Baohua Li, Hameed Naseem, Mansour Mortazavi, and Shui-Qing Yu, Structural and Optical Characteristics of GeSn Quantum Wells for Silicon-Based Mid-Infrared Optoelectronic Applications, Journal of Electronic Materials, 45, 6265 (2016).

2 Yiyin Zhou, Wei Dou, Wei Du, Thach Pham, Seyed Amir Ghetmiri, Sattar Al-Kabi, Aboozar Mosleh, Joe Margetis, John Tolle, Greg Sun, Richard Soref, Baohua Li, Mansour Mortazavi, Hameed Naseem, and Shui-Qing Yu, Systematic study of Si-based GeSn light-emitting diodes towards mid-infrared applications, Journal of Applied Physics 120, 023102 (2016).

2014

1 Wei Du, Yiyin Zhou, Seyed A. Ghetmiri, Aboozar Mosleh, Benjamin R. Conley, Amjad Nazzal, Richard A. Soref, Greg Sun, John Tolle, Joe Margetis, Hameed A. Naseem, and Shui-Qing Yu, Room-temperature electroluminescence from Ge/Ge1-xSnx/Ge double heterostructure LEDs on Si substrates via CVD, Appl. Phys. Lett., vol. 104, pp. 241110 (2014)

H.2 Articles and Abstracts in Conference Proceedings

2020

29 Grey Abernathy, Yiyin Zhou, Solomon Ojo, Yuanhao Miao, Wei Du, Greg Sun, Richard Soref, Jifeng Liu, Yong-Hang Zhang, Mansour Mortazavi, Baohua Li, and Shui-Qing Yu, "Study of gain for SiGeSn/GeSn/SiGeSn multiple quantum well lasers," in Conference on Lasers and Electro-Optics, OSA Technical Digest (Optical Society of America, 2020), paper SM3M.5.

28 Yiyin Zhou, Yuanhao Miao, Solomon Ojo, Grey Abernathy, Wei Du, Greg Sun, Richard Soref, Jifeng Liu, Yong-Hang Zhang, Mansour Mortazavi, Baohua Li, and Shui-Qing Yu, "Direct bandgap electroluminescence from SiGeSn/GeSn double-heterostructure monolithically grown on Si," in Conference on Lasers and Electro-Optics, OSA Technical Digest (Optical Society of America, 2020), paper SM3M.4.

27 Yiyin Zhou, Huong Tran, Wei Du, Jifeng Liu, Greg Sun, Richard Soref, Joe Margetis, John Tolle, Yong-Hang Zhang, Baohua Li, Mansour Mortazavi, Shui-Qing Yu, "Mid-Infrared GeSn/SiGeSn Lasers and Photodetectors Monolithically Integrated on Silicon," in *Conference*

on Lasers and Electro-Optics, OSA Technical Digest (Optical Society of America, 2020), paper JM2E.1.

2019

26 Yiyin Zhou, Huong Tran, and Shui-Qing Yu, Wei Du, Joe Margetis, John Tolle, Seyed Ghetmiri, Aboozar Mosleh, Mansour Mortazavi, Greg Sun, Richard Soref, and Baohua Li, 2019 IEEE BiCMOS and Compound Semiconductor Integrated Circuits and Technology Symposium (BCICTS), Nashville, TN, USA.

25 Yiyin Zhou, Huong Tran, and Shui-Qing Yu, Wei Du, Joe Margetis, John Tolle, Seyed Ghetmiri, Aboozar Mosleh, Mansour Mortazavi, Greg Sun, Richard Soref, and Baohua Li, Development of GeSn/SiGeSn Technique towards Integrated Mid-Infrared Photonics Applications, IEEE Research and Applications of Photonics in Defense (RAPID 2019), Miramar Beach, FL, 8/19-8/21, TuD 1.2.

24 Alejandra V. Cuervo Covian, Yiyin Zhou, Xiaoxin Wang, Shui-Qing Yu, Jifeng Liu, Sn Nanodots-Induced Composition Enhancement (NICE) to Achieve 26 at. % Sn in GeSn for Mid-Infrared Integrated Photonics, 2nd Joint ISTDM / ICSI 2019 Conference, 6/2-6/6 (2019), University of Wisconsin-Madison

23 Yiyin Zhou, Huong Tran, and Shui-Qing Yu, Wei Du, Joe Margetis, John Tolle, Seyed Ghetmiri, Aboozar Mosleh, and Mansour Mortazavi, Greg Sun, Richard Soref, and Baohua Li, Development of GeSn Emitters and Detectors towards Integrated Mid-Infrared Photonics Applications, IEEE Summer Topical Meeting 2019, Fort Lauderdale, Florida.

22 Yiyin Zhou, Joe Margetis, Grey Abernathy, Wei Dou, Perry C Grant, Bader Alharthi, Wei Du, Alicia Wadsworth, Qianying Guo, Huong Tran, Solomon Ojo, Aboozar Mosleh, Seyed A Ghetmiri, Gregory B Thompson, Jifeng Liu, Greg Sun, Richard Soref, John Tolle, Baohua Li, Mansour Mortazavi, Shui-Qing Yu, Investigation of SiGeSn/GeSn/SiGeSn Quantum Well Structures and Optically Pumped Lasers on Si, CLEO 2019 (San Jose): Science and Innovations, STu3N. 3.

21 Huong Tran, Thach Pham, Joe Margetis, Yiyin Zhou, Wei Dou, Perry C Grant, Joshua M Grant, Sattar Alkabi, Wei Du, Greg Sun, Richard A Soref, John Tolle, Baohua Li, Mansour Mortazavi, Shui-Qing Yu, Study of High Performance GeSn Photodetectors with Cutoff Wavelength up to 3.7 μm for Low-Cost Infrared Imaging, CLEO 2019 (San Jose): Science and Innovations, STh4O. 6.

20 Yiyin Zhou, Wei Dou, Wei Du, Solomon Ojo, Huong Tran, Seyed Ghetmiri, Jifeng Liu, Greg Sun, Richard Soref, Joe Margetis, John Tolle, Baohua Li, Zhong Chen, Mansour Mortazavi, Shui-Qing Yu, Si-based Mid-Infrared GeSn-Edge-Emitting Laser with Operating Temperature up to 260 K, CLEO 2019 (San Jose): Applications and Technology, AW3P.3.

19 Yiyin Zhou, Wei Dou, Perry C. Grant, Joe Margetis, Wei Du, Seyed A. Ghetmiri, Aboozar Mosleh, John Tolle, Greg Sun, Richard A. Soref, Jifeng Liu, Baohua Li, Mansour Mortazavi,

and Shui-Qing Yu, Silicon-based GeSn Mid-Infrared Lasers, SPIE Photonic West, San Francisco (2019).

2018

18 Shui-Qing Yu, Wei Du, Wei Dou, Yiyin Zhou, Perry Grant, Thach Pham, Huong Tran, Joe Margetis, John Tolle, Seyed Ghetmiri, Aboozer Mosleh, Mansour Mortazavi, Jifeng Liu, Greg Sun, Richard Soref, and Baohua Li, Development of Si-based GeSn Laser, Compound Semiconductor Week 2018, Th2A6.5.

17 Wei Dou, Yiyin Zhou, Huong Tran, Thach Pham, Perry Grant, and Shui-Qing Yu, Seyed Ghetmiri, Aboozar Mosleh, Wei Du, Joe Margetis, John Tolle, Mansour Mortazavi, Greg Sun, Richard Soref, Huong Tran, Yiyin Zhou, Perry Grant, and Baohua Li, Development of SiGeSn Technique towards Integrated Mid-Infrared Photonics Applications, IEEE Summer Topical Meeting 2018 (Waikoloa), IMIP, MA3.2 (Plenary).

16 Perry C. Grant, Joe Margetis, Yiyin Zhou, Wei Dou, Grey Abernathy, Andrian Kuchuk, Wei Du, Seyed A. Ghetmiri, Baohua Li, John Tolle, Jifeng Liu, Greg Sun, Richard A. Soref, Mansour Mortazavi, Shui-Qing Yu, Direct Bandgap Type-I GeSn Quantum Well toward Si-based Optoelectronics, CLEO 2018 (San Jose): Science and Innovations, STh4I. 4.

15 Wei Dou, Yiyin Zhou, Joe Margetis, Seyed Amir Ghetmiri, Wei Du, Jifeng Liu, Greg Sun, Richard A. Soref, John Tolle, Baohua Li, Mansour Mortazavi, and Shui-Qing Yu, Optically Pumped GeSn-edge-emitting Laser with Emission at 3 μm for Si Photonics, CLEO 2018 (San Jose): Applications and Technology, AF1Q. 5.

2017

14 Joe Margetis, John Tolle, Sattar Al-Kabi, Yiyin Zhou, Huong Tran, Thach Pham, Wei Dou, Perry Grant, Shui-Qing Yu, Wei Du, Seyed Ghetmiri, Mansour Mortazavi, Greg Sun, Richard Soref, Baohua Li, GeSn-based Light Sources and Photoconductors towards Integrated Photonics for the Mid-Infrared, 2017 Summer Topicals Meeting Series (10 - 12 July 2017), San Juan, Puerto Rico

13 Timothy Eales, Igor P. Marko, Seyed A. Ghetmiri, Wei Du, Yiyin Zhou, Shui-Qing Yu, Joe Margetis, John Tolle, Stefan Schulz, Edmond O'Halloran, Eoin P. O'Reilly and Stephen J. Sweeney, New experimental evidence for nature of the band gap of GeSn Alloys, SPIE Photonics West, No. 10108-48, Jan 30-Feb 1, 2017, San Francisco, CA, USA.

12 Wei Du, Seyed Ghetmiri, Sattar Al-Kabi, Aboozar Mosleh, Thach Pham, Yiyin Zhou, Huong Tran, Greg Sun, Richard Soref, Joe Margetis, John Tolle, Baohua Li, Mansour Mortazavi, Hameed Naseem, Shui-Qing Yu, Silicon-based $Ge_{0.89}Sn_{0.11}$ photodetector and light emitter towards mid-infrared applications, SPIE Photonics West, No. 10108-38, Jan 30-Feb 1, 2017, San Francisco, CA, USA.

11 Sattar Al-Kabi, Seyed Amir Ghetmiri, Joe Margetis, Thach Pham, Yiyin Zhou, Wei Dou, Wei Du, Aboozar Mosleh, Jifeng Liu, Greg Sun, Richard A. Soref, John Tolle, Baohua Li, Mansour Mortazavi, Hameed A. Naseem, and Shui-Qing Yu, Optically pumped Si-based edge-emitting GeSn laser, CLEO 2017, SW4C. 1

10 Huong Tran, Thach Pham, Wei Du, Joe Margetis, Yiyin Zhou, Perry C. Grant, Greg Sun, Richard A. Soref, John Tolle, Baohua Li, Mansour Mortazavi, Hameed A. Naseem, and Shui-Qing Yu, Temperature Dependent Study of Lifetime and Minority Carrier Diffusion Constant for $Ge_{0.89}Sn_{0.11}$ Photoconductors, CLEO 2017, STu1N. 6

9 Wei Du, Seyed Ghetmiri, Sattar Al-Kabi, Joe Margetis, Yiyin Zhou, Wei Dou, Aboozar Mosleh, Jifeng Liu, Greg Sun, Richard Soref, John Tolle, Baohua Li, Mansour Mortazavi, , and Shui-Qing Yu, Study of SiGeSn/GeSn/SiGeSn Quantum Well towards All Group-IV-Optoelectronics, CLEO 2017, STh3I. 3

2016

8 Timothy Eales, Igor P. Marko, Seyed A. Ghetmiri, Wei Du, Yiyin Zhou, Shui-Qing Yu, Stefan Schulz, Eoin P. O'Reilly, and Stephen J. Sweeney, "GeSn Alloys for Mid-infrared Optoelectronics", the 13th International Conference on Mid-Infrared Optoelectronics: Materials and Devices, Beijing, China, September 18-22 (2016).

7 Huong Tran, Thach Pham, Yiyin Zhou, Seyed Ghetmiri, Sattar Al-Kabi, Aboozar Mosleh, Hameed Naseem, Shui-Qing Yu, John Tolle, Joe Margetis, Wei Du, Mansour Mortazavi, Richard Soref, Greg Sun, and Baohua Li, "Investigation of Si-based Ge0.93Sn0.07 Photoconductors towards Short-wave Infrared Detection", IEEE Summer Topicals Meetings, Newport Beach, CA, USA, July 11-13 (2016).

6 Yiyin Zhou, Wei Du, Wei Dou, Thach Pham, Aboozar Mosleh, Seyed Amir Ghetmiri, Sattar Al-Kabi, Joe Margetis, John Toll,4Greg Sun, Richard Soref, Baohua Li, Mansour Mortazavi, Hameed Naseem, and Shui-Qing Yu, "Systematic Study of Si based $Ge_{0.9}Sn_{0.1}$ Light-Emitting Diode towards Mid-Infrared Application", the Conference On Lasers and Electrooptics (CLEO), No. JW2A.127, San Jose, CA, USA, June 5-10 (2016).

2015

5 Seyed Amir Ghetmiri, Wei Du, Yiyin Zhou, Joe Margetis, Thach Pham, Aboozar Mosleh, Benjamin R. Conley, Greg Sun, Richard Soref, John Tolle, Hameed A. Naseem, Baohua Li, and Shui-Qing Yu, Temperature-dependent characterization of $Ge_{0.94}Sn_{0.06}$ Light-Emitting Diode grown on Si via CVD, the Conference On Lasers and Electrooptics (CLEO) 2015, ATu1J.6, May 10-15, 2015, San Jose, CA, USA.

4 Wei Du, Seyed A. Ghetmiri, Yiyin Zhou, Aboozar Mosleh, Joe Margetis, John Tolle, Greg Sun, Richard A. Soref, Baohua Li, Hameed Naseem, and Shui-Qing Yu, Si-Based GeSn Edge-

Emitting LEDs with Sn Compositions up to 8%, 2015 IEEE Summer Topicals, July 13-15, Nassau, Bahamas (2015).

3 S.-Q. Yu, S. A. Ghetmiri, W. Du, J. Margetis, Y. Zhou, A. Mosleh, S. Al-Kabi, A. Nazzal, G. Sun, R.A. Soref, J. Tolle, B. Li, and H.A. Naseem, Si based GeSn light emitter: mid-infrared device in Si photonics, SPIE Photonics West, No. 9367-26, February 7-12, 2015, San Francisco, CA, USA.

2014

2 Yiyin Zhou, Wei Du, Seyed Amir Ghetmiri, Aboozar Mosleh, Amjad Nazzal, Richard A Soref, Greg Sun, Joe Margetis, John Tolle, Hameed A. Naseem, and Shui-Qing Yu, Room-temperature electroluminescence from Ge/Ge0.92Sn0.08/Ge double heterostructure LED on Si, IEEE Photonics Conference, San Diego (2014).

1 Benjamin R. Conley, Yiyin Zhou, Aboozar Mosleh, Seyed Amir Ghetmiri, Wei Du, Richard A Soref, Greg Sun, Joe Margetis, John Tolle, Hameed A. Naseem, and Shui-Qing Yu, Infrared spectral response of a GeSn p-i-n photodiode on Si, in the 11th International Conference on Group IV Photonics, Paris (2014).

Appendix I: Publishing Agreements/Permissions

ACS Photonics

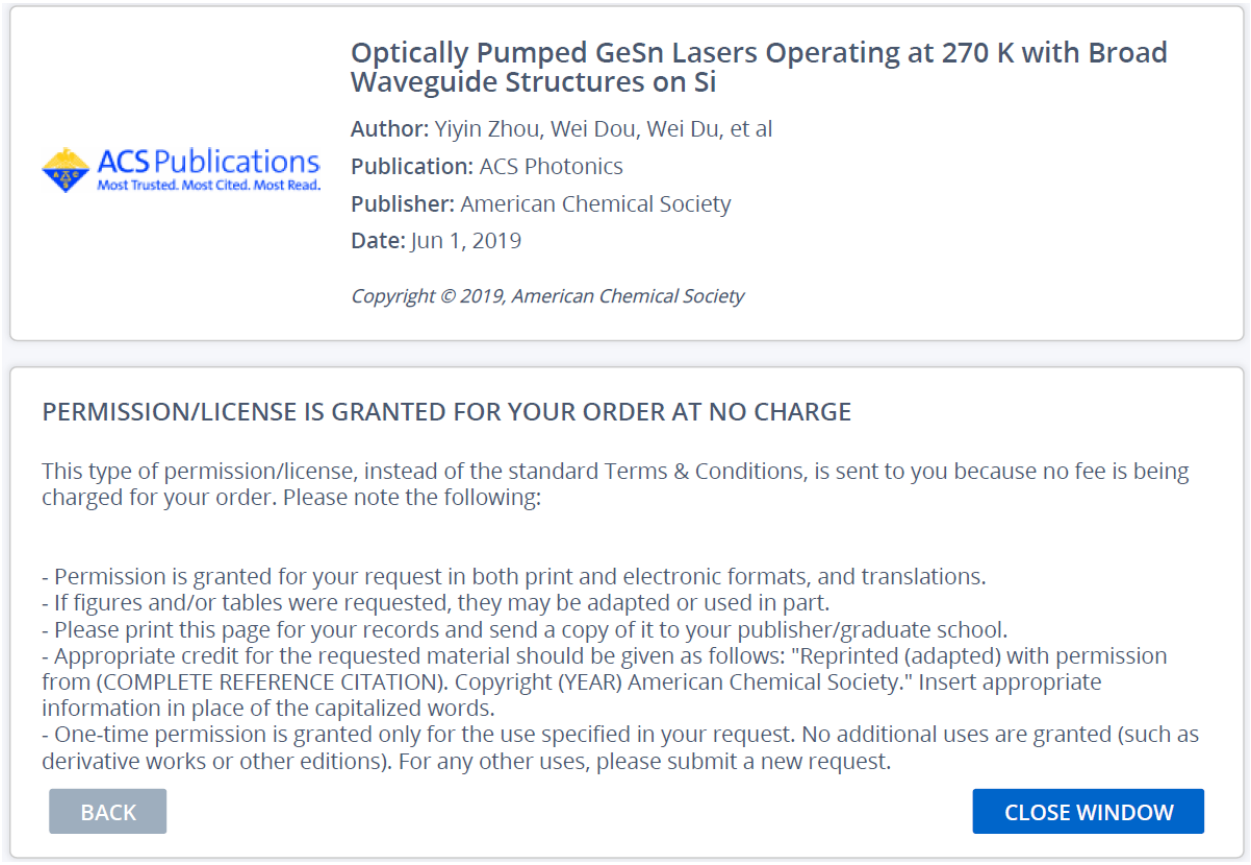

Optically Pumped GeSn Lasers Operating at 270 K with Broad Waveguide Structures on Si

Author: Yiyin Zhou, Wei Dou, Wei Du, et al

Publication: ACS Photonics

Publisher: American Chemical Society

Date: Jun 1, 2019

Copyright © 2019, American Chemical Society

PERMISSION/LICENSE IS GRANTED FOR YOUR ORDER AT NO CHARGE

This type of permission/license, instead of the standard Terms & Conditions, is sent to you because no fee is being charged for your order. Please note the following:

- Permission is granted for your request in both print and electronic formats, and translations.
- If figures and/or tables were requested, they may be adapted or used in part.
- Please print this page for your records and send a copy of it to your publisher/graduate school.
- Appropriate credit for the requested material should be given as follows: "Reprinted (adapted) with permission from (COMPLETE REFERENCE CITATION). Copyright (YEAR) American Chemical Society." Insert appropriate information in place of the capitalized words.
- One-time permission is granted only for the use specified in your request. No additional uses are granted (such as derivative works or other editions). For any other uses, please submit a new request.

BACK CLOSE WINDOW

Journal of Applied Physics & Applied Physics Letter

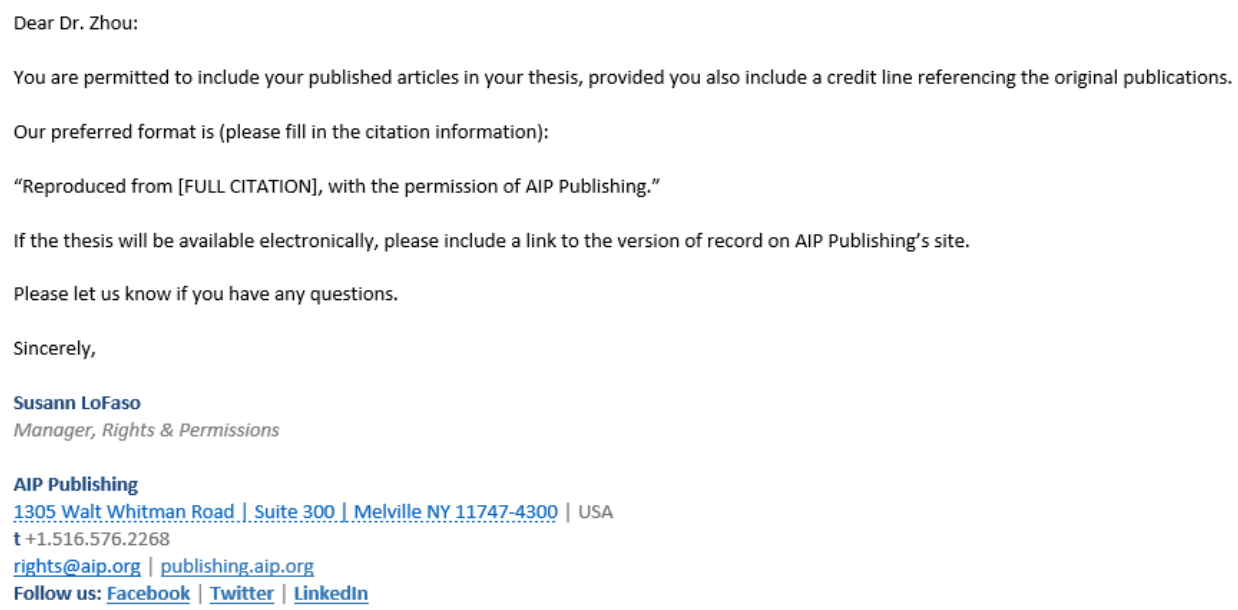

Dear Dr. Zhou:

You are permitted to include your published articles in your thesis, provided you also include a credit line referencing the original publications.

Our preferred format is (please fill in the citation information):

"Reproduced from [FULL CITATION], with the permission of AIP Publishing."

If the thesis will be available electronically, please include a link to the version of record on AIP Publishing's site.

Please let us know if you have any questions.

Sincerely,

Susann LoFaso
Manager, Rights & Permissions

AIP Publishing
1305 Walt Whitman Road | Suite 300 | Melville NY 11747-4300 | USA
t +1.516.576.2268
rights@aip.org | publishing.aip.org
Follow us: Facebook | Twitter | LinkedIn

Optica:

Dear YiYin Zhou,

Thank you for contacting The Optical Society (OSA).

For the use of material from Yiyin Zhou, Yuanhao Miao, Solomon Ojo, Huong Tran, Grey Abernathy, Joshua M. Grant, Sylvester Amoah, Gregory Salamo, Wei Du, Jifeng Liu, Joe Margetis, John Tolle, Yong-hang Zhang, Greg Sun, Richard A. Soref, Baohua Li, and Shui-Qing Yu, "Electrically injected GeSn lasers on Si operating up to 100 K," Optica 7, 924-928 (2020):

Because you are the author of the source paper from which you wish to reproduce material, OSA considers your requested use of its copyrighted materials to be permissible within the author rights granted in the Copyright Transfer Agreement submitted by the requester on acceptance for publication of his/her manuscript. It is requested that a complete citation of the original material be included in any publication. This permission assumes that the material was not reproduced from another source when published in the original publication.

For the use of this paper in your thesis, it is permissible to use the version of record.

While your publisher should be able to provide additional guidance, OSA prefers the below citation formats:

For citations in figure captions:

[Reprinted/Adapted] with permission from [ref #] © The Optical Society. (Please include the full citation in your reference list)

For images without captions:

Journal Vol. #, first page (year published) An example: Opt. Express 19, 2720 (2011)

Please let me know if you have any questions.

Kind Regards,
Hannah Greenwood

Hannah Greenwood
October 7, 2020
Authorized Agent, The Optical Society